Optimisation of The Value in-use of The Refractory Submerged Entry Nozzle: Implication of preheating failures

Swansea University
Prifysgol Abertawe

Ebrima Sallah

Materials and Manufacturing Academy

College of Engineering

Swansea University

Submitted to Swansea University in fulfilment of the requirements for the Degree of Doctor of Engineering

October 2023

Abstract

There is a need to understand the preheating process implication on the performance of a submerged entry nozzle (SEN) that allows the transfer of liquid steel from tundish to mould. The SEN suffers from failure attributed to improper preheating, leading to sudden thermal shock failures and oxidation of its carbonaceous matrix weakening its resistance to fracture. Process knowledge concerning temperature and time period that the SEN is exposed is often lacking/or insufficient in sponsor site (steel user of product). It is not currently being practised or possible to monitor the temperature of the SEN during its use. This is perhaps due to lack of cost-effective methods for sponsor, which therefore necessitates a new approach in obtaining quantitative and effect profiling methods that can address the gap in process knowledge implications on SEN performance. In future the same profiling methods are suggested is a way to generate datasets for modelling and predicting the missing process variables that impact on performance (i.e., the effect of time and temperature combined) since the material displays distinguishable profiles based on preheat treatment. The data can be further processed to address failure classification.

Three of the same supplier batch SENs were characterised in this study, comprising of one virgin SEN and two industrially as-received preheated SENs (i.e., one heated for three hours and the other for six hours). Carbon phases present within the SEN were used as a marker when profiling and assess oxidation resistance. The synergistic use of Model-free kinetics, Raman cluster analysis imaging technique, temperature modulated Raman spectroscopy, supplemented with X-ray Photoelectron Spectroscopy analysis, were effective in; 1) distinguishing of carbon phases 2) tracking of oxidation and pyrolytic degradation 3) non-isothermal oxidation kinetic profiling 4) oxidation resistance comparison between SENs 5) oxidation kinetic influences based on chemical, surface area changes and microstructure. Micro–X-ray Computed Tomography provided pore analysis discriminatory values to support the microstructural evaluation of oxidation, whilst at the same time highlighting its potential for macro-crack network analysis related to thermal shock. Laser flash analysis corroborated detection of temperatures linked to microstructural changes of the pore-closure mechanism that was also evaluated by temperature modulated Raman, with results tracking the G-peak shift associated with stress-strain effects. Lastly, the impulse excitation technique was used for evaluating thermal shock resistance of the SENs utilising the Q-factor (dampening) values.

When evaluating the preheated SENs, the 3-hour SEN presented a lesser risk factor to thermal shock than the 6-hour, with values of Q-factor: 10.36 and 92.94 respectively. However, the 6-hour showed more resistance to oxidation than the 3-hour when using the graphite cluster phase at conversion $\geq 0.5\%$ and their corresponding temperatures ≥ 650 °C. It appears that lower temperatures showed the virgin to be more resistance to oxidation in relation to the graphite cluster phase only. The virgin sample results of thermal shock were somewhat between the two SENs indicative of a healing process occurring after the diminishing of thermal shock resistance during heating. The Vyazovkin method of activation energy values from the non-isothermal oxidation kinetics profiles for both resin and graphite regions were in the ranged between 150 kJ/mol to 220 kJ/mol.

Authorship Statement

The following people and institutions contributed to a peer reviewed journal publication from work undertaken as part of this thesis:

Authorship Declaration:

Name	*Name and College*
Ebrima Sallah	Swansea University - College of Engineering
Wafaa Al-Shatty	Swansea University - College of Engineering
Cameron Pleydell-Pearce	Swansea University - College of Engineering
Chris Smith	UKAEA- Materials Research Facility
Andy J London	UKAEA- Materials Research Facility

Author Details and their Roles:

Title: "Distinguishing of carbons and oxidation behaviour (Part 1): Exploring model-free kinetics and RAMAN spectroscopy as a synergistic approach for evaluating carbon-bonded-refractories"

Located in Chapter: 3, 4, 6 and 8

Main Author: Ebrima Sallah

Contributed: Funding acquisition, complete concept and experimental design, data analysis for all data present, writing of the complete journal (editing and reviewing) and submission of journal.

Author: Wafaa Al-Shatty

Contributed: Facilitator for SDT access, responsible for running TGA experiment on behalf of main author due to COVID access limitation and upon seeking the approval from co-

author's supervisor. Collaboration was established on this basis. Provided SEM data for supplementary material under the collaboration established. Review of journal.

Author (Supervisor): Cameron Pleydell-Pearce

Contributed: Funding acquisition, review and edit of journal

Author: Chris Smith and Andy J London

Contributed: Provided placement extension and training on equipment through their internal budgetary arrangements. Review of journal.

Declarations and Statements

This work has not previously been accepted in substance for any degree and is not being concurrently submitted in candidature for any degree.

Signed: [redacted]

Date: 20/10/2023

This thesis is the result of my own investigations, except where otherwise stated. Other sources are acknowledged by footnotes giving explicit references. A bibliography is appended.

Signed: [redacted]

Date: 20/10/2023

I hereby give consent for my thesis, if accepted, to be available for electronic sharing after expiry of a bar on access approved by the Swansea University.

Signed: [redacted]

Date: 20/10/2023

The University's ethical procedures have been followed and, where appropriate, that ethical approval has been granted.

Signed: [redacted]

Date: 20/10/2023

Contents

Chapter 1 Introduction 1

Chapter 2- Theoretical Review and Motivation 12

2.1 Industrial motivation 12

2.2 Submerged Entry Nozzle 14

2.2.1 Background and Structure 14

2.2.2 Pre-heating temperature and time 28

2.2.3 Fundamentals of Raman and Model-Free Kinetics 28

2.2.4 Review of the application of Raman spectroscopy for carbon-bonded refractories 38

2.2.5 Review on application of Model-Free-Kinetics for carbon-bonded refractories 40

Chapter 3- Methodology 42

3.1 Model-Free Kinetics Approach 42

3.1.1 Fundamental Equations 42

3.1.2 Isoconversion Methods 43

3.1.3 Non-Conversion Method 46

3.2 Materials, Preparation, and Identification 48

3.3 Characterisation 52

3.3.1 Thermo-kinetic Analysis 52

3.3.2 Raman Spectroscopy Analysis 53

3.3.3 XPS Analysis 55

3.3.4 μ-CT Analysis 55

3.3.5 IET Analysis 56

3.3.6 LFA Analysis 56

Chapter 4- Carbon Oxidation Phase Profiling 57

4.1 Assessment of Non-conversion model free via oxidation profiling of Resin phase 57

4.2 Isoconversion Analysis of Resin Phase 61

4.3 Assessment of isoconversion predictive capabilities and mechanistic association to model-fitting and model-free approaches 67
4.3 Isoconversion Analysis of Graphite Phase..... 72
Chapter 5-Influence of preheat on oxidation kinetic profiling..... 79
5.1 Isoconversion Preheat Analysis of Resin Phase 79
5.2 Isoconversion Preheat Analysis of Graphite Phase..... 82
Chapter 6-Raman Oxidation Tracking and Assessment of Preheated SENs 85
Chapter 7-Synergistic uses of Raman with XPS and μ-CT to evaluate chemical and microstructural influence on oxidation 93
Chapter 8-Implications of preheat on thermal Shock profiling of carbon-bonded refractory 103
Conclusive Summary 110
Future Recommendations 111
Industrial Impact 112
References 114
Appendices 130
μ -CT of Large pore-network crack 130
Image Segmentation of μ-CT pores 130
Image Segmentation of μ-CT Carbon Matrix 131
Image Segmentation of μ-CT Carbon Matrix and Aggregate..... 131
Image Segmentation of μ-CT of All regions..... 132
Dampening Wave, and Frequency Velocity fityk fitted peak..... 133
Illustration of Lorentzian peak fitting of G and D peak..... 134
SEM and FTIR Scans for SEN samples..... 135

Acknowledgements

The best of journeys is one that requires you to grow continuously by overcoming a mirage of challenges and succeeding in them overtime. This industrial doctorate has been a worthwhile journey and I thank God for giving me the inner resolve to want to succeed and bring value to those that have entrusted me with this opportunity. As a person of faith, I know full well that I cannot thank God if I do not thank the people who have made it possible for me to be in this position. I am most honoured and grateful to my supervisors and the M2A team for their guidance and support.

I would like to dedicate a special thanks to Prof. Cameron Pleydell-Pearce, Dr Szymon Kubal, and Dr Liam Way for their supervisory role and support in the project. I have developed massively as a person both in technical and social terms through our many interactions. I will certainly miss learning from your wealth of experiences combined. I would like to extend this special thanks to Mathew C. Davies for his support in facilitating the industrial trials of the preheated SEN that I used in conducting this body of work. I am extremely grateful.

I would not have been able to achieve the majority of this work without the extra funding grants that I was able acquire to help me navigate COVID-restrictions and project change timeline. I am extremely grateful to The Henry Royce Institute for granting me x4 award to access advanced equipment and training in various facilities in around the UK (Grant Number: EP/R00661X/1). The first two proposals amounted: £ 11,000 and research conducted at Culham Science Fusion Centre – Material Research Facility. This amounted to £3000 per day for accessing additional days at NXCT Manchester University (for 2-days) and the other at the Materials Research Facility £5000. I am also grateful to NXCT Manchester University for offering me their free-access award of £3000 per day which allowed to me train and conduct X-ray Computed Tomography work for 3 days (EPSRC grant EP/T02593X/1), this is in addition to the Royce funding. I am extremely grateful to the UKAEA's Materials Research facility for allowing me to extend my stay within their facility in addition to the Royce funding to explore and do further testing with the WiTec Raman suite. A special thanks to HarwellXPS for accepting our proposal to conduct the XPS work that went into this project.

I would like to express further thanks to Dr Mark Coleman, secondary supervisor whom I have had the pleasure of benefitting from his company, expertise and advise on outreach activities. A special thanks to Prof. Peter Holliman for his kindness, approach and advise in both project and non-project matters.

A massive thanks to colleagues/doctoral counterparts that I have met who have left a remarkable memory for me which has made this journey much easier and enjoyable. I owe to their good nature and support to express my thanks to, Dr Wafaa Al-Shatty, James Grant, Dr Carlos Llovo, Dr Sarah Mugabo, and Dr Liam Cotton.

The one person I cannot thank enough with words for her support during this programme, is my amazing wife, Selma. I dedicate the efforts of this work to her and my two boys that I had during the doctoral programme. I would not have been able to do it without you. I am so lucky to have someone like you by my side.

The most important people to thank whom without their commitment and investment in me I would not have started this journey in the first place, are my parents, I am more than grateful for your prayers and support in wanting me to succeed.

Figures

Figure 1. The continuous casting process of steel making showing the position of SEN located between the tundish vessel and the mould during casting. a) Steel arrives at the continuous casting process in a ladle vessel which empties its content on the tundish vessel and then onto the mold for steel cooling and solidification. Slag is added to protect steel from oxidation and remove impurities. b) An actual image of a SEN during casting[4].1

Figure 2. Thermocouple trial (two images on the left) conducted on sponsor site. The SEN (middle image) is being gas flared or preheated outside in an open oxidising atmosphere with thermo-couples installed at various points along its length. The protective glaze coating protects the SEN from oxidation during preheating. The image on the far right is the inductive heating intervention undertaken on behalf of sponsor company to mitigate non-uniformity of heating. 14

Figure 3. The continuous casting process of a steel plant showing the various section of the casting operation. The pre-heated SEN is positioned between the tundish vessel and the mold after its installation or in casting position. Molten steel arrives in ladles and are emptied into

tundish before finally cooling with the help of mold and spray nozzles (image adapted to show position of SEN)[54]. 15
Figure 4. Depiction of the general manufacturing process of refractories, highlighting the route the SEN would take under “Fired refractories” (shaped refractories) according to Louis Pilato (image adapted with star symbol and thick and red inner border under Fired refractories to show the route of the SEN)[62]. 16
Figure 5 The influence on coking temperature on the biaxial flexural strength of carbon bonded refractories with the same carbon content of 33%. The higher coked sample shows lower strength at temperatures below 1200 °C due to thermal expansion mismatch theory of Luchini (i.e., it has higher pores or micro crack formation when cooling). Strength is observed to increase up to the coked temperature before decreasing as a result of newly generated cracks[64]. 18
Figure 6. Cross sectional image of the SEN adapted from Memarpor et al., showing the z-band, protective glass coating, alumina-graphite main bulk material and insulation coating locations[15]. 20
Figure 7. The effect of graphite on the carbon-based refractories systems. a) The effect of increased graphite flake shows an increased in bending strength adapted from cooper 1987, b) The increase in graphite content on the properties of magnesia carbon bonded refractory system showing an increase in thermal conductivity and a decreasing trend for both Young’s modulus and depth of slag penetration. 21
Figure 8. The electron interaction of catalyst with carbon proposed by Long and Skyes. a) Represent the electron configuration adopted when an oxygen atom is initially absorbed, b) and c) are the configurations adopted for easy evolution of carbon monoxide by transfer of electron to catalyst or forming a covalent bond with it, respectively, and d) represent the configuration that inhibits the evolution of carbon monoxide by accepting electrons from a donor which stabilises its structure [81,82]. 26
Figure 9. Adapted illustration of the different modes of light scattering phenomenon in a Raman instrumentation when an incident photon reacts with a polarisable sample. The arrow demonstrates the direction of excitation and de-excitation of molecules to various vibrational states involved in each type of scattering (Rayleigh, Stokes, Anti-Stokes, Fluorescence; E, referring to their associated energies)[89]. 30
Figure 10. An example a Raman spectrum highlighting the important aspects to consider when assessing a spectrum. The peaks intensity (useful for detecting concentration), width

(useful for detecting defects or doping) and position (useful for identification of molecules) are three key main features that can used to understand Raman components[88]..... 31
Figure 11. Raman spectra of a typical graphite like sample highlighting the most common of its peaks and the effect of stress-strain on the direction of the G-peak position. The D peak and the D' peaks are defect induced. The G peak is the sp2 representation of the bonding in graphitic samples and its shift in position can be used to assign stress/strain distribution. The 2D appears to indicate stacking/thickness of the planar structure of graphitic samples[90]. 32
Figure 12. Illustration of the Laser energy dependence on the peak shift position of D, D' and 2D/G' peaks. The D band is known to shift position with laser by approximately 50 cm-1 /eV, the D' shifts by approximately 10 cm-1 /eV and lastly the 2D/ or G' shift s by approximately 100 cm-1 /eV. The laser sensitivity of these peaks must be considered when conducting experiments[87]. 34
Figure 13. A silicon oxycarbide ceramic analysis of Raman showing stability of FWHM on the left and defect types on the right. a) nano-crystalline carbon FWHM stability with temperature change (C-11 and C-17; numbers denoting percentage of carbon present in the ceramic), b) defect types calculated for both C-11 and C-17 and position on master plot of defects found in modified graphene and graphite[92]. 35
Figure 14. The three SEN provided by sponsor company and sampling locations. A) Image of the three SENs, two of which are preheated (one for 3 hours and the other for 6 hours) and a Virgin SEN (that was not preheated). B) Shows the location (Port) of IET samples (of which, only two can be obtained per SEN) and the general samples for other characterisation techniques other than LFA. C) Shows the sampling location (which is labelled as base) for LFA analysis. 48
Figure 15. IsoMet precision saw cutting a subsection of the SEN piece (left), the middle image shows a cut sample for IET analysis being weighed, and on the far right a set of samples mounted on a stub in readiness of μ-CT-Xray tomography scan. 49
Figure 16. a) Shows the weight loss due to oxidation of carbon as a function of temperature increase for both the resin phase and graphite within the refractory the refractory. Peak positions of resin and DTG highlighted alongside their respective onset oxidation point b) shows the Ozawa Arrhenius Plot, c) Shows the Kissinger Arrhenius plot. The heating rate is β; Tp denotes peak temperature[24]. 58
Figure 17. The isothermal experiment at 510 °C which is initiated after the gas flow was switched from an argon source to air. a)The DTG rate of mass loss against time is shown as

a brown line. The purple line shows the conversion in graph with a peak DTG measured at 40% conversion. b) Represents the TGA plot of weight loss with time (brown line). Temperature profile and Gas-Switch instances are also depicted in each graph[24]... 60
Figure 18. Graphical representation of the Arrhenius plot of a) OFW and b) KAS; linear regression applied on conversion with each slope and intercept producing an activation energy and Arrhenius constant. c) Graphical illustration of compensation effect displaying the linearity between “ln A” and activation energy. d) Shows the activation energy values for both KAS and OFW with respect to conversion (KAS displaying higher kinetic parameters but sharing the same trend)[24]..... 62
Figure 19 Graph showing the change in entropy change versus the Arrhenius parameter in this case represented as logarithmic value “ ln A”. Adapted from already publish work to include the thermodynamic descriptors of SAC, SR, and ΔS, with arrows indicating directional increase or decrease in the gap between SAC, and SR [24] 64
Figure 20. “X” the temperature integral approximation derived from KAS and OFW against the average temperature in each conversion (heating rate of 11 °c/min was used and X=E/RT). The X values of the OFW stayed within its limits of approximation and was therefore considered more accurate than KAS..... 66
Figure 22. a) Time taken to reach a set conversion point versus temperature (model generated for predicting isothermal experiments). b) Isothermal experimental data at 510 °C, 540 °C, and 570 °C for the time taken vs temperature. c) Theoretical prediction for 510 °C compared with experimental data. d) Theoretical prediction for 540 °C compared with experimental data. Standard error is used to assess the difference between theoretical and actual experimental values[24]..... 68
Figure 23. Z(α) master plot of common solid-state theoretical models compared against experimental plot. Z(α) theoretical output was calculated by multiplying the differential with the integral forms of reaction mechanism equations below. Experimental values were determined using dα/dt (3°C/min) in the equation: Z(α) =(dα/dt) T2. [π(x)/βT][30]; where π(x) can be determined by the fourth rationale of the Senum-Yang approximation[116] 71
Figure 23. A graphical representation showing the oxidation of both resin and graphite oxidation as a function of temperature increase. The graphite maximum DTG peak temperature are highlighted for reference. 73

Figure 24. DTG time derivative of percentage weigh change as function temperature increase during oxidation (%/min) of graphite showing the effect of heating rate on the mechanisms influencing oxidation. 74
Figure 25. The Arrhenius isoconversion plot of a) OFW method and b) the Friedmann method used for profiling the oxidation behaviour of in the graphite phase of a virgin sample. 75
Figure 26. Graph of activation energy and ln A for various model free-kinetic models: Friedmann, OFW and Vyazovkin. Each models shows their predictive capability in analysing the graphite phase in a virgin refractory sample. 77
Figure 27. The use of kinetic triplet to predict experimental data with the use of Vyazovkin kinetic parameters. 78
Figure 28. A graph showing the Vyazovkin kinetic parameters of activation energy and Arrhenius constant for a virgin SEN, 3-hour preheated, and 6-hour preheated when analysing the resin phase of a carbon-bonded refractory composite 80
Figure 29. Entropy (change) evaluation of preheated samples (3-hour vs 6-Hour preheated): Analysis of the resin phase applied for the resin phase only. 81
Figure 30. A graph showing the Vyazovkin kinetic parameters of activation energy and Arrhenius constant for a virgin SEN, 3-hour preheated, and 6-hour preheated when analysing the graphite phase of a carbon -refractory composite 83
Figure 31. Entropy (change) evaluation of virgin SEN sample, and preheated samples:3-hour and 6-Hour. The analysis comprises of the graphite phase only. Entropy is used symbolically to assess the magnitude difference between SENs 84
Figure 32. WiTec cluster analysis map output data, with location tracking of different carbon regions in a sample comprising of 40,000 data points. Automatic colour assignment is given unless changed manually when cluster technique is applied to show grouping of similar clusters shown. The green colour selected is a single Raman spectrum of carbon belonging or affiliated to cluster 3 averaged map of all cluster within the selected group. The green represents 1 out of 4 cluster that can be represented graphical form shown in Figure 33. 86
Figure 33. Re-position of the graphical output of 4 carbon cluster to select the best feature less impacted by the proximity of substrates around it; a) and b) are different representations from cascade mode to single merge respectively. 87
Figure 34. a) A Raman depth scan profile with applied cluster mapping using WiTec software to distinguish carbons. The top Raman spectra in red is Graphite (region) and the

one below it in blue is the resin (region). b) and c) are their associated locations mapped in yellow with each pixel representing a Raman spectrum. The black regions are for masking other carbon regions affected by substrates[24]. 88
Figure 35. a) Crystallite size measured for resin as a function of oxidation time, b) Graphite crystallite size as a function of oxidation, c) The change in ID/IG ratio of resin phase with respect to oxidation and d) The ID/IG ratio change of the graphite phase with respect to oxidation point[24]. 90
Figure 36. Effect of titania suppression on the G and D peak clusters at 2-minute oxidation point. (a) 4 cluster mapped with their respective locations; Two clusters show high intensities of titania peaks: 156, 399, 503, and 615 rel.cm-1. (b) b) A single graphical output from the cluster showing the peaks of titania and suppressed signals of the carbon peaks (G and D). 91
Figure 37. Changes in peak components due to substrate effects; from 3-minute oxidation to the 4-minute oxidation time point. a) component cluster of resin least affected at each oxidation level, and b) component of the least affected graphite cluster at each oxidation level. 92
Figure 38. EDS map of elements of in the refractory that can impact signals obtained by Raman (Aluminium silicon and titanium) using the oxidised sample at 1 minute oxidation timepoint..... 92
Figure 39. Cluster lateral Map of a virgin (Top), 3-hour preheated (Middle) and 6-hour preheated sample (Bottom) showing distribution of carbon and their respective location.The least affect cluster in each map be resolved by intensity of D peak and whether data is influenced by aggregate. LG represent least graphite rich region, LR represnts least affected resin rich region. A is showing an area coverage of a single cluster. Arrow pointing upwards due to higher defect and downwards due to lower defect. 95
Figure 40. Combine (averaged) map of the entire cluster in each SEN sampling showed a clearer difference in terms D peaks Intensities. The D-peak decreases from image labelled Top (Virgin SEN sample) to Middle (3-hour preheated SEN sample) and then Bottom (6-hour preheated SEN sample) which has the lowest D-peak intensity. 96
Figure 41. The crystallite size of graphite and ID/IG ratio of virgin, 3-hour preheated, and 6-hour preheated SEN sample determine. 97
Figure 42. a) The average D-parameter of the combined etched and non-etched sample for virgin, 3 hour preheated and 6 hour preheated sample, b) Shows the %atomic concentration of the averaged combined C1s peak components for virgin (blue), 3-hour preheated (orange)

and 6-hour (grey) samples, and c) is the binding energy (ev) of the averaged combined C1s peak components for virgin (blue), 3-hour preheated (orange) and 6-hour (grey) samples. 99
Figure 43. a) An xps survey scan of non-etched sample for identification for C1s peak, b) Deconvolution fitting of peak components into the C1s carbon peak, c) Carbon auger peak fitting and synthetic differential to produce the D parameter from d) graphical representation of the result produced from the differential of carbon auger peak (fitting of the component with sp2/sp3 type background gives a FWHM equivalent to the D-parameter)..... 100
Figure 44. CT-scan native measure of Equivalent Diameter of the segmented refractory pores and b) Sphericity of pores calculated as reciprocal of the native measure of feretShape3d using avizo software. 101
Figure 45 Results of IET test showing Elastic Young's Modulus (red diamond), Natural frequency of vibration (brown -circle), and Dampening factor Q (purple - square) for the virgin 0-hr, 3-hour preheated (3-hr) and 6-hour preheated (6-hr) sample. 105
Figure 46. a) Image shows the thermal diffusivity of a refractory SEN sample as function temperature, b) show the change in Cp as and c) represents the changes in thermal conductivity all as a function of temperature increase for the Virgin SEN sample (0-Hr), 3-hour preheated SEN (3-Hr) and 6-Hour (6-Hr) preheated SEN sample. 106
Figure 47. Resin cluster map of the least impacted signal by the substrate effect scanned with high temperature modulated Raman spectroscopy. Pyrolysis effect, followed by microstructural changes are observed with the decrease in D-peak and increase in 2D-peak exposing the graphite phase. 108

Tables

Table 1. An EDX elemental analysis of the Virgin SEN, highlighting the major composition of elemental aluminium and silicon present that make up the refractory. These metals in the form of alumina and silica were observed by utilising ATR-FTIR analysis in conjunction. The SEM Hitachi TM4000-plus coupled with EDX SSD was used to map and analyse three areas and combined the results shown 50
Table 2. An EDX elemental analysis of the 3 hours preheated SEN (3-hour), highlighting the major composition of elemental aluminium and silicon present that make up the refractory. These metals in the form of alumina and silica were observed by utilising ATR-FTIR analysis in conjunction. The SEM Hitachi TM4000-plus coupled with EDX SSD was used to map and analyse three areas and combined the results shown. 51
Table 3. An EDX elemental analysis of the 6 hours preheated SEN (6-hour), highlighting the major composition of elemental aluminium and silicon present that make up the refractory. These metals in the form of alumina and silica were observed by utilising ATR-FTIR analysis in conjunction. The SEM Hitachi TM4000-plus coupled with EDX SSD was used to map and analyse three areas and combined the results shown 51
Table 4. The activation energy and Arrhenius parameter values for both Kissinger (α) and Ozawa (β) are displayed. The symbol “(*)” is indicative of Arrhenius parameter using variable heating rates with Kissinger’s equation re-arrangement. The symbol “(Δ)” refers to the Arrhenius derived from intercept of the slope[24]. 59
Table 5. The isoconversion oxidation kinetic predictions of the Ozawa Flynn Method. "*" is indicative of the optimised “ln A" factor through the use of the compensation effect[24]. 63
Table 6. Shows the Vyazovkin activation energy values with respect to conversion that served as inputs for calculation improvement in this section 68
Table 7. Kinetic and thermodynamic parameter obtained from Vyazovkin method. An improvement was applied to the values a and b of the compensation effect by using the predicted Arrhenius constant from the kinetic software that allow for a better prediction of entropy compared to the earlier report values using OFW compensation effect values of a and b. 81
Table 8. CT-Scan measures of the segmented pores for a virgin sample (0-hour), 3 hour preheated SEN and 6 Hour preheated SEN. The main discriminatory measures are the

average aread3d and average volume 3d which show a decline in with respect to preheat 102
Table 9. Table of G-Peak shifts peak position in support of the microstructural evolution at high temperature. Cluster A: represent clusters least impacted by substrates effect; Cluster B and C are clusters affected by substrate effect (graphite and aggregates). 109

Nomenclature

DSC	Differential Scanning Calorimetry
TGA	Thermogravimetric Analysis
SDT	Simultaneous DSC-TGA
DTG	Differential Thermogravimetric
DTA	Differential Thermal Analysis
XRF	X-ray fluorescence
XPS	X-ray Photoelectron Spectroscopy
μ-CT	micro–X-ray Computed Tomography
LFA	Laser Flash Analysis/Analyser
IET	Impulse Excitation Testing
EDS	Energy Dispersive X-ray
XRD	X-ray Diffraction
SEM	Scanning Electron Microscope
A-FTIR	Attenuated Fourier Transform Infrared Spectroscopy
SEN	Submerged Entry Nozzle
OFW	Ozawa-Flynn-Wall equation
KAS	Kissinger-Akahira-Sunose equation
dα/dt	Rate of Reaction Per Time (time rate of a conversion mass ratio)
dα/dT	Rate of Reaction Per Temperature (temperature rate of a conversion mass ratio)
α	Conversion
β	Heating Rate
K	Rate Constant
E	Activation Energy

Ln-A	Natural Log of Arrhenius Constant
A	Arrhenius Constant/Pre-exponential Factor
Q	Dampening Quality Factor
Q^{-1}	Dampening Friction
T_p	Peak Temperature (DTG)
$T_{\alpha,i}$	Corresponding Conversion and Heating Rate Temperature
$f(\alpha)$	Reaction Model (Differential equation)
$g(\alpha)$	Reaction Model (Integral equation)
p(x)	Temperature Integral approximation
C_p	Heat Capacity
R	Universal Gas constant
ΔS	Total Entropy (Change)
ΔH	Enthalpy Change
ΔG	Gibbs Free Energy Change
h	Planck constant
k_B	Boltzmann constant
MFK	Model Free Kinetics

Chapter 1 Introduction

The submerged entry nozzle (SEN) is a carbon bonded refractory tube that facilitates the passage of molten steel into the mould during the continuous casting process of steel manufacturing [1–4]. The continuous casting process being one the most important processes of steel making in terms of temperature control, production rate and steel quality, need high temperature resistant materials to help regulate the aforementioned features [1–4]. The SEN is therefore a flow control device used to ensure a continuous production process is maintained (see Figure 1). It is also critical in shrouding the molten steel to prevent unwanted oxidation or the loss of heat which can negatively impact the steel quality [1–6]. Fluxes or slags also share the same objective in of preventing oxidation and improving steel quality at various stages in the process [4,7–9]. Since refractories are high temperature resistant materials (i.e., good insulators), carbon is added into the material to improve its thermal conductivity and thermal shock resistance[10–13]. The carbon within the refractory SEN is protected by an outer glaze in the case of SEN at-least during its preheating stage heated correctly[1,14,15].

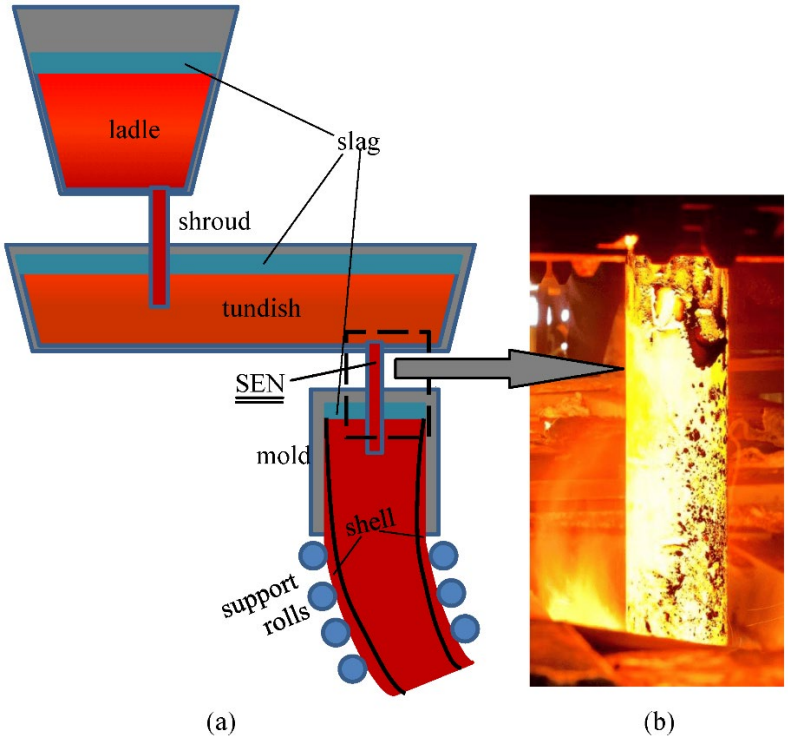

Figure 1. The continuous casting process of steel making showing the position of SEN located between the tundish vessel and the mould during casting. a) Steel arrives at the continuous casting process in a ladle vessel which empties its content on the tundish vessel and then onto the mold for steel cooling and solidification. Slag is added to protect steel from oxidation and remove impurities. b) An actual image of a SEN during casting[4].

The type of SEN discussed herein is preheated to temperatures of between 1000 °C -1200 °C as a preparatory step before coming to contact with molten steel (i.e., casting)[1,2]. The preheating time can take between 1 and 6 hours at sponsor company site/steel user. This preparatory step is essential in preventing thermal shock failure of the SEN[16,17]. It also prevents unwanted cooling resulting in the solidification of molten steel on the SEN itself, which negatively impacts steel quality[4,16]. In terms of failure modes, the SEN is therefore susceptible to a combination of oxidation and thermal shock failure if improperly preheated[1,2,4,16,17].

In the year 2018, major pre-heating failure incidents at sponsor company site raised concerns about the implications of their process towards refractory behaviour and its general integrity when supplied[17,18]. Additionally, in the first three months where these high incidents of failures were observed, 239 SENs were scrapped after not being used post preheating (i.e., SENs have gone past their preheating time limit)[17]. These unused SENs were evaluated to be equivalent to loosing 18 pieces of SENs per-week, which translates to a yearly loss of £137,000[17]. Failures incidents greater than 2% of total SENs used weekly, if consistent over a period, calls for immediate attention to either a problem with the material integrity or the steel practises or process (i.e., preheating preparatory step)[17–19]. The latter being more common as to the reason why failures may occur and became a key driver for the project[17–19].

Temperature, although a key process parameter is not measured during or post preheating [1,17,20]. It is only during trials of new products or major failure incidents that the SEN's temperature is verified [1,17,20]. This can be achieved by mounting thermo-couples directly into the SEN or indirectly using a thermal imaging camera[1,17,20].The lack of data and difficulty in obtaining live measurements pertaining to the SEN (i.e., monitoring temperature of SEN during preheating, temperature of SEN during off-gas time and temperature during casting) creates a need to find cost effective solutions to determine process implication on the SEN [1,17,20]. As well as the aforementioned challenges to monitor process parameters continuously, it may not even be financially feasible to adopt this idea when weighed against the inexpensive nature of the SEN.

This therefore begs the question as to how the SEN's integrity should be monitored in the absence of process data. The following questions provide the basis of this research:

- Is there a way to profile the integrity of the product when supplied for the purpose of standardisation? This should also help differentiate material integrity issues originating from supplier (if they were to occur) to that of the steel user's process.

- Subsequently, will this integrity profile change when the SEN is undergoing its preheating regime within the steel user's process?
- What is the implication of the above profile change? How may it translate to performance, so that value can be obtained in:
    1) Improving failure classification.
    2) Improvement of preheating practises by regulating preheat time and installation strategies. This impact of which could lead to strategies that prevent failures and reducing the number of unused SEN by adopting better strategies.
    3) And in future, be able to create data driven statistical models/or machine learning models that predict both the type of failure and the process parameters influencing it using the material itself. This may be achievable by training the generated datasets from these profiles in combination with experimental data simulating those of the steel user's process. This will also ensure failure classification is backed evidence-based research.
- Are there novel approaches that can be used to examine the product directly despite challenges related to its curved and irregular geometry of faulty/affected areas. The ability to analyse very small irregular regions at failure can be challenging and tedious especially if a mechanical testing approach was required for thermal shock assessment. Most mechanical testing equipment for refractories may require standard shapes and sizes making it difficult to examine and quantify the effect of thermal shock in service[21–23]. Consequently, the avoidance of tedious sample preparation as well as having of flexible method that can accommodate a range of sizes will be a key factor to consider.
- Lastly, the results of the analysis produced from these approaches should be quantifiable and accessible in such a manner that non-refractory experts, if need be, can be trained to use it. The variables or data produced will also be useful in future studies addressing the predictability of missing process parameters and failure classification.

The objective of this study will therefore be geared towards improving the preheating process knowledge implication on the SEN, when process information itself is insufficient. This will involve finding solutions comprising of profiling techniques and experimental approaches that can overcome a myriad of industrial challenges highlighted in the research questions above. A profiling technique can help standardised what is expected in terms of

performance when the product is supplied and the profile to be expected when the product/or SEN is treated correctly by the steel user. It will also help shorten the time it takes to determine the origin of failure taking away the need for costly plant and supplier investigations.

In this study, the integrated carbon in the SEN will be used as a marker to track and profile the refractory behaviour using sophisticated, yet simple to use techniques[24]. In terms of tracking carbon, the main technique and approach investigated will be the use of Raman spectroscopy and its synergy with Model-Free Kinetics (MFK)[24]. Their extensive flexibility in dealing with varying sample geometries, simple sample preparation needs, sensitivity for detecting different carbon phases and efficiency in analysis time, makes them an excellent candidate for the purpose of this work.

In the case of Raman imaging, sophisticated in-built propriety software algorithms have emerged that allow for automated detection of phases or features based on an image clustering technique (which is one out many statistical multivariate analysis technique)[25]. The way in which this would work for a user and for the purpose of this study is to firstly acquire the mapped area to investigate using the WiTec Raman instrument (i.e., create the settings required to program scans automatically). A single Raman spectrum can be obtained within a short time period of about ~ 0.66ms (milliseconds), with each scan representing an image pixel that can be grouped by features of similarities (i.e., this is what the cluster technique does) [25]. Once a map is acquired, the user has the option to select the cluster technique as a method of analysis and can choose the number of clusters (i.e., 2 or more) that the software will use to group features of similarity[25] This number will be decided by the user[25]. It will depend on the sample and user knowledge about their sample[25].

The benefit of this method allows one to know and expect the same cluster or set of clusters when comparing it to another sample that is of the same type or composition effectively profiling what to expect[25]. If a sample treatment were to change slightly by heating as an example, the same or similar set of clusters that is expected can be used to learn about what these changes may mean (i.e., if the comparison afterward is done across sample by way of regression analysis). In other words, is there a trend observed between the non-heated and heated sample? If cluster A is expected to exist in both samples, has it changed slightly, and if it did, this can be attributed to changes in sample treatment. Therefore, cluster A will be a good probing mechanism to track changes that are otherwise

difficult to examine in terms of sensitivity, time, and effort and therefore not align to the objective of this study.

It is important to note that the cluster analysis is applied only to each sample given (i.e., not across samples). Other analysis methods (i.e., regression analysis based on three or more points applied across samples of the same type, where a similar population of clusters may exist) can be used to assess the known and acquired cluster to expect when comparing across samples.

Interestingly, another scenario to consider when applying the cluster technique is the possibility that due to the treatment of a comparator sample or due to a random scan location, samples may no longer share a similar cluster marking or appear significantly different (i.e., when comparison is done across samples). There may be localised regions within the sample type that contain a specific composition (i.e., elements affecting the cluster signal) that only manifest themselves when those areas are scanned (i.e., based on distribution within sample) or the effect of certain compositions are only being realised due to the degree of change within the comparator sample. Therefore, scarcity or distribution of composition, the degree of change due to sample treatment and the area coverage that can be accommodated by the Raman scan are important factors considered in this study.

Without the use of the cluster technique that relies on thousands of scans performed (i.e., utilising the Witec Confocal Raman mapping suite) in a selected area (acquired within a short period of time), it may be extremely difficult to gain insight on carbon-bonded refractory composite especially if the impact of preheating on microstructure is subtle (i.e., in the context of a profiling objective). The aforementioned statement has to be put in the context of research questions outlined previously. The Witec software and Raman suite will be used in this study to explore the clustering technique with the objective of finding the most suitable method in examining the SEN's behaviour/or profile. Any new insight uncovered during the use of the clustering technique will be valuable. This can manifest itself as a novel method to probe microstructural, surface area changes, and chemical influences governing oxidation resistance, carbon mineral integrity or even provide insight on the use of the technique and limitations. It also worth noting that the Raman technique is a non-destructive method that identifies, or fingerprints molecules of interest based on in-elastic scattering of light[25].

In the case of MFK, the ability to measure kinetics (and in some cases extrapolate thermodynamics) directly from thermo-analytical data alone, without prior knowledge of reaction mechanism or models, makes it a valuable approach in the assessment of the SEN

[24,26,27]. The adoption of this technique should help overcome a myriad of sample challenges and with minimal sample preparation required.

However, it is important not to confuse classical kinetics with MFK (which combines kinetics with thermo-analysis)[26,28]. The thermo-analysis approach does not require a reaction mechanism [26,28]. Kinetic parameters obtained from MFK such as activation energy (E) and pre-exponential factor (A) are dependent on conversion [26,28,29]. The E in MFK represents the sensitivity of the overall reaction rate as a function of temperature[26]. The A value, on the other hand represents the intensity of the reaction rate[26]. The decrease of E will increase the rate and the increase of A will have the same effect[26]. The conversion of matter itself is evaluated as a function of temperature directly or indirectly using thermo-analytical methods such as thermogravimetric analysis (TGA) , differential thermogravimetric analysis (DTG), differential thermal analysis (DTA) and differential thermal analysis (DSC) [26,28,29]. It is recommended to use more than two heating rates (3-5) and to understand that the accuracy of the arrhenius parameters depend on the extreme heating rates or temperatures[30]. It is therefore crucial to replicate test runs on these extreme temperatures for better predictions[30]. Both E and A in MFK are correlated in such manner that their simultaneous adjustment does not change the overall reaction rate [26]. This behaviour is called the compensation effect and has been attributed an equation to show this dependency[26,27,30].

In classical transition state theory, the frequency factor which is analogous to A behaves very differently and is independent of activation energy[26]. Rate as known in the classical sense is controlled by height of an activation energy barrier (which acts a boundary between reactant and product) and the vibrational frequency of the activated complex[26,31]. The classical theory also deals with single chemical reactions and does not consider the effects of medium[26,28]. Even the reaction mechanism in form of f(α) or g(α) should not be confused with that of early kinetic mechanism originating from homogenous kinetics[29]. The famous Arrhenius equation also came from homogenous kinetics in its early infancy[28]. In MFK isoconversion method, the concept that E changes with conversion (α) (denoted as E_α) has been misunderstood and wrongly perceived as a mistake[26]. The expectation that E must be constant is predominantly influenced by undergraduate physical chemistry text[26]. However, the idea of a constant E will only be valid for single step gas phase reaction occurring in the absence of a medium[26]. The physical parameters of a medium which also changes as a function of temperature therefore becomes a key factor in determining the height of free energy barrier[26]. Having

E_α values in MFK represented as constants (i.e., multiple constant values determine for each conversion measured) therefore reflects changes occurring in the medium[26]. Aside from the theoretical implications, the only practical need for obtaining reaction mechanisms would be to predict the experimental rate and especially the rate outside the experimental region for it to be useful in any sense[26]. In essence if the kinetic triplet (E, A, and f(α)/or g(α)) which can also be obtained in MFK is insufficient in its practical sense (i.e., in describing experimental data and predicting kinetic curves outside experimental region), then applying the theoretical meanings of classical kinetics will not be necessary[26]. Although, E and A do play a similar role to activation enthalpy and frequency factor with regards to rate, the stringent focus on the interpretation of classical kinetic equations to judge MFK has created misconceptions as highlighted[26]. Meanings of E and A can simply be taken as described previously in the context of MFK and can be supported by evidence of measured or known characteristic that influence the reaction process if known.

Furthermore, the main purpose of using MFK in this work will be to profile the sensitivity of oxidation as a function of preheating. A great portion of the work will be geared towards understanding the various ways in which MFK can be used. This will be done initially by evaluating a virgin SEN. Thereafter, a selected approach will be used in assessing the virgin SEN, 3-hour preheated SEN and a 6-hour preheated SEN, against the objective of this work. For the purpose of emphasis and not confuse classical kinetics with MFK, the units of A will be annotated in the methodology section alone. It is known that units of A do vary, however for the purpose of this work the time unit for A is generally measured in the reciprocal per minute (i.e., A will adopt the unit, 1/time unit: measured in minutes)[32–38]. Nevertheless, wherever there is a need to adopt a particular unit if appropriate (i.e., having units of per second as an example for A) in order to perform a calculation with a classical kinetic equation, the appropriate units can be assumed or determined[31–35]. Neither the order of reaction nor the mechanism or reaction model will be the focus of this study and therefore cannot be used to dictate the units of rate or the kinetic parameters obtained. It is worth noting that MFK kinetics parameters of both E and A will be derived graphically and equations do not need solving directly. This is owed to the simplicity of the method.

The oxidation kinetics of a carbon bonded refractory is sensitive to porosity and chemical reactivity of carbon surface area [11,39]. At low temperatures below 950 °C, oxidation is governed largely by chemical reactivity of available surface area of carbonaceous matrix

(graphite and resin), and to a lesser degree pore structure [11,39]. At higher temperatures above 950 °C, kinetics is controlled mainly by pore structure through gaseous diffusion permeability and influenced lesser by chemical reactivity [11,39]. Pore structure and chemical reactivity are both controlled by the mineralogical grade and the way in which the product is manufactured. The oxidation profiling will therefore be complemented with techniques that probes these chemical and microstructural features. This will involve the use of micro–X-ray Computed Tomography (μ-CT), and X-ray Photoelectron Spectroscopy (XPS).

The graphite and the binder phase (resin) microstructure (i.e., carbonaceous material within the SEN) are expected to have gas entrapment pores and calcination cracks akin to graphite application in nuclear graphite applications[40,41]. Calcination cracks are mostly linked to closed porosity resulting from volumetric shrinkage[40]. However, gas entrapment pores are associated with open porosity within the binder phase[40]. The shape, orientation, and volume fractions of pores may be useful as a discriminator value to profile the SEN at minimum. This will ensure that the expected microstructure at various stages of the SEN is known. The significant deviation of the expected in future will suggest either a material integrity issues or process implications (i.e., deficiency lies within the process not the material). The resolution used with μ-CT will be suitable for analysing the aforementioned pore structures[41]. For the purpose of profiling, the images will be pre-processed from the inner bulk material away from regions close to the protective coating which can chemically react with inner bulk material and affect the microstructure around it (i.e., on the edges closes to it)[14].

The μ-CT is in fact a powerful non-destructive technique for microstructural evaluation that will allow samples to be tested as received[41,42]. It helps circumvent tedious sample preparation and can deal with the brittle/fragile nature of the material. It has superior software capabilities for segmenting phases, 3-D volumetric image analysis quantitative in results, can be coupled with deep learning for automatic finger printing[41,42]. Conventional techniques such as optical microscope and scanning electron microscope (SEM) are useful in certain scenarios but requires significant effort for quantitative image analysis[41]. There is also a risk of not gathering enough images that describes the microstructure analysed and the difficulty of handling porous or fragile materials[41]. These microscope techniques are often employed where there is sufficient knowledge that can be gathered by evaluating fracture surfaces or surfaces where oxidation and non-oxidised are easily distinguishable[41]. The aforementioned challenges remain with

regards to these standard microscope techniques and for the purpose of this work it is the inner bulk microstructure that is of interest which may not oxidise in a manner that is easily detected if evaluated by these tools.

Raman and XPS will complement each other in terms having the ability to probe the chemical structures of the carbon phases present [43,44]. The local chemical order and long-range crystalline order of carbons are extensively diverse in terms of structures that can exist[45]. The large chemical differences observed is also attributed to their versatility in bonding chemistry or bonding hybridisation (i.e., sp^1, sp^2 and sp^3)[45]. It is these structures that influence the properties of carbon such as their chemical reactivity, physical and electrical properties[43,45]. Carbon atoms can be arranged according to their crystalline (graphite, diamond, fullerene) and disordered structures (glassy carbon, amorphous carbon, graphitic amorphous carbon etc.)[43,45]. Raman has become a standard tool for probing carbons due to their capability of evaluating short, medium, and long-range order[45]. The limitation in other methods not being able to probe disordered carbons sufficiently (an example being X-ray diffraction) gives Raman this precedence[45]. In this study the carbonaceous material consists of a mixture of resin (disordered) and graphite (crystalline) embedded within a refractory aggregate mixture (comprising mainly of alumina aggregate)[46–48]. By utilising Raman with the Witec cluster image analysis technique, a better insight can be observed in terms of distinguishing the carbon phases, their chemical structures and surface area changes impacted by preheating.

The Raman technique is susceptible to suffer from bulk effects which essentially arise from compounds/or elements within the composite that causes a change in the carbon signal/or signature that would not have existed if there were not present[44,49]. The XPS, being more of a surface sensitive technique is less impacted by this bulk effect and will therefore compensates for the affected Raman signals[44,49]. XPS will be used to help understands whether the chemical structures of carbon changes (i.e., based on changes of carbon order determined by D-parameter scale[43]) with respect to preheat. The expected order of carbon will be measured for the virgin and compared to those of the preheated SEN. Since graphite is considered more ordered than the resin it is expected to be more resistant to oxidation. Values obtained defining this order (i.e., where their chemical structure lie within the D-parameter scale referenced against known values of graphite) and can be used to assess or rank the potential chemical reactivity (by way of inference) of the carbons present within the SEN[43]. The D parameter has a liner relationship to the so called

sp^2/sp^3 ratio[43]. Graphite is at one end of the scale with only sp^2 hybridisation whilst diamond is the other of the scale with only sp^3 hybridisation[43]. The D parameter for pure graphite is documented to be 22.5 with 100% sp^2[50]. The lower the D value as would be expected in the carbons analysed the lower this sp^2 percentage[43,50]. This will be due to an increase in sp^3 which measured more in bulk by Raman using band known as the D-band (i.e., defect band) [43,50].

Given that the carbonaceous matrix of the refractory presents itself akin to a composite, the mixture poses a challenge where each area scanned will be influenced by both carbons (resin and graphite will co-exist in each scan). This is where the WiTec software cluster technique will be extremely useful, when deciphering carbon phases in the case of Raman. It is important to also emphasise that the samples will be handled and analysed as received with minimal sample preparation if any at all to maintain the microstructures found and to meet the industrial objective of this work. It has been evidenced that polishing of graphite sample also influence Raman signal and causes overestimation of intrinsic structural properties[51]. The label free non-destructive technique (i.e., Raman) will be helpful in overcoming tedious sample preparation, analysis time, provide quantifiable results which are easily accessible for non-experts of the material. The inner bulk material will be probed for part of the study dealing with comparative analysis of the virgin SEN, 3-hour preheated SEN and the 6-hour preheated SEN. This will be away from surface regions that could be impacted by the protective coating and to ensure that the carbon markers and the microstructure surrounding it are profiled effectively.

It is believed that longer preheating may increase the risk to oxidation, and a shorter preheat regime increases the risk to thermal shock [1]. For the latter point, it is important to know whether thermal properties and thermal shock resistance of the carbon-bonded refractories change during preheating. The Laser Flash Analysis/Analyser (LFA) which is another non-destructive technique will be useful in assessing the thermal property changes of the bulk inner material (thermal diffusivity, C_p, thermal conductivity) as a function of preheat time. The LFA will also be used to gain insight on microstructural changes and may prove useful as a profiling tool for the SEN. The impulse excitation technique (IET) is the final non-destructive technique and is used specifically in this instance for assessing the thermal shock resistance of the SEN. The IET measures the elastic Young's modulus and dampening from the vibrational frequency response of an excited sample[22,23,46]. The elastic Young's modulus property is sensitive to microstructural changes as well as thermal shock changes in the material[22,23,46]. The dampening measurement is more tailored

towards measuring faults caused by thermal shock and therefore provides a targeted result[22,23,46]. IET is in fact more sensitivity to larger voids or macro-crack networks useful for the analysis of thermal shock[23].

It is known that traditional thermal shock testing in laboratory environments does not reflect the true nature of refractory thermal shock behaviour in-service for composites i.e., the ΔT_c critical temperature difference (that induces thermal shock) in Hasselman equation cannot be accurately associated with the true ΔT_c in service, if taken from quench experiments[23]. Given that the microstructure of carbon-bonded refractories is complex (composites), its fracture behaviour and its transient thermal stress behaviour in a thermal transient condition is difficult to examine (if not impossible for the latter analytically)[23]. Efforts are always geared towards both experiment and theory to inform design application since no unified theory can suffice all composites[23]. However, with the use of dampening and elastic Young's modulus from IET, the changes in microstructures associated with their thermal shock resistance can be profiled effectively.

Lastly, the introduction of μ-CT will be useful in future failure classification studies of thermal shock if macro-network cracks are profiled using a different resolution. It will also be extremely useful for overcoming challenges associated with the analysis of smaller targeted samples having irregular shapes that do not possess the appropriate handling dimension for IET or other bulk mechanical testing methods. Introducing this technique for the purpose of microstructural evaluation to support the inner bulk oxidation sensitivity profiling part of the study will therefore be the catalyst to inspire alternatives concepts in future.

Discussed in the remaining sections in brief, will be the industrial motivation, methodology, product, and process knowledge surrounding the SEN. A review on feasibility and novel insight that can be gained when using Raman spectroscopy with MFK will be addressed. The sections to follow, starting from chapter 4, will focus initially on gaining an understanding and appreciation of the variety of ways in which MFK approaches can be used. Due the diverse feature of MFK a great portion of the work will be directed to decipher it. This is subsequently followed by chapter 5 which deals with the industrial application (i.e., looking into the effects of preheat) and the value that can be directly derived from MFK analysis. It will focus less on equations (as only a single selected approach will be used) and more on conveying the meaning of results. Raman is then introduced in sections, thereafter, providing a unique insight on the method development steps that would guide how the SEN should be characterise using its carbon

signatures, depth scan (for method development to gain insight by oxidising sample in a laboratory environment) vs lateral scan (for evaluating the actual SENs as received) and evidencing the use of image cluster technique. The Raman chapters will be supported by XPS and μ-CT analysis to evaluate potential chemical and surface area changes that may influence the oxidation kinetics of carbons. Finally, in chapter 8, the effect of preheat on the thermal shock resistance will be addressed.

Access to specialised equipment (particularly with the use of IET, confocal Raman with WiTec software suite, temperature modulated fixture for Raman, μ-CT) was obtained externally through a competitive grant proposal bid accompanied with a stringent timeframe to conduct the work. Therefore, the planning of this work needed to be done in a manner that best makes use of the available time and resource and in effect shapes the organisation of the thesis. The methodologies or approaches used therefore aim to lay the foundation on profiling carbon-bonded refractories in the manner described previously on the objective of the study.

Chapter 2- Theoretical Review and Motivation

2.1 Industrial motivation

High incidents of preheat failures occurred in sponsor company (steel user) beyond levels that called for supplier investigation in the year 2018[17,18]. The investigation efforts from sponsor company were very much reliant on the supplier data about their manufacturing processes and preheating trial results conducted on sponsor site[17,18].

Investigation by the supplier at sponsor company site indicated that the fault was mainly due to the sponsor company's installation/preheating practices, in particular, preheating burner misalignment[17,18]. Thermo-couple trials were conducted to confirm that the misalignment of burners did in fact cause the SEN to be under heated[17,18]. The SEN's temperature distribution also indicated high levels of temperature mismatch during heating. Adjustments to the burner and the chamber were made to rectify preheating treatment[17,18]. Although, the trials provided an opportunity to optimise preheating of the SENs in terms alignment issues it was not able completely resolve the fast-cooling rate noticed in some parts of the SEN between off-gas time (time taken away from flare) and installation of SEN into the position of casting[17,18].

However, a similar investigation was conducted by sponsor company's sister site in the following year in trying to understand the thermal stresses during heating up, cooling (during off gas time), and when the SEN is in casting position (when the SEN becomes in

contact with molten steel)[52]. It was a conclusive in their investigation that the installation aspect of the SEN was found to be by far the most important factor than thermal stress caused by non-uniformity during heating[52]. They also made a recommendation to focus on reducing off-gas time prior to the SEN coming to contact with molten steel[52].

The persistence of the failure incident and cost involved in the investigation process prompted sponsor company site to find better ways for determining performance issues. It was noted in the presentation given by the supplier to sponsor company that the influence of preheating on the mix (raw material inside the SEN) was something that was not investigated[17,18]. This indicated an opportunity for standardising performance and being able to distinguish failures arising due to their process or supplier material's integrity in a much simpler and smarter way which drives the body of this work.

The preheat research was later confirmed and assigned as a doctoral study coinciding with the second half of the doctoral research programme (2019). It replaced the initial research of secondary steel making and clogging phenomena (where there is already a significant body of prior work). This revised approach was determined to have greater industrial impact in terms of knowledge and may lead to possible analytical procedures that save cost in the long run. There is real value in knowing the possibility of increasing the preheating time. Knowing the limits of preheating can help reduce refractory consumption and save additional cost in terms of reducing the number of unused pre-heated SEN that have expired their preheating time. The study may also circumvent the cost involved in failure analysis of major incidents that involves trial and major material testing regime that often relies on the virgin mix (raw material) instead of directly assessing the product due to geometrical and sample challenges.

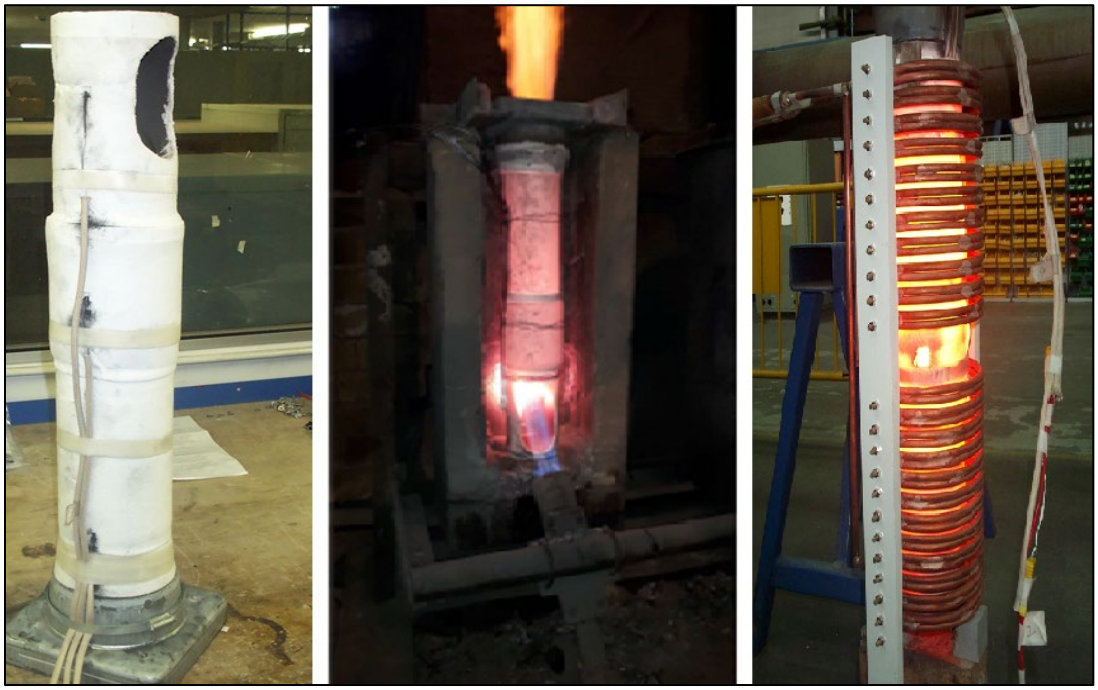

Figure 2. Thermocouple trial (two images on the left) conducted on sponsor site. The SEN (middle image) is being gas flared or preheated outside in an open oxidising atmosphere with thermo-couples installed at various points along its length. The protective glaze coating protects the SEN from oxidation during preheating. The image on the far right is the inductive heating intervention undertaken on behalf of sponsor company to mitigate non-uniformity of heating.

In the interim, the thermo-couple trials conducted at sponsor site initiated a series of heating propositions alongside burner re-positioning and preheating chamber re-construction[17,18]. There has been trials and discussion surrounding the use of inductive heating strategies (see Figure 2) to eliminate the uneven heating of the SEN. Induction heating has been adopted in other major steel making industry to achieve even heating and faster heating rates that suppresses oxidation by early activation of the glass protective coating around the SEN[53]. Although, these heating strategies may improve performance by meeting the preheat target temperatures, their influence on the SEN must still be investigated. The question about the material's integrity and ways to detect performance issues using the material itself to inform about process influences remained unaddressed. This will therefore be the main driver for this research.

2.2 Submerged Entry Nozzle

2.2.1 Background and Structure

2.2.1.1 Continuous casting process

The continuous casting process of producing steel was invented to mitigate wastage of steel production and increase productivity[3,54–56]. The continuous casting process facilitates the cooling down of steel into intermediate products as either slabs or billets

which are later transformed to thinner products called sheets, at other steel processing sections of an integrated steel plant (i.e., cold rolling and hot rolling processes)[3,54,56,57].

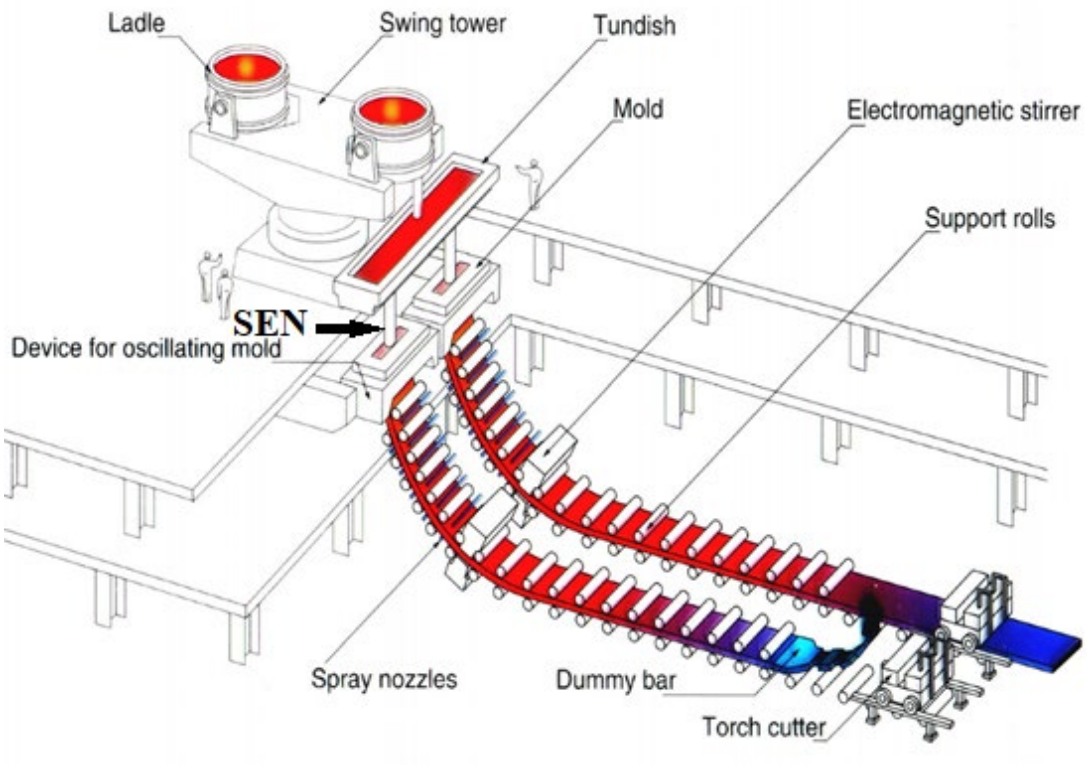

Figure 3. The continuous casting process of a steel plant showing the various section of the casting operation. The pre-heated SEN is positioned between the tundish vessel and the mold after its installation or in casting position. Molten steel arrives in ladles and are emptied into tundish before finally cooling with the help of mold and spray nozzles (image adapted to show position of SEN)[54].

During casting, molten steel arrives at the continuous casters of a steel plant inside vessel containments called ladles (see Figure 3)[54,58]. Once the ladle arrives, it is positioned right above another vessel called the tundish[3,54]. This is where the ladle's steel content is gradually released[54,58]. Ladles also have a tube-like shroud similar to SEN that facilitates the transfer of molten steel into the tundish [3,54,58]. The tundish act as a buffer container that facilitates the means to control the speed of casting and can be used for further steel treatments including inclusion removal for better quality steel[3,54].

The preheated SEN is positioned between the tundish and the mould (see Figure 3 and Figure 1) [3,54,58,59]. As well as acting as a flow control device, it is equally responsible for shrouding the liquid steel from atmospheric contact with air[3,54,58]. The SEN therefore prevents re-oxidation of steel during casting and helps improve steel quality [3,7,54,58]. Despite the benefits the SEN holds during casting, it suffers from major drawbacks due to the effects of improper preheating (i.e., thermal shock and loss of

strength due to oxidation) as well as clogging and mold flux erosion[1,2,7,17,60,61]. Most steel plants use SENs with an exchange mechanism by design, in-order to maintain the continuous process of casting[17,18,59]. The exchange mechanism gives steel manufacturers the ability to regularly change the SENs during casting whiles maintaining the continuous production stream [17,18,59]. The SEN utilised on sponsor company site is gas flared during the preheating stage in an open atmosphere, but a protective glass coating is what protects it from the oxidising atmosphere[14,17,18].

2.2.1.2 Manufacturing process of SEN

The route of manufacturing for carbon-bonded refractories generally involves the below steps chronologically, with the last two dedicated to manufacturing of the SEN itself (also see Figure 4 for the SEN route)[10,12,18,62,63]:

1. A mixing stage of raw material blends
2. A moulding stage to give its required shape and in the case of the SEN, this will take the route of isostatic pressing
3. A baking or carbonising stage conducted in an inert atmosphere
4. An impregnation stages to reduce porosity
5. A glazing stage in the case of the SEN for oxidation protection
6. An insulation blanket or coating wrapping around the SEN for preventing heat-loss during preheating service

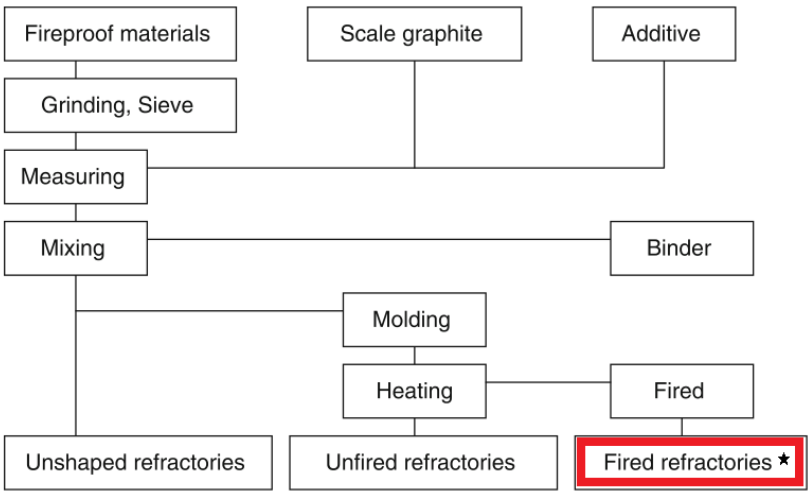

Figure 4. Depiction of the general manufacturing process of refractories, highlighting the route the SEN would take under "Fired refractories" (shaped refractories) according to Louis Pilato (image adapted with star symbol and thick and red inner border under Fired refractories to show the route of the SEN)[62].

Prior to blending, the aggregates, binders, and fillers would have been ground, milled (granulated), sieved, and distributed to the required particle sizes[10,12,62]. Blending or mixing temperatures can range between 160 °C – 200 °C depending on the binder of choice and its curing properties which then forms a so-called green batch[10,12,62]. The isostatic forming of the product ensures that there is less defect (mainly porosity), making the final product more isotropic overall[10,12,62]. Carbonisation at higher temperatures (to approximately 1200 °C in some cases) creates pores within the material itself that requires further impregnation to improve the density of the final product[10,12,62]. Impregnation agents such as resin and coke can be used for this purpose [10,12,62].

The coking temperature of carbon bonded refractories have an impact on their strength and elastic Young's modulus[47,48,64]. The dynamic elastic Young's modulus is known to decrease in the initial stages of heating up to 500 °C due to the effects of volatile release from resins[47]. Beyond this temperature the thermal expansion mismatch between aggregate and carbonaceous matrix causes an increase in the elastic Young's modulus[47]. There is a holding time of heating and then cooling down which create microcracks which in effect lowers the strength of the material [47,48,64]. Zielke et al has shown the effect of coking on the strength of a carbon bonded refractory whereby the higher the coke temperature the lower the strength (< 1200 °C) (see Figure 5) [65]. Strength is also observed to decreased when the material is heated beyond its coked temperature (shown by material coked at 800 °C in Figure 5)[65]. The pore opening and closure mechanism described by various authors (Luchini et al, Werner et al etc.) affecting the aforementioned properties in carbon bonded refractories will be expected to influence the behaviour of SEN during preheating[47,48,64].

Phenolic resin binders in the form of resol or novalak resins are predominantly adopted in manufacturing practises as the main bonding material for carbon bonded refractories[10,12,62]. Their adoption in industry is due to phenolic resins being more environmentally friendly in comparison to tar, coal-tar, and pitch[10,12,62]. These resins originate from a series of condensation reactions between phenol and formaldehyde precursors and crosslinked upon curing [10,12,62].

Their pyrolysis stage combines a complex series of many mechanisms occurring simultaneously: i.e., condensation, oxidation, decomposition, slight shrinkage, dehydration [10,12,62,63]. During pyrolysis a careful balance of the release of volatiles and condensation must be managed to obtain good carbon yield by peroxidation or chlorination to increase the cross-linking density of the resin[63]. Their curing stage has to also be

carefully monitored, to allow a good mixing time prior to hardening[63,66]. The time it takes to harden can be adjusted by the presence of a catalyst and changes in PH[10,63].

The phenolic resins are classed as non-graphitising carbons however, they exhibit significant changes in structure during heating and are able to be catalytically graphitised during their processing and/or when used at steel making temperatures. Otherwise, graphitisation can occur only at temperatures above 2000 °C[63,66].

Phenolic resins have greater strength in contrast with their pitch bonded counterparts[10,12,63,66]. They also succeed in producing higher carbon yields during carbonisation, and are readily available in many forms (i.e., power, solution, solids) [10,12,63,66].

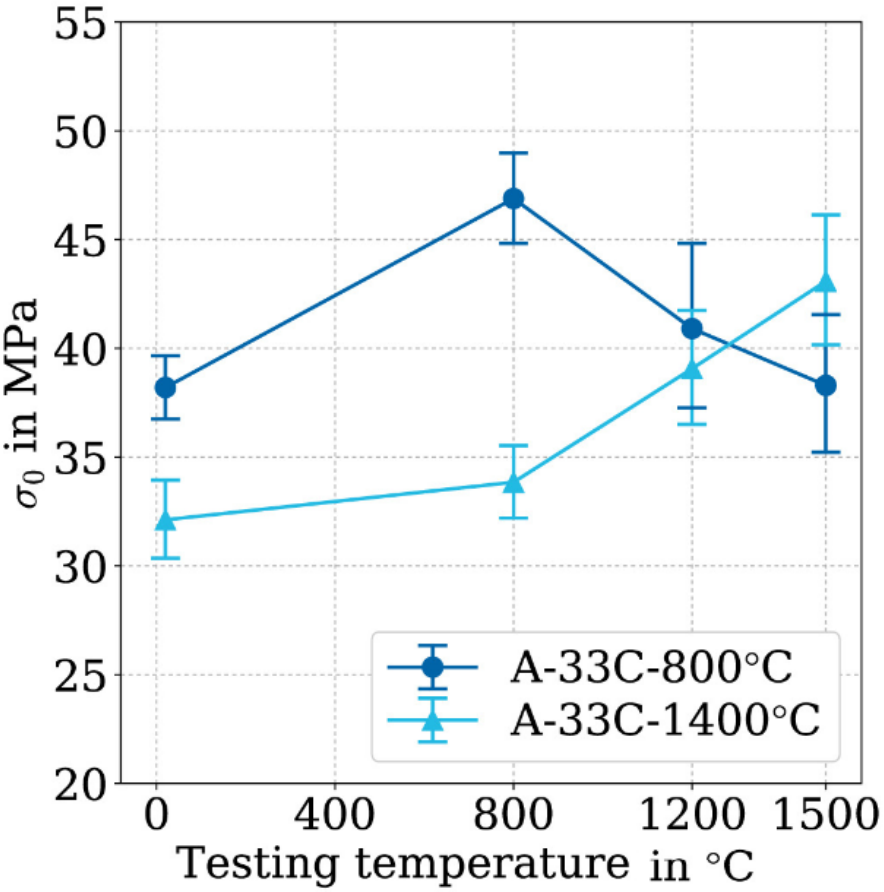

Figure 5 The influence on coking temperature on the biaxial flexural strength of carbon bonded refractories with the same carbon content of 33%. The higher coked sample shows lower strength at temperatures below 1200 °C due to thermal expansion mismatch theory of Luchini (i.e., it has higher pores or micro crack formation when cooling). Strength is observed to increase up to the coked temperature before decreasing as a result of newly generated cracks[64].

Phenolic resins do, however, possess a lower thermal conductivity, a higher elastic Young's modulus and are less thermal shock resistant [63,66,67]. However, their thermal shock

inferiority may not be detectable when inside a refractory composite[67]. This is due to the complexity of the composite whose thermal shock resistance depends on its microstructure and the way in which crack propagates through it[67]. Its oxidation resistance is also inferior due to having a higher surface area in comparison to pitch[67]. The addition of more resin carbon than graphite increases porosity[12]. In general, having more carbon content increase apparent bulk porosity and decreases density decreased[12]. The presence of pores and surface area attributable to these carbons therefore poses a risk to oxidation in the context of SEN preheating[10,39].

The formation of glassy carbon after carbonisation makes them very susceptible to spalling[10]. As a binder they can form dense products without many open pores which negatively impacts the structure if gaseous evolution occurs during its decomposition through heating[63,66]. Hexahydric alcohol has been used to try circumventing some of the disadvantages associated with the use of phenolic resin (spalling)[10]. The addition of graphite to the resin also reduces the spalling effect[12]. This factor is also important as preheating of the SEN can cause pyrolytic degradation of the resin[24].

Additives in the form of antioxidants, resin graphitizers, are commonly used to improve the product behaviour depending on its purpose [10,12,68]. They can also be used to improve the strength of the refractory[12]. Additives can come in the form of metals or metallic alloys (of Carbides, Nitrides and Boron types)[10,68,69]. Lastly, aggregates will also have to be pre-synthesised or sourced with great purity prior to incorporating into the manufacturing process[10,68,69].

The raw material choices and their processing parameters would eventually determine both the cost, quality, and performance of product produced[12]. It is documented that the most notable parameters for raw materials inspection are its particle size distribution, presence of impurities, ash content and degree of graphitisation in the case of binders[12,63]. Quality control inspection with the aid of sophisticated software is always in-place to ensure manufacturing processes are consistent[18]. It is the believe that a consistent process produces consistent products[18]. Products would inevitably have slight variations which will have to be accounted for as acceptable tolerances documented in service-agreement with respective customers[18].

2.2.1.3 Structural Components of the SEN and their implications

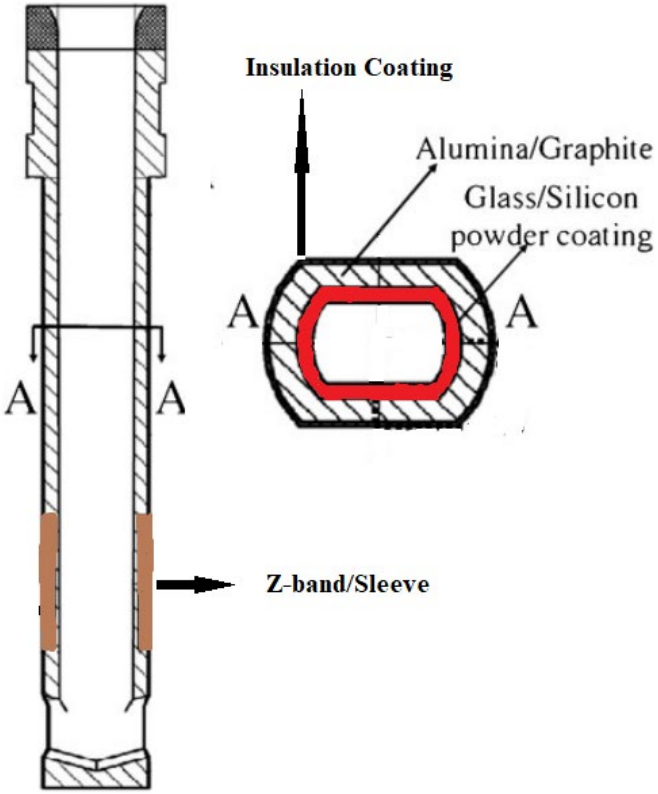

Figure 6. Cross sectional image of the SEN adapted from Memarpor et al., showing the z-band, protective glass coating, alumina-graphite main bulk material and insulation coating locations[15].

The diagrammatic illustration of the SEN structures above (Figure 6) will serve as a visual reference in the subsections to follow.

2.2.1.3.1 Carbonaceous Matrix (Graphite)

The integration of carbon in the SEN allows it to be heated rapidly in order to reach the optimal temperature required for protection against oxidation. The increase in carbon content (Graphite) is associated with an increase in thermal conductivity, lowering of elastic Young's modulus and thermal expansion [10,12,67] (see Figure 7). These properties have the overall bulk impact of improving the thermal shock resistance of the refractory [10,12,67]. Its non-wettability by slag attack enhances its corrosion resistance[10,12,67]. Graphite also provides a means of increasing toughness as it hinders crack propagation due to its thermal expansion mismatch with the aggregates creating compressive strains and micro-crack deflections[70]. It develops higher strength for the refractory when heated[10,67,69]. Cooper et al., demonstrated that graphite flakes in carbon-based refractory system increase the strength of refractories(see Figure 7)[69]. This mechanism of toughening described (as graphite pull out and crack branching) was based on a clay-

graphite refractory, however, it was suggested that this effect of graphite flake can be expected in other carbon-based ceramic composites[69].

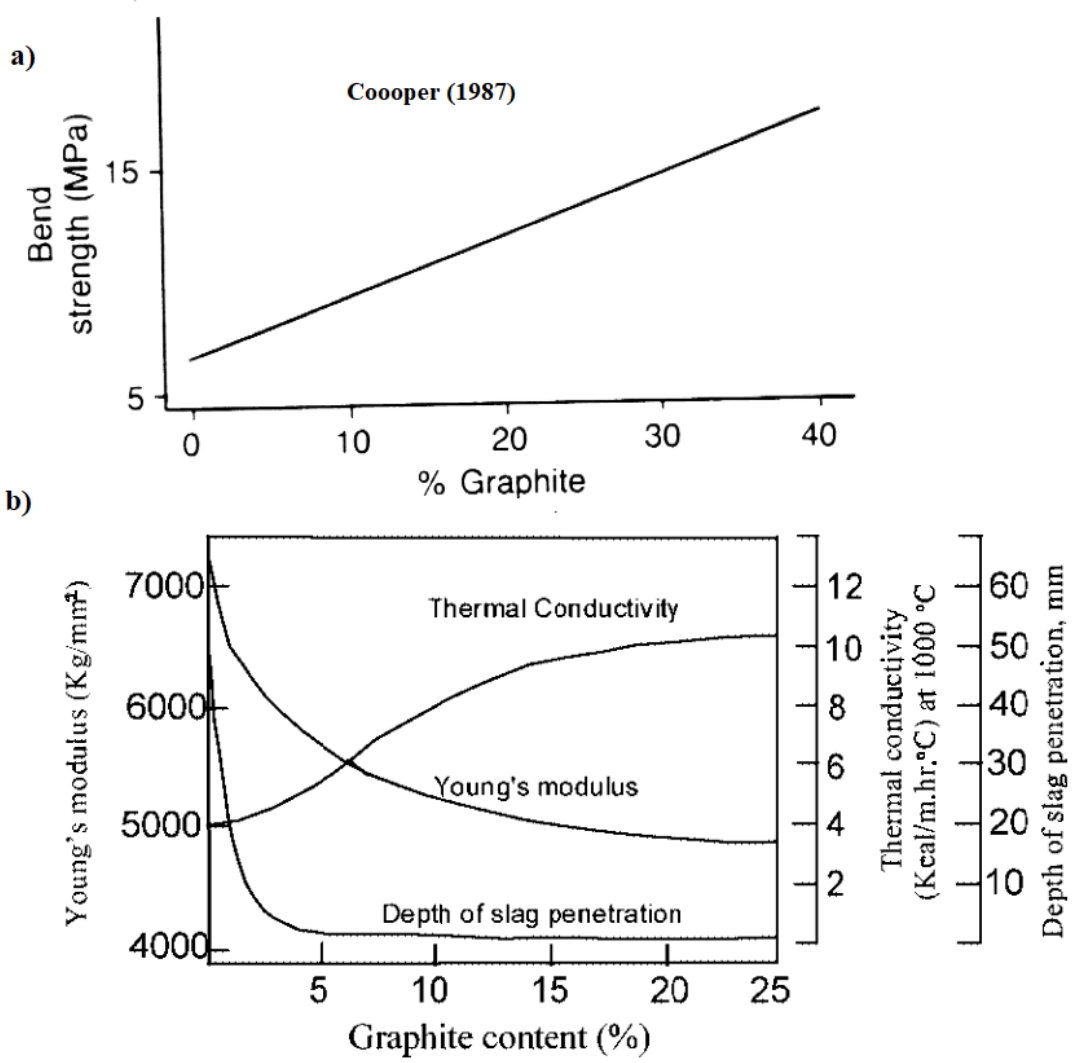

Figure 7. The effect of graphite on the carbon-based refractories systems. a) The effect of increased graphite flake shows an increased in bending strength adapted from cooper 1987, b) The increase in graphite content on the properties of magnesia carbon bonded refractory system showing an increase in thermal conductivity and a decreasing trend for both Young's modulus and depth of slag penetration.

The properties of a graphite as a HCP (hexagonal closed packed) single crystal are well known to be anisotropic[10,67]. It has a planar structure with the weaker bonds situated between the planes and the strong covalent bonds joining the carbon atoms sitting on the plane [10]. Its thermal conductivity is far greater in the direction parallel to the plane than perpendicular to it (i.e., 200 times more)[10]. Its thermal expansion property is greater in the direction perpendicular to its plane the by the same magnitude (200 times)[10]. Even its compressive strength is far greater in the direction perpendicular to its planes than parallel to it[10]. However, it is important to distinguish these properties from that of the commonly manufactured carbon bonded refractories where there is a random array of

graphite crystallites (amorphous carbon and well-ordered carbon) that exist within a random structure[10]. The degree of graphitic anisotropic decreases with such random structures to an extend where it may no longer be feasible to determine properties of the bulk from graphitic orientation alone[10].

A study conducted by Rand, B. et al., did however, evidence the anisotropic influence of orientation on graphite's thermal expansion coefficient when a prepared model graphite composite devoid of additives (antioxidants) was uniaxially pressed and heated at 1600 °C[67]. The study showed the tendency of graphite flakes aligning perpendicular to the pressing direction[67]. Since the in-plane thermal expansion coefficient is almost zero at this preferential orientation after pressing, the thermal expansion coefficient declined as function of increased graphite content[67]. This was in contrast to graphite aligned parallel which remained a constant value[67]. The results obtained were based primarily on experimental conditions aimed at modulating particle sizes of oxide and graphite to obtain a preferred orientation and not to be confused with industrially manufactured carbon-bonded refractories in terms of processing and the microstructure produced as a result[67].

The disadvantage of carbon sources within refractories is their susceptibility to oxidation at temperatures above 400 °C if not protected and exposed to oxidising environments[1,2,10,24]. The increase in carbon also creates a risk of carbon pick up in molten steel which is undesirable[12,71]. The high thermal conductivity may pose a risk to faster cooling of the SEN when being transported for installation[12]. It can cause a rapid undesirable decrease in the temperature of the molten metal leading to its solidification on the refractory [12].

There is also a major gap in terms of the practical application of thermal shock assessments with regards to composite refractories[23]. There are inconsistencies between theoretical values of the critical temperature difference to induce shock (ΔT_c) versus those measured in quench test experiments[23]. Many parameters of the quench environment are unknown, and its heat transfer properties can be affected by factors such as temperature and specimen surface[23]. This means that the values produced from such experiments will have major issue if used to give accurate design criteria for practical use. Determining thermal shock behaviour during a transient thermal condition analytically yet remains a challenge[23]. Although, extensive research has been utilised to establish the knowledge of thermal shock with regards to ceramic monolithics, for their composite counterparts the knowledge cannot be directly transferred[23]. Refractory composites bring about more complexity such as anisotropic features and mismatching of properties, the presence of different phases

and interfacial features between matrix and its surroundings[23]. These would influence the fracture behaviour often described using Hassleman's unified theory of thermal shock[23]. In other words, no unified theory can suffice all composite which means efforts have to be continuously geared toward both experiments and theoretical studies to improve knowledge and seek better ways of predicting performance[23].

2.2.1.3.2 Protective Coating

The primary protection of the SEN against oxidation is provided by a glass/silicon outer coating (SiO_2, Na_2O K_2O) that forms an alkaline glaze during the process of preheating (see Figure 6)[2,72]. It is the activation of this glass-oxide coating at temperatures above 800 °C that necessitates a rapid heating regime for ultimate protection[1,2,72]. Under heating therefore poses a great risk to oxidation as well as thermal shock failure when the SEN is suddenly in contact with liquid steel[2].

The integrity of the glazed coating of industrial SEN investigated by Memarpour et al., highlighted how alkaline phases (Na_2O, K_2O) within the glaze can react with the graphite refractory base material to form CO gas[15]. The dissociation of which can be a source of carbon and oxygen pick up for the steel[15]. The presence of silicon found on the coating after preheating also presented a risk when it co-existed with carbon within the SEN interface[15]. According to Memarpour et al., this resulted in an increased activity of silicon which can lead to the formation of undesirable silicates that attract inclusion from steel and lead to clogging[15,73].

The decrease of silica in the glaze after preheating can also be used as to indicate that it has reacted with the refractory base material [15,73]. A no glaze penetration of the base refractory material indicates good protection against oxidation and confirms that the heating rate of the SEN was effective enough to activate the glaze protection required[15,73].

Madias et al., also investigated a glazed SEN composition and arrived at similar conclusions of glass formers within the glaze composition being able to react with the refractory base material[2]. In their study the existence of porosity within the glaze was an additional assessment indicating poor preheating and a risk of oxidation[2]. Chromium found in some SEN glaze compositions was known to be protective and prevented porosity formation by forming an (Cr_2O_3) oxide during preheating[2]. However, the preheating gaseous atmosphere (i.e., CO and CO_2 partial pressure) and temperature are both important factors to consider thermodynamically when heating the SEN with respect to Cr_2O_3 being able to protect the SEN[2]. Madias et al., showed through an Ellingham diagrammatic

illustration that at 1260 °C chromium oxide was stable in a rich CO atmosphere, but if the partial pressure of CO were to be less than 1 atm (atmospheric unit of pressure) the protection of the glaze would be lost due to a reduction of the chromium oxide [2]. At preheating temperatures of a 1000 °C, the chromium will be reduced if partial pressure of CO was to be less than 1.3 x 10^{-2} (atm) [2].

Kumar et al., also investigated preheating mainly focused on the zirconia band of the SEN but briefly touched on the alumina-graphite phase[14]. Their study also highlighted there is a presence of metallic silicon in the base material post preheating of the alumina-graphite part of the SEN[14]. There were also additional features related to observed grain geometrical differences of silicon particles before preheating and after the preheating process[14]. Their assessment of the zirconia band highlighted the preheating degradation mechanism of zirconia that occurred through the formation of zircon in the glaze and its dissolution during casting[14]. Finally, they highlighted the persistence of the coating protection during casting for at least 90 minutes with regards to the zirconia band[14].

Novel coatings in the form yttra stabilized zirconia and calcium titanate have been shown to improve SEN protection against oxidation and reduce the impact of clogging[72,73]. An additional improvement that has been tested to circumvent the increase of silicon activity at the SEN interface caused by carbon, was to engineer a specialised composite nozzle comprising of two parts[74]. The composite nozzle had an inner bore which was made with a carbon-free refractory material and then co-pressed with an outer bore of an alumina carbon-based refractory[74].

2.2.1.3.3 Z- band/Sleeve

The Z-band/sleeve is made of zirconia graphite-based refractory[14]. The is a component found just above the port of the SEN and it serves to protect the SEN against mold flux erosion during casting (see Figure 6)[14,60]. Zirconia is an advanced refractory usually incorporated to give additional benefits where other refractories may not do so well[75–77]. It maintains a good thermal shock resistance while having better strength, fracture toughness and erosion resistance properties [75–77]. It is regarded to be more corrosion resistance than alumina, hence it is used to counteract mold flux corrosion [75–77]. It is often stabilised/or partially stabilised by calcium oxide, magnesium oxide, or yttria doping for better thermal shock resistance [73,75–77].

Kumar et al., investigated the impact of preheating on the glaze coated Z-band and the impact of glaze coating after preheating i.e., during casting for the first 90 minutes and 480 minutes[14]. Their study proved that the preheating temperature was critical in the

degradation mechanism involved with regards to the Z-band prior to casting. It was uncovered that during preheating destabilisation of the zirconia aggregate occurred leading to the formation of pits and fissures[14]. A further interaction between the high silica content in the glaze infiltrating into the fissures led to the formation of zircon. The presence of zircon at preheating temperatures caused the fragmentation of zirconia aggregates and drifts to the top layer of the glaze at the initial stage[14]. During casting, a rapid dissolution rate of the zircon was observed when in contact with the mold flux [14]. After 480 minutes of casting the glaze was lost and dissolution rate observed with regards to destabilised zirconia was noted as constant [14]. It was also emphasized that the destabilised region was only limited to the outer reaction surface of the zirconia grains[14]. It was conclusive that preheating temperature was critical in impacting the glaze thickness and should be adapted based on plant practises[14].

Although not easily adopted due to expense or at times requiring more field testing for supplementary validation checks, there have been many developments related to the use of zirconia in other parts of the SEN [75]. Zircon-zirconia and alumina-zirconia systems based on a toughening dispersion mechanism of monoclinic zirconia crystals holds a potential for application in SENs to resist clogging and reduce temperature of preheat[75]. An additional development by Vesuvius Crucible Co. and Cookson Group PLC working collaboratively have produced a so called O'Zirconia refractory based on reacting zirconia with silicon nitride[75]. Field trials have shown the potential of O'Zirconia-graphite refractory protecting against alumina building up in the SEN, outperforming refractories made with sialon-graphite[75].

It is also important to note that the Z-band has been a major focus in many studies mainly related to its degradation with mold flux slag[5,16,76,78,79]. There is still ongoing research highlighting the complexities involved in the phenomenon of slag crawling[5,16,76,78,79]. Some of which aim to supplement early theories in terms of degradation mechanisms with regards to mold flux erosion and industrial/plant operations, this is in contrast with preheating studies which are quite limited[14,60].

2.2.1.3.4 Main Aggregate - Alumina

Various high melting point oxide aggregates are selected to make up part of the SEN's base material. Alumina is the major compositional constituent for the SEN, although other oxides such as silica, zirconia, lime, titania, and magnesia are additions that are commonly incorporated into the mix, in order to obtain the best properties[53,80,81]. In the 1960's fused silica was used as the main material of choice for the nozzles, which was later

changed to alumina to counteract the effect of Mn (manganese) in steel and provide better erosion resistance[53,80,81].

The preferred method used for synthesis of tabular alumina grains(40 to 200 μm) is by heating pellets of calcined alumina at temperatures just below its melting point [69]. This converts it to approximately 100% alpha alumina[69]. They possess high crushing strength (30 – 60 MPa) and good thermal conductivity (40 W m^{-1} K^{-1}) making them a useful application for counteracting thermal shock as a component of the SEN[69].

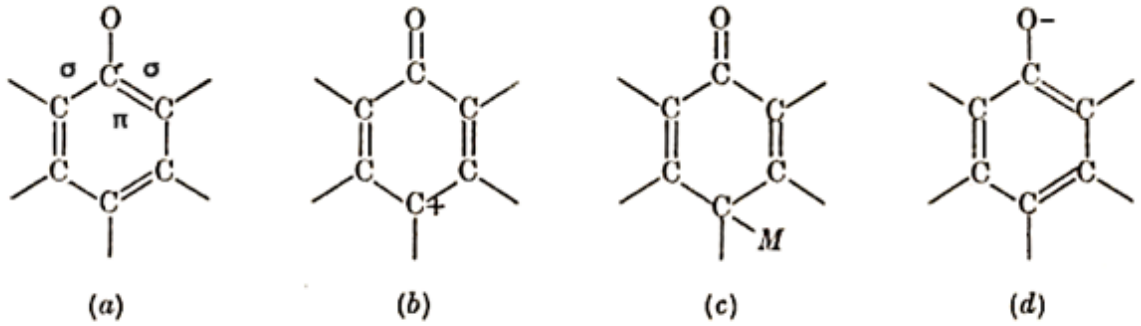

Figure 8. The electron interaction of catalyst with carbon proposed by Long and Skyes. a) Represent the electron configuration adopted when an oxygen atom is initially absorbed, b) and c) are the configurations adopted for easy evolution of carbon monoxide by transfer of electron to catalyst or forming a covalent bond with it, respectively, and d) represent the configuration that inhibits the evolution of carbon monoxide by accepting electrons from a donor which stabilises its structure [81,82].

Yamaguchi A et al., investigated the effect certain refractory oxides may have on the oxidation of graphite using electron theory (i.e., the electron interaction of catalyst with carbon proposed by Long and Skyes) [81,82]. Refractory oxides are mostly stable at preheating temperatures and therefore cannot oxidise graphite, hence the use of electron theory is the only way in which their effects could be explained[81,82]. According to this theory, a carbon atom that has oxygen adsorbed onto it takes the initial configuration of Figure 8 (a) [81,82]. The oxygen in this state is firmly attached to the lattice electron configuration and requires the breaking of the two sigma and one pi bond to release carbon monoxide as a product of the reaction[81,82]. Based on the electron theory, if graphite was to exist with a catalyst the bonds required to be broken will be different[81,82]. They will either take the configuration of Figure 8 (b) or Figure 8 (c) in order to release the carbon mono oxide[81,82]. If the graphite transfers an electron to the catalyst, then configuration Figure 8 (b) will be adopted[81,82]. If the catalyst forms a covalent bond with graphite, then configuration Figure 8 (c) will be adopted[81,82]. Due to the loss of one pi bond, the configuration of Figure 8 (b) and (c) are much weaker (in comparison to Figure 8 (a)) and

can therefore facilitate the evolution of carbon monoxide[81,82]. The last configuration of Figure 8 (d) is adopted when the catalyst transfers electrons to graphite completely and as a result stabilises the oxygen atom in that configuration[81,82]. This makes it difficult for the evolution of carbon mono oxide to occur and acts more like an inhibitor in this instance[81,82].

Yamaguchi et al., experiments indicated that the presence of alumina oxide accelerates graphite oxidation though an electron accepting mechanism. This changes the conformation of the graphite bonding structure or electron distribution facilitating its ease to be oxidise in the presence of an oxidising agent[81]. However, titania, zirconia and magnesia were regarded as electron donors and therefore reduce the effect of oxidation by donating electrons to graphite stabilising its structure or electron distribution[81]. Silica was noted to reduce the effect of oxidation by a very small amount and its electron-donating or accepting properties are not known[81]. All experiments were performed at low temperatures relevant to the preheating temperatures discussed herein[81].

2.2.1.3.5 Insulation coating

A highly porous insulation layer of fibrous refractory material (can be made from: silica glass, pure alumina, and alumina-silicate) is the final component wrapped around the SEN's outermost region (see Figure 6)[52,53,69]. This component serves to protect the SEN from losing heat during off-gas time which is the period between the SEN being taken away from the burner and in contact with molten steel during casting[17–19]. It melts away when in contact with the melt/molten steel[17–19]. Its thickness can range from 3 – 6 mm[52,53,83].

The off-gas time was a useful parameter investigated during the preheat failure incident at sponsor site[17]. The off-gas time was divided it up into three parts during the investigation[17]. The time taken to change a tube (i.e., equating to anytime up to 2.5 minutes of cooling time), the flying tundish change time (i.e., up to 4.5 minutes of cooling time), and the start-up of casting (i.e., > 4.5 minutes)[17]. It was demonstrated during the trial that adjustments of the burners to get a better heat distribution improved the time it took for parts of the SEN to cool down[17]. The ports and the base of SEN were only able to maintain their temperatures above 800 °C during the tube change time post adjustments[17]. However, the zirconia-band and 500mm from the SEN's plate were able to main temperatures above 800 °C for all time sections of the off-gas time[17].

2.2.2 Pre-heating temperature and time

Preheating time can vary quite significantly from anywhere between 1 to 6 hours at sponsor company[17]. The SEN can also experience variation in wall temperature during its preheating cycle[1,17]. This non-uniformity of temperature distribution can be attributed to the positioning of the burners relative to the SEN's walls during its heating cycle and can take around 30 minutes to reach its optimal temperature of preheat[1,17]. There is a higher risk to thermal shock at short heating times and a risk to oxidation and longer heating periods[1]. The SEN's is heated to temperatures 1000 °C to 1200 °C and it should be kept above 800 °C post preheating as best practise[1,2,17]. A faster heating regime would ensure that critical temperatures (550 °C – 950 °C) where oxidation is likely to occur are passed quickly[1]. Faster heating rate also ensures that the glaze is activated in time to prevent any oxidation from occurring[1,17].

Svensson et al., found in their industrial preheat trials, variation of temperatures across the length of the SEN and all steel plants they investigated. Those with faster heating rates were essentially protected by against oxidation by reaching the optimum preheat temperature required to activate glaze coating[1].

Another critical process time not covered in this context is the casting time or heat (usually representing the same steel quality with successive ladle per heat) experienced by the SEN when in contact with the molten metal[84,85]. A SEN can be used and maintained for approximately 4 heats before changed [84,85]. The SEN must be maintainable for a long duration when both preheat time and casting time is considered.

2.2.3 Fundamentals of Raman and Model-Free Kinetics

2.2.6.1 Raman Fundamentals, Limitations, and Carbonaceous Matrix Assessment

It is known that diffraction-based methods (neutron, electron, X-ray) are insufficient in their characterisation of structures pertaining to disordered forms of carbon and a more suited for crystalline carbon forms[45]. Raman spectroscopy on the other hand has shown proven capability to characterise carbons (solid) with high sensitivity ranging from short, medium to long range order[45]. It is effective in resolving disordered forms of carbon[45]. Due to this reason, it has become the standard tool for characterisation especially for samples where different forms of carbons co-exist[45].

It fundamentally uses the vibrational dynamics of molecules to uncover their structure and relate it to the ordering of carbon forms[45,86,87]. It is a form of spectroscopy that uses the process of inelastic light scatter effect, when a laser source interacts with a material/or

molecules (i.e., be it solid, liquid or gas) to cause its excitation of vibrational mode[45,86–88].

The Raman scattering process can be summarised as two main parts (see Figure 9):

1) An incident light is absorbed by a polarizable sample causing the molecules at the ground vibrational state to transition into an excited state/or virtual state.

2) This is subsequently followed by a transition from the excited state to a lower energy state emitting a photon of energy (loss) in the process and creating or absorbing a vibrational quantum of energy (phonon) dictated by two processes (stokes and anti-stokes)[45,86,89].

The stokes process being the loss of energy due to the difference between the ground state and excited state [45,86,89]. Stokes processes are mainly used in Raman studies due to having higher intensities than the anti-stokes process [45,86].

The anti-stoke process is where a molecule already exists in an excited state then absorbs light (photon) energy to transition into a virtual state and then returns to the ground state. The energy gained from the incident photon due to difference between ground state and excited is known as anti-stokes [45,86,89].

Rayleigh scattering which is normally filtered out via Raman instrumentation is a form of elastic scattering where there is no difference in energy between the incident photon and scattered photon(see Figure 9) [45,86,89].

A Raman shift in energy is equivalent to its scattered photon/ or vibrational states of the molecule under investigation[88] This can be represented graphically as a spectra of scattered light (on the y-axis) vs frequency of light (on the x-axis: with its unit referred to as wavenumber cm^{-1}) as depicted in Figure 10. Other units such can be adopted on both the x-axis and y-axis and depending on the Raman instrument used, however the meanings in Figure 10 still apply.

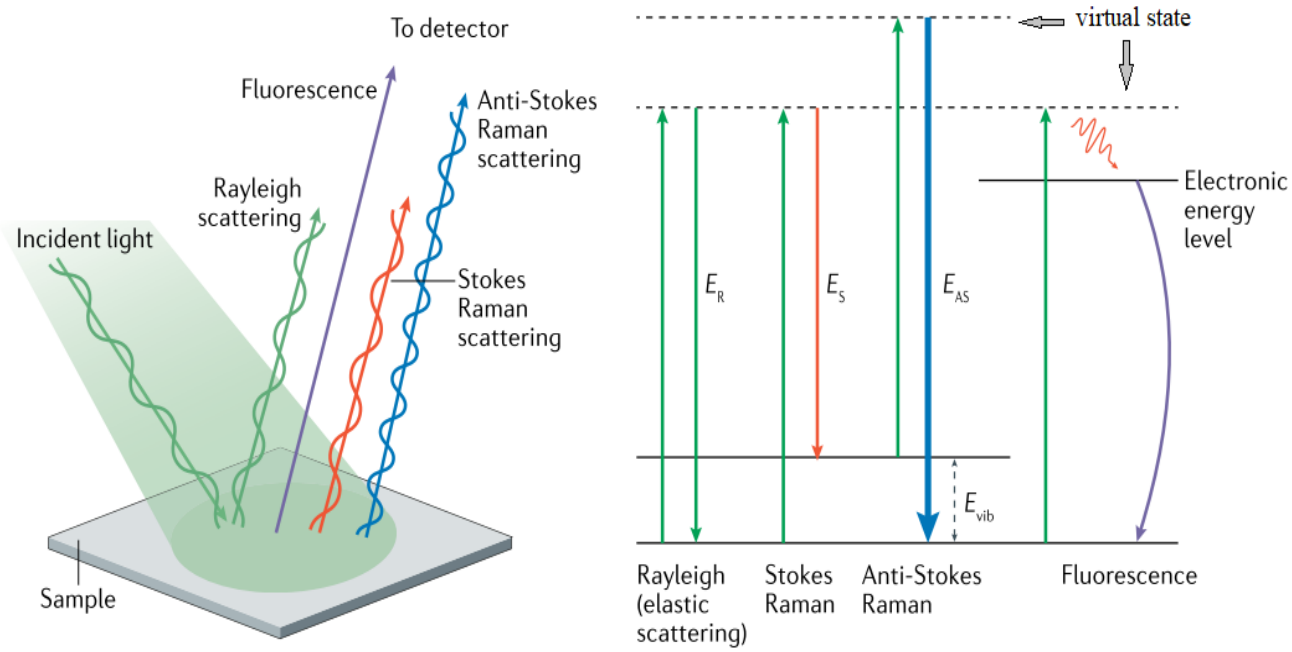

Figure 9. Adapted illustration of the different modes of light scattering phenomenon in a Raman instrumentation when an incident photon reacts with a polarisable sample. The arrow demonstrates the direction of excitation and de-excitation of molecules to various vibrational states involved in each type of scattering (Rayleigh, Stokes, Anti-Stokes, Fluorescence; E, referring to their associated energies)[89].

A typical Raman graphical spectrum would show [88]:

i) Intensity – which is indicative of the measured component concentration within the sample

ii) A Raman shift position/peak – used for identification of samples structure, phase, and stoichiometric content, and

iii) Peak width – useful for calculating crystallinity (FWHM: Full Width Half Maximum), to detect the influence of defects/or doping and its shift in position relative to where it originates can be used to understand the effects of temperature, pressure, and stress.

The graph below represents the aforementioned points (Figure 10):

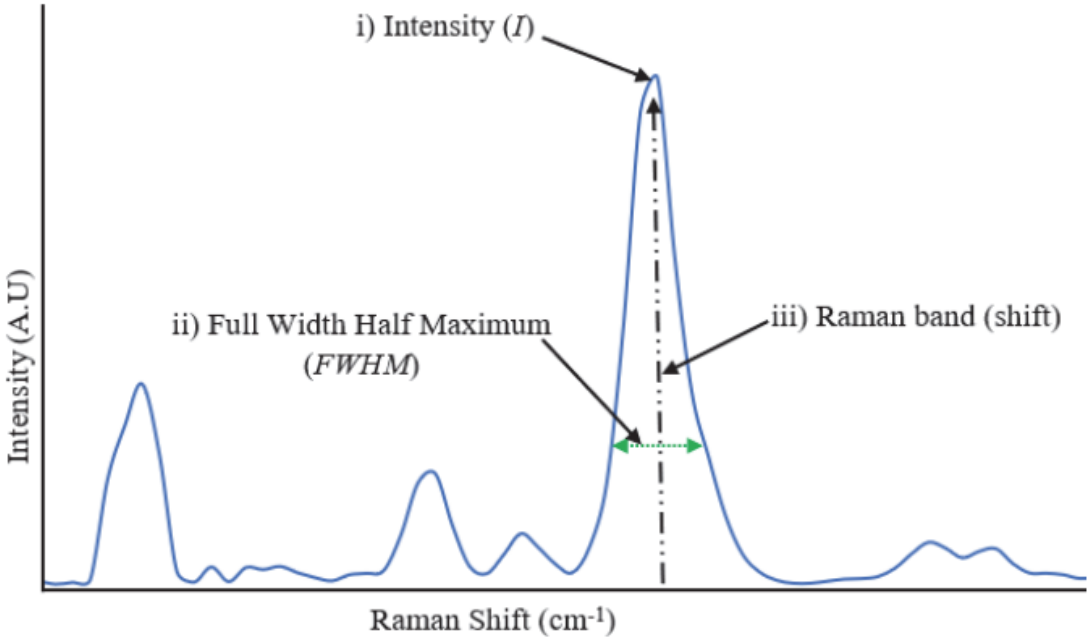

Figure 10. An example a Raman spectrum highlighting the important aspects to consider when assessing a spectrum. The peaks intensity (useful for detecting concentration), width (useful for detecting defects or doping) and position (useful for identification of molecules) are three key main features that can used to understand Raman components[88]

The most common limitations pertaining to Raman spectroscopy comes in form of a fluorescence effect obscuring the Raman signal, and high excitation effect/laser power which can thermally decompose samples sensitive to heat[86,88,89]. When an incident photon's energy is equivalent to an electronic energy level of a molecule, excitation to this energy level followed by a de-excitation that emits a photon with a longer wavelength than the incident photon is what causes fluorescence to occur (refer to Figure 9)[89]. Alumina is known to cause fluorescence; however, graphene can suppress this effect. With the advent of more sophisticated Raman tooling fluorescence can be mitigated via time-gated techniques to quickly obtain Raman signals prior to the effect of fluorescence[49,86,88].

The diversity of carbon presented in its bonding types to forming two-fold, three-fold and four-fold hybridized bonding allows for their classification into crystalline and disordered forms[45,87]. The common crystalline carbon phases are graphite, diamond and fullerite. The disorder members have many forms some of which are: glassy carbon, graphitic amorphous (g-C), nanocrystalline carbon, diamond-like amorphous carbon (d-C) etc.[45]. Since graphite's phonon dispersion, density of states, and Raman spectra is well established, it can be used as a reference point when analysing similar system. This is often the case despite the breaking of Raman selection rules and unexplained features in some spectra of carbons[45,87,90].

A typical graphite sample has the following peaks as the most observable. A G-band peak position at 1581.118 cm^{-1} (Defect free graphite), a D-band peak position may appear around 1350 cm^{-1}, a D'-band peak (depending on laser used) at 1620 cm^{-1}, and a G'/or also referred to as 2D-peak at around 2700 cm^{-1}(refer to Figure 11 for illustration)[45,87,90].

The G-band is always present in graphite, and it is a Raman active optical mode (in-plane stretching mode) with E_{2g} symmetry[45,87,90]. It represents the presence of sp^2 bonding structure where it is found[45,87]. This is in contrast to sp^3 as in the case of diamond which appears at around 1333 cm^{-1}; and for the p bonding in linear carbon chains, their Raman peaks lie around 1850-2100 cm^{-1} [45,87]. The shifting of the G-band is also often associated with stress/strain phenomena of a sample[45,87,90,91]. The shifting of the band to lower frequencies is indicative of tensile stress whereas the shifting to higher frequencies relative to the expected is considered compressive stress (see Figure 11)[90,91].

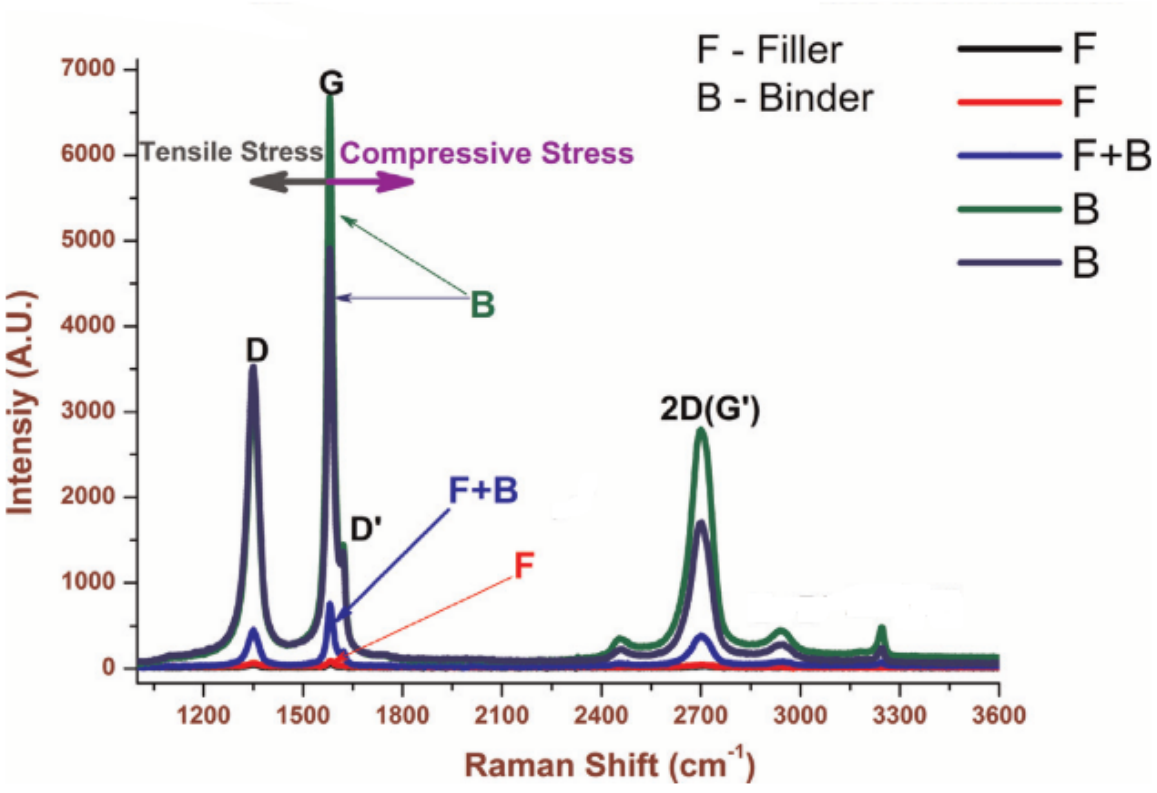

Figure 11. Raman spectra of a typical graphite like sample highlighting the most common of its peaks and the effect of stress-strain on the direction of the G-peak position. The D peak and the D' peaks are defect induced. The G peak is the sp^2 representation of the bonding in graphitic samples and its shift in position can be used to assign stress/strain distribution. The 2D appears to indicate stacking/thickness of the planar structure of graphitic samples[90].

The G-band is also expected to shift linearly with temperature in most cases (−0.02 cm^{-1}/°C in the case of graphene)[92]. The change in frequency of the G-band can be determined via a thermodynamic derivation that relates the temperature change, volume (due to thermal expansion of graphite), and pressure [92].

Rosenburg et al, investigated a silicon oxycarbide and found that the FWHM of the G-peak was stable with respect to temperature change (see Figure 13(a))[92]. Maslova et al., also found that the same FWHM did not change with laser frequency for two anthracene-based coke pyrolyzed at 2000 °C and at 2900 C[51]. Due to this stability and its linear relationship with I_D/I_G ratio, an equation was derived to calculate in-plane crystalline size[51].

The D and D' peaks are known as disorder or defect induced bands that are absent in highly crystalline graphite[45,87]. The D-band originates from disorder induced activity at the A_{1g} phonon[45]. The D-band is sensitive to laser frequency/energy and has been observed to shift strongly with laser energy by approximately 50 cm^{-1} /eV (The reason is yet to be explained) (see Figure 12)[45]. The D'-band can also appear in some disordered carbons ascribed to the splitting of the E_{2g} peak and breakdown of Raman selection rules[45,87]. The D'-peak also exhibits dispersive behaviour and sensitive to laser energy (see Figure 12)[87].

The 2D-peak or G' is knowns as the second order, overtone of the D-band[45,87]. It exists without the need for a defect and mostly utilised to determine the layer thickness of graphene/ or graphite-like samples[45,87]. The changes in the shape of the main peak and the number of peaks that can be fitted is what dictates the thickness of a highly graphitised sample[87]. It also has a dispersive behaviour and thus affected by Raman laser(see Figure 12)[87].

The common measurement in determining carbon order is the intensity ratio of the D-peak to G-peak (I_D/I_G)[45,87]. The lower the ratio the more graphitised a sample is [45,87]. A famous study by Tuinstra and Koenig in the 1970's evidence that the I_D/I_G ratio was inversely proportional to in -plane crystalline size L_a[45,87,93]. Due to the dispersive nature of the D peaks, other modification of the same equation relating crystalline size to I_D/I_G ratio have emerged[51,87,93]. Initially, a formula to include the energy of the laser was derived, then in more recent times formulas have emerged that can be used independent of wavelength of laser used; with some variations in terms of their nano-crystalline size predictability range limit[51,87,93].

Another parameter of significance that can be obtained from the Raman is the defect types which was investigated by Eckmann et al., by plotting I_D/I_G ratio against $I_{D'}/I_G$ for various modified graphene and graphite samples (see Figure 13 (b))[94]. They uncovered that a group of modified carbons sharing the same slope of I_D/I_G vs $I_{D'}/I_G$ had the same $I_D/ I_{D'}$ ratio and therefore belonged to the same defect type[94]. The $I_D/ I_{D'}$ ratio was regarded as independent of defect concentration but sensitive to only the type of defect contained within the carbon. The $I_D/ I_{D'}$ at approximately 13 is associated with sp^3 hybridisation defect, which decreases to vacancy-type defects at about 7 and finally arriving at a minimum value of 3.5 (in graphite samples) (refer to Figure 13 (b) for graphical illustration)[94].

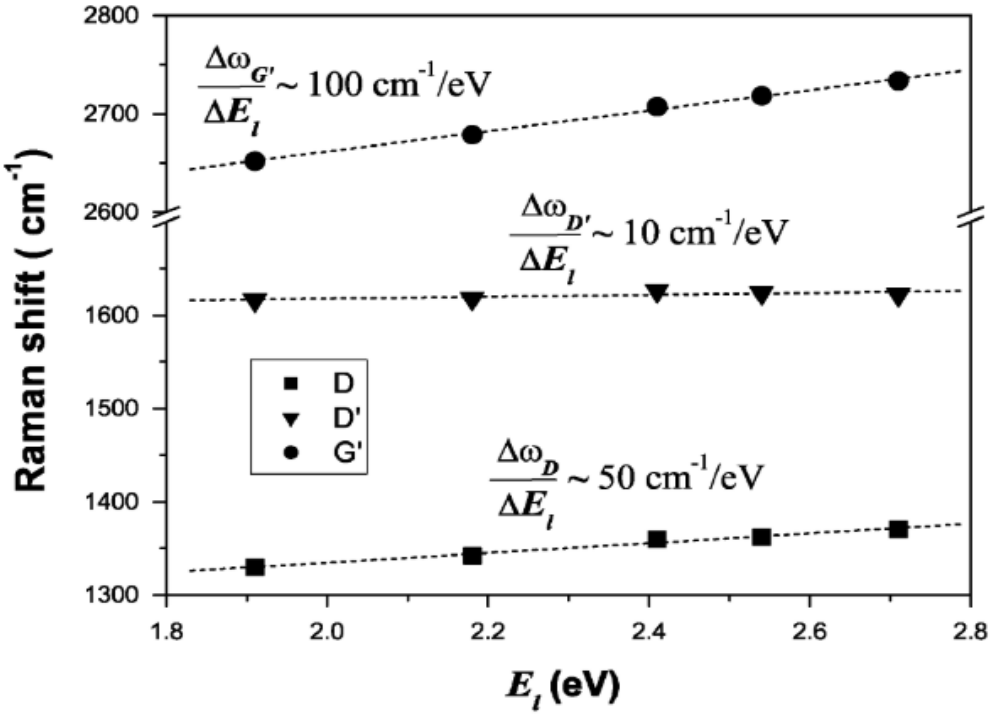

Figure 12. Illustration of the Laser energy dependence on the peak shift position of D, D' and 2D/G' peaks. The D band is known to shift position with laser by approximately 50 cm^{-1} /eV, the D' shifts by approximately 10 cm^{-1} /eV and lastly the 2D/ or G' shift s by approximately 100 cm^{-1} /eV. The laser sensitivity of these peaks must be considered when conducting experiments[87].

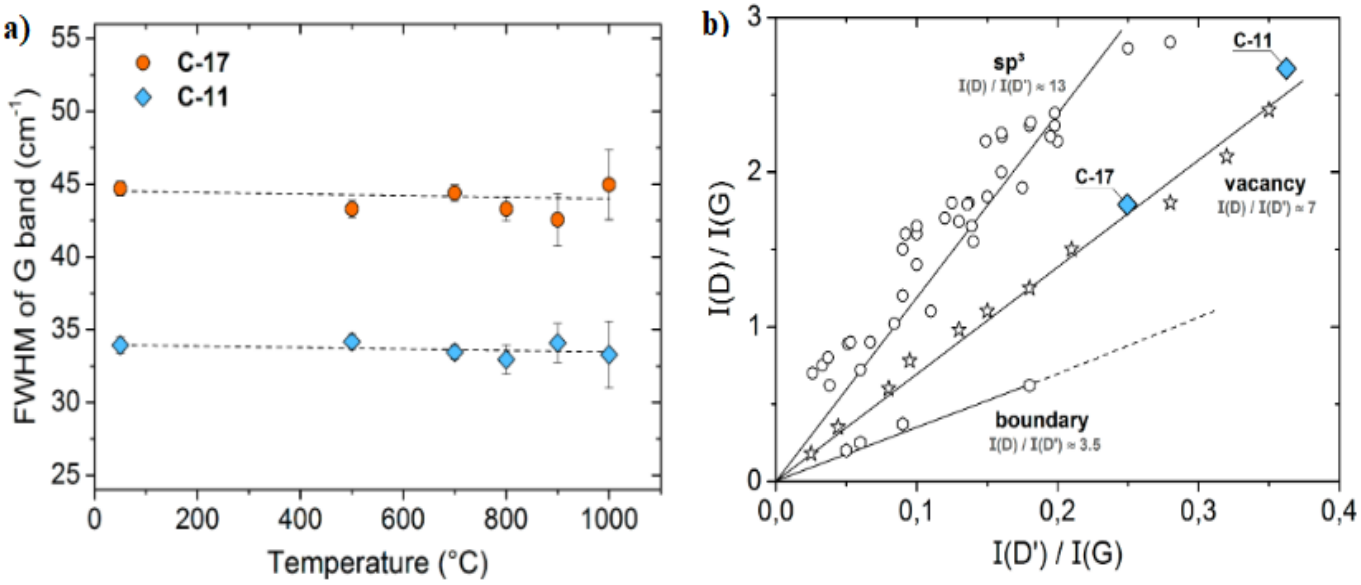

Figure 13. A silicon oxycarbide ceramic analysis of Raman showing stability of FWHM on the left and defect types on the right. a) nano-crystalline carbon FWHM stability with temperature change (C-11 and C-17; numbers denoting percentage of carbon present in the ceramic), b) defect types calculated for both C-11 and C-17 and position on master plot of defects found in modified graphene and graphite[92].

With the advancement of sophisticated Raman data acquisition and analysis software many of the challenges that were initially associated with raman spectra has massively improved[25]. Alongside instrumentation improvement such as in lasers, filters, and grating slits, the data analysis, image analysis and pre-processing capabilities included in software packages has changed the landscape[25]. Multivariate analysis methods and proprietary algorithms within Raman software allows for automatic detection and identification of Raman features in their thousands[25]. The sensitivity and intelligence of these data driven tools helps map phases in sample mixtures, uncover hidden features, statistically summarise a data sets, filter out areas of interest, conduct background subtractions, correlative image mapping, apply various peak fitting models, conduct cluster analysis, combination of image features, component analysis, and remove defect (cosmic ray removal) or mask unwanted (i.e., fluorescence effect) regions[25].

The recently developed Witec-Five plus propriety software component selection module and cluster analysis will be applied in this research to facilitate the uncovering of carbonaceous phases within a mixture of aggregates. It will unveil new insight in behaviour and superior chemometric imaging analysis in this field [25].

2.2.6.2 Basic of Model-free Kinetics, Thermal Analysis, and Its Association to Classical Kinetics

"Model free" as the name implies, allows the determination of kinetic parameter without any knowledge of the reaction model[26,29,30]. Advances within this field has allowed kinetic predictions to be made without the need for both reaction model and pre-exponential factor (A)[26,29]. MFK uses methods from thermal analysis instrumentation to directly predict kinetic parameters[26,29,30]. The common thermal analysis procedures are as follows[26,29,30,95]:

- Thermogravimetric (TG); used to measure the change in mass of a sample as reaction proceeds
- Differential/Derivative Thermogravimetric (DTG); used to measure the rate of mass change as reaction proceeds (versus Temperature for non-isothermal heating)
- Differential Scanning Calorimetry (DSC); used to measure the heat flow change into or out of the sample. Useful for determining whether a reaction is endothermic or exothermic
- Differential Thermal Analysis (DTA); measures the difference in temperature between that of the samples against a reference

In solid state reactions the concept of molar concentration used in the description of liquids and gaseous mixed phase kinetics, does not bear suitability[29]. Thermal analysis, therefore, makes use of the changes in samples weight or mass in combination with heat flow to describe reaction of solids[29]. This makes it justifiable for the use in m isoconversion methods which assess the kinetic parameters as a function of conversion[29].

Kinetic parameters determined from the MFK context should be understood as a measurement of the reaction's overall process[29,30]. Thermal analysis instruments like the Simultaneous Thermal Analyser/ or Simultaneous DSC-TGA (STA/SDT) do not have the capability to measure individual reaction steps, which in essence forms the theoretical basis of classic kinetics[29]. The analysis of a single reaction step, by classic theory is also devoid of the transport step, due to the absence of medium[26]. Rate in the classical sense is determined by the activation energy barrier height (in relation to reactants vs product) and frequency of activated complex[26].

Therefore, the activation energy in a MFK context is referred to as the global or effective activation energy (as opposed to molar activation energy found in Arrhenius's famous rate

equation) [29,30]. Its value is likely due to the combined contributions of the individual steps and their activation energy barrier[29,30]. The kinetic parameters can therefore take on behaviours not expected by the classic kinetic theory[29,30]. For example, the global activation energy has the ability to significantly change with respect to temperature, conversion and adopt values that are negative[30]. The pre-exponential factor or frequency factor which is independent of activation energy in transition state theory does not hold true in the case of MFK[26]. The pre-exponential factor is correlated to the global activation energy in a compensating manner[26,27,30]. This is observable through a graphical linear correlation if the pre-exponential factor was plotted against the global activation energy[26]. In essence, the global activation energy indicates the sensitivity to reaction rate by temperature (i.e., a temperature coefficient) whereas the pre-exponential factor represents the amplitude of that rate[26]. Increasing one directly affects the other, but they both have an effect on rate in a similar way to enthalpy and frequency factor in the transition state theory[26,30].

The expectation of having a constant kinetic parameter and a stringent focus on classical interpretation of these kinetic parameters in relation to MFK has created misconceptions[26]. These ideas are often inspired by undergraduate physical chemistry text referring to single step gas phase reactions in the absence of a medium[26]. Constancy will only be true in the aforementioned situation[26]. Where there is a medium (transport step involved) present the height of the free energy barrier will be influenced by it and any changes in temperature will in turn affect its physical nature[26] Meanings of activation energy and pre-exponential factor can also be simply taken as sensitivity to rate and the intensity, respectively[26]. It can also be supported by evidence of measured or known characteristic that influence the reaction process if known [26]

Its noteworthy that the Arrhenius equation has been a subject of criticism in that it can only be used meaningfully (in its original sense) in reactions of homogenous nature[28]. Many other phenomena follow the Arrhenius-like expression with ultimately different meaning such as Darsi-Fermi statistics (in electrons) and Bose-Einstein statistics (in phonons)[28]. The Arrhenius equation has even been used to describe temperature dependence reaction of some solid-state process (for instance: nucleation, diffusion, and nuclei growth) merely with the assumption that the system under investigation must go through the energy barrier potential and obey Boltzmann Statistics in their energy distribution along reaction coordinate[28]. Hence, its use in MFK is acceptable based on

its sound theoretical foundation and the ability to associate some physical meaning with its parameters[28].

It has been argued that obtaining of the kinetic triplet is trivial in the practical sense when using MFK approach[26,29]. One of the main purposes to obtaining the kinetic triplet is to be able to predict reactions (especially those outside the experimental region). If by obtaining the kinetic triplet, one can describe the reaction sufficiently and predict reaction outside of experimental temperature region then this becomes useful in theoretical sense too[26]. However, if this criterion is not met then there will not be a necessity to apply theoretical meanings and MFK can be described in the manner previously explained.

Highlighted in the method chapters will be the three forms of MFK equations that will be used in this study. It is recommended to use three or more heating programs[30]. The choice of which is determine by sample type and the data quality[30,96]. The non-isothermal approach will be employed in this study.

2.2.4 Review of the application of Raman spectroscopy for carbon-bonded refractories

A thorough review of literature points only to a single journal article published by Gyakwaa et al., employing Raman to directly examine the SEN, but only in relation to the study of non-metallic inclusions not preheating [86]. An alternative study conducted by Zeilke et al., did utilised Raman for evaluating the graphitisation of the carbon with respect to coking temperature in a carbon-bonded alumina filter components which is somewhat closer to the SEN in terms of composition, microstructure, and behaviour [64]. The decrease in the carbon order intensity ratio (integrated area) I_D/I_G as a function of temperature increase was equated to an increase in the planar graphite domain[64]. This was observed with samples coked at both low and high temperatures compared to their room temperature specimens suggesting an increase in graphitisation during coking[64]. It was also observed that at higher carbon contents the position of the G-peak shifts to lower wavenumber when compared against room temperature samples whereas the low coked G position remained almost constant despite the testing temperature used[64]. The shift in the G-peak position was then associated with microstructural transformation that can be used to support the decrease in strength observed at room temperature for high temperature coked samples[64]. The application of carbon-nanotube in carbon bonded refractories has also been a use case for Raman application[97–100]. Halder et al., utilised the technique to study the bonding and presence of their nanotubes inside a magnesia graphite composite[100].The research published from the work conducted in this

literature also serves as proof of scarcity in the direct examination of SEN by Raman with its carbon constituents and it is especially rare in its implication to preheating[24].

Aside from the direct examination of the SEN or within a similar aggregate system, Raman analysis has been applied to study the respective individual carbon components on their own (resin and graphite) in studies that pertain more towards the influence of manufacturing processes/or synthesis on the microstructure of the carbons[97–101]. Ko et al., demonstrated the use of Raman to investigate the processes of coking or pyrolysis on the graphitisation/or ordering of phenolic resin[102]. They were able to use crystalline size derived from Raman spectra to study the changes in structure of carbon ordering at high temperatures[102]. The L_a in plane crystalline size was observed to increase only when above 1000 °C with respect to temperature[102]. The ordering parameter of I_D/I_G ratio also decreased in trend (> 1000 °C); however, it had values above 1.5 even after heat-treatment at 2500 °C indicating that the graphitised resin was still disordered[102]. The L_c stacking order which was measured using X-ray diffraction (XRD), increased rapidly above the same temperature but only increased slightly when below 1000 °C[102]. This was indicative of randomness in structure and disorder at low temperatures during coking, and isotropic behaviour at high temperatures[102]. They also observed shifting of the wavenumber position of the resin G and D peak at higher temperatures above 500 °C[102]. A shift at 1600 cm^{-1} of the G peak was associated with a separate phase comprising of a microcrystalline order[102]. Luz et al., studied the graphitisation of phenolic resin that are used in magnesia carbon bonded refractories and preferred the use of XRD for accurate examination of stacking order crystalline size (L_c)[103]. They were not able to find any correlation between oxidation with graphitisation levels in their study using XRD method and alluded to other aspects that may be influencing oxidation such as surface area, impurity, and concentration[103]. Wang et al., evaluated the graphitisation and formation of nanotubes from pyrolysis and Fe-catalysis of phenolic resins[98]. They found that increase in pyrolysis temperature improved graphitisation[98].

In terms of graphite analysis there are many fundamental studies with respect to Raman analysis, highlighting how to gain various information such as the types of defects and quantity, graphitisation/ordering, determining stress/strain, determining of crystalline size and temperature dependence of the common observable peaks but seldom studied within an alumina-carbon bonded refractory composite if non-existent[51,64,90–92,104].

2.2.5 Review on application of Model-Free-Kinetics for carbon-bonded refractories

The application of model-free kinetics (MFK) to study the kinetics of oxidation on carbon-bonded refractories like the SEN has not been explored to the best of knowledge, despite its simplicity[24]. The core shrinking model or derived mathematical kinetic models have been used to explore the oxidation kinetics of these refractories and mostly, addressing the kinetics of MgO-C via the direct oxidation route (equation: $C(s) + O_2(g) = 2CO(g)$)[11,105,106]. The indirect oxidation where the aggregate oxide reacts with carbon can occur but only at temperatures above 1400 °C due to the stability of the metal oxides (equation: $C(s) + M_xO(s) = CO(g) + M_x(g)$; where M_x is the metal)[11,105]. Adding to the complexity of these models in terms of interpretation, is the layer of oxidised region, which is an important parameter in measuring of resistance to oxidation[11,105–107]. Lui et al., studied the indirect oxidation of MgO and found that an increase in carbon content decreased the decarburised layer but increased the effective diffusion coefficient which seemed paradoxical in apparent meaning[106]. It was explained that the molar density of carbon prevailed more than the coefficient of effective diffusion when carbon content was increased and therefore took a longer time to form the same decarburised layer as the comparator sample[106].

It is also important to note that there are other studies that have investigated various effects on oxidation such as partial pressure of gaseous species, flow characteristics, graphite flake reactivity, open porosity, effect carbon content and orientation of specimens[11,105–107].

In terms of MFK however, there are studies on carbon-carbon composites that can be utilised as preliminary information to gauge the feasibility of its application on carbon-bonded refractory composites. The existence of different phases of carbon presents the same opportunity as resin and graphite (in refractories) from a MFK analysis perspective[108–111]. And since most kinetic studies of refractories are focused on the direct oxidation route, the carbon-carbon composites share a similar trend in terms of temperature coverage and analysis[108–111].

Guo et al., used MFK to study the oxidation of carbon-carbon composites and found that, at low temperatures, oxidation was controlled by chemical reaction[108]. However, at high temperatures the reaction mostly depended on gaseous transport during the middle stages of the reaction (i.e., oxidation was stable until after 60% conversion)[108]. At the final stages of the reaction, there was decrease in reactant carbon fibres, coupled with

surface micro-depression, which meant the rate decreased as a result of reduced surface area[108].

This is somewhat analogous to the fundamental understanding of oxidation of carbon-bonded refractories[11]. Chatterjee et al., gives a detail report on the oxidation mechanism of the graphite phase deciphered by Ozgen et al., who studied an alumina-graphite composite (clay-bonded) with 30% graphite content[11]. Chatterjee et al., explains that at low temperatures up to 950 °C, the kinetics of oxidation was largely controlled by chemical reaction at the active surface of graphite and to a lesser degree controlled partly by gaseous transport via the refractories pore-structure[11]. At high temperatures the reaction mostly depended on gaseous transport through the pore-structure of the decarburised layer; to which a description of a mathematical function was derived that considers geometrical factors when assessing the kinetics at high temperatures[11].

Apart from the published research article from this literature there is scarcity in the analysis of the resin phase (whilst embedded in the refractory composite) during the oxidation kinetic degradation of carbon-bonded refractories[24]. Wang et al 2006., came close in their analysis of oxidation kinetics of a normal phenolic resin against a modified lignin-phenolic composite (with silicon additions) using the non-conversion method of MFK to compare between the resins[112]. The model free method was employed to only study the resins in isolation (in the absence of refractory aggregate)[112]. The modified resin proved to be more resistant to oxidation based on thermal analysis observation and activation energy value[112]. For further validation of this chemical resistance to oxidation of the modified resin, it was added to an alumina aggregate mix and carbonised to formed an alumina carbon bonded refractory composite, before admitting into an oxidation test. The assessment of oxidation resistance was based on the degree of decarburised layer formed (when comparing between the refractory with modified resin the one with normal phenolic resin)[112]. Their observation agreed with the MFK analysis[112]. MFK finds itself being utilised mainly in areas such as curing kinetics, synthesis, oxidation, and pyrolysis with regards to the resin phase and often investigated in the absence of a composite structure like the SEN or similar aggregate systems[95,112–114].

Chapter 3- Methodology

3.1 Model-Free Kinetics Approach

3.1.1 Fundamental Equations

The solid-state kinetic expression of rate degradation/oxidation is illustrated in Equation 1[26]. $\boldsymbol{d\alpha/dt}$ defines the time rate of reaction, which is represented as a function of both temperature and conversion in the term ***K (T)*** and ***f(α),*** respectively[26,30,32,115]**.** ***f(α)*** is indicative of the driven mechanism for the reaction[26].

$$\frac{d\alpha}{dt} = K(T).f(\alpha)$$

[1]

Equation 2 is used in the calculation of conversion from mass change during sample oxidation. Where the $\mathbf{m_o}$ equates to initial mass of sample, $\mathbf{m_t}$ is the calculated mass at each time-point during the process of oxidation reaction, and finally the $\mathbf{m_\infty}$ denotes the final mass residual at the end of the reaction [26,30,32,115].

$$\alpha = \frac{mo - mt}{mo - m_\infty}$$

[2]

In Equation 3 ***K*** in the Arrhenius representation can be used to calculate the rate constant as depicted below:

$$K\ (T) = A\ exp\frac{-E}{RT}$$

[3]

Where the activation energy is denoted as ***E*** (kJ mol^{-1}), ***R*** is the gas constant 8.314 $JK^{-1}.mol^{-1}$, ***T*** is the absolute temperature measured in Kelvin and ***A*** is pre-exponential factor/or Arrhenius constant (min^{-1})[32–38].

$$\beta = \frac{dT}{dt}$$

[4]

In Equation 4 β represents the heating rate of the most commonly employed non-isothermal heating program under thermal analysis[29,30]. It represents the linear change in temperature over time[30]. Operators of the thermal analysis program can decide on whether to use an isothermal temperature setting, where T (temperature) is constant i.e., T = const. or employ the common non-isothermal setting where T changes with time T=T(t)[30].

From Equation 3, we can observe that rate constant K has a dependency on temperature and therefore can be utilised for the general/or commonly used non-isothermal case description[24,29]. By taking Equation 1 and transforming it into the general, non-isothermal case with the use of the temperature dependent term of heating rate "β", Equation 5 is conceived[24,29].

$$\frac{d\alpha}{dt} = \beta . \frac{d\alpha}{dT}$$

[5]

Equation 6 results in the combination of the aforementioned equations forming the basis for all non-isothermal kinetic reactions[24,29].

$$\frac{d\alpha}{dt} = \beta . \frac{d\alpha}{dT} = K(T) . f(\alpha) = A . f(\alpha)\, e^{\frac{-Ea}{RT}}$$

[6]

3.1.2 Isoconversion Methods

By utilisation of Equation 6, derivations of the most prominent methods of the isoconversion have emerged, notably: Kissinger–Akahira–Sunose (KAS), Ozawa-Flynn-Wall (OFW), Friedman, and Vyazovkin method respectively, in the Equations: 7, 8, 9 and

10[24,29,30]. As alluded to in previous sections, these methods produce multiple sets of kinetic parameters for E and A based as a function of conversion[24,29,30].

$$ln\left(\frac{\beta_i}{T_{\alpha,i}^2}\right) = ln\left(\frac{A_\alpha R}{g(\alpha)E_\alpha}\right) - \left(\frac{E_\alpha}{RT_{\alpha,i}}\right)$$

Kissinger-Akahira-Sunose equation

[7]

$$ln\,\beta_i = ln\frac{A_\alpha E_{\alpha,i}}{Rg(\alpha)} - 5.3308 - 1.052\left(\frac{E_{\alpha,i}}{RT_{\alpha,i}}\right)$$

Ozawa-Flynn-Wall equation

[8]

$$ln\left(\frac{d\alpha}{dt}\right)_{\alpha,i} = ln[A_\alpha\, f(\alpha)] - \left(\frac{E_\alpha}{RT_{\alpha,i}}\right)$$

Friedmann equation

[9]

$$\phi(E_\alpha) = \sum_{i}^{n}\sum_{i\neq j}^{n}\left(\frac{I(E_\alpha, T_{\alpha,i})}{I(E_\alpha, T_{\alpha,j})} \cdot \frac{\beta_j}{\beta_i}\right)$$

Where, temperature integral is:

$$I(E_\alpha, T_\alpha) = \int_0^T exp\left(\frac{-E_\alpha}{RT}\right) dT$$

Vyazovkin method

[10]

For all equations above with the exception of Vyazovkin, the activation energy and pre-exponential factor are obtained by using variables on the left side and plotting it against 1/T (where β denotes heating rate and α, i; are a function of both the conversion and

heating rate) of the last part of the above equations[24,30]. The slope of the graph and its intersect are used to derive the apparent activation energy and pre-exponential factor[24,30].

In Equation 10, n represents the number of heating rate, $T_{\alpha,i}$ is referred to as the thermodynamic temperature for each so called "ith" heating rate[26,116]. The activation energy values are obtained by minimising the function $\phi(E_\alpha)$[26,115,116]. Activation energy is determined for each conversion by solving the temperature integral in the minimisation function.

From Equation 7, 8 and 9, it appears as though, that the true value of the pre-exponential factor is associated with knowing the reaction model. However, the emergence of Vyazovkin methods and the compensation effect equation makes it possible to determine the pre-exponential factor without the need of a model[26,27,116]. Plotting the values of slope (i.e., activation energy values of conversion) against intersect values (of pre-exponential factor) gives an equation of line in representing the compensation effect. Two constants a and b can be derived from the Equation 11 to then optimise or better predict the pre-exponential factor (E and A are the activation energy pre-exponential factor respectively)[26,27].

$$lnA = aE + b \quad [11]$$

Equation 7, 8 and 10 are classed as integral form of the isoconversion equations whereas the Equation 9 is considered derived as a differential method[29,30]. All of the integral forms therefore relate to Equation 6 derivative form by the following series of equations which share a common base in Equation 12[24,29,30,39]:

$$g(\alpha) = \int_0^\alpha \frac{d\alpha}{f(\alpha)} = A \int_0^t exp\left(\frac{-E}{RT}\right) \text{ dt} \quad [12]$$

$$g(\alpha) = \int_0^\alpha \frac{d\alpha}{f(\alpha)} = \frac{A}{\beta}\int_0^T exp\left(\frac{-E}{RT}\right) dT = \frac{AE}{\beta R}p(x) \cong$$

$$g(a) = \frac{AE}{\beta R}\, e^{-x}\left[\left(\frac{1}{x}\right)^{2} - 2!\left(\frac{1}{x}\right)^{2} + 3!\left(\frac{1}{x}\right)^{3} ..\right]$$

[13]

$$p\,(x) = \; e^{-x}\,\left(\frac{1}{x^{2}}\right)$$

[14]

The temperature integral p(x), where x=E/RT, does not appear to have an analytical solution which warranted approximations to be derived (depicted in Equation 12 and 14)[24,36,39,114]. These derivations made it possible to derive the integral form of the model free equations listed above by way of mathematical re-arrangement and transferring equation between the base equation 6 and those corresponding to equation 11 [24,30,36,39,114]. In terms of the KAS method the approximation used was the Frank-Kameneskii approximation[24,39]. It had the values of x as "20 < x < 50" through which the KAS equation was derived[24,39]. Derivation of the OFW equation was done by utilising Doyle's approximation with values of x to be between "20 < x < 60" [24,36,39,114]. The temperature integral can also be approximated by using the fourth Senum and Yang approximation which often used in the Vyazovkin method[28,96,117].

The Vyazovkin method is now the most advanced and accurate method in terms of predicting kinetic parameter by way of mathematical minimisation of equation 10 to obtain activation energy[26,30,116]. It is more complex in computation, however, a MATLAB code, supplemented with additional equation of deriving pre-exponential factor and reaction model is freely available[116]. To make it even more accessible a software built from this code is available for predicting Vyazovkin kinetic triplet simply by importing thermo-analytical data into the kinetic software which can makes its adoption in industry more promising[116]. The work conducted in this literature will use the software method to employ the Vyazovkin kinetic predictions[116]. The software will use the columns of temperature, time, DSC, and the mass from the thermo-analytical data to perform the necessary predictions[116].

3.1.3 Non-Conversion Method

The most basic forms of the model free equations are those that produce a single kinetic parameter for the entirety of the reaction[24,30,118]. These are termed non-conversion

methods of model free. This attribute makes them unsuitable for the assessment of reaction complexities, however interesting discussing have emerged in literature about their use in determining the rate limiting step of reaction[24,29,30,117,118]. Sbirrazzuoli et al., mentioned that predictions of kinetic parameters using these methods are associated with 50% conversion[119]. Assessment of this hypothesis will be crucial in this experiment and in learning the various ways in which model free equations can be employed. It is also important to note that the derivation of the Kissinger method obeys a limit law that of first order reaction model (f(α)=(1-α)) which makes it not entirely model free from a mathematical standpoint[29,30]. The equations mentioned in previous sections are similar to the ones in this section but only differ on the basis of conversion.

$$ln\left(\frac{\beta}{T_p^2}\right) = ln\left(\frac{AR}{E}\right) - \left(\frac{E}{R}\frac{1}{T_P}\right)$$

Kissinger equation

[15]

$$ln\,\beta_i = ln\frac{AE}{Rg(\alpha)} - 5.3308 - 1.052\left(\frac{E}{R}\frac{1}{T_P}\right)$$

Ozawa equation

[16]

By plotting the first part of equation against $1/T_{p,}$ with T_p representing the maximum peak temperature from the DTG curve, an Arrhenius plot is produced, where the slope and intercept represent activation energy and pre-exponential factor[24,29,30]. The simplicity of these equations makes them a popular choice for comparing degradation of similar compounds which degrade within similar regions[24,29,30].

3.2 Materials, Preparation, and Identification

Three Submerged Entry Nozzles (SENs) of the same product (mixture) were examined and provided for by sponsor company TATA-Steel Strip UK ltd. The direct examination of the port was of major interest (see Figure 14 B and C for sampling locations), due to it being the most common failure location. It also presents major sampling challenges in terms of geometry, brittleness and limited sampling numbers that can be obtained from it.

The conditions at which the three SENs were provided is as follows:

- A Virgin SEN that has not been gas flare by the sponsor company
- A 3-hour preheated SEN that has undergone gas flared (natural gas) preheating for 3 hours in an open atmosphere as done in practise
- A 6-hour preheated SEN that undergone has undergone gas flared preheating for 6 hours in the same environment as above

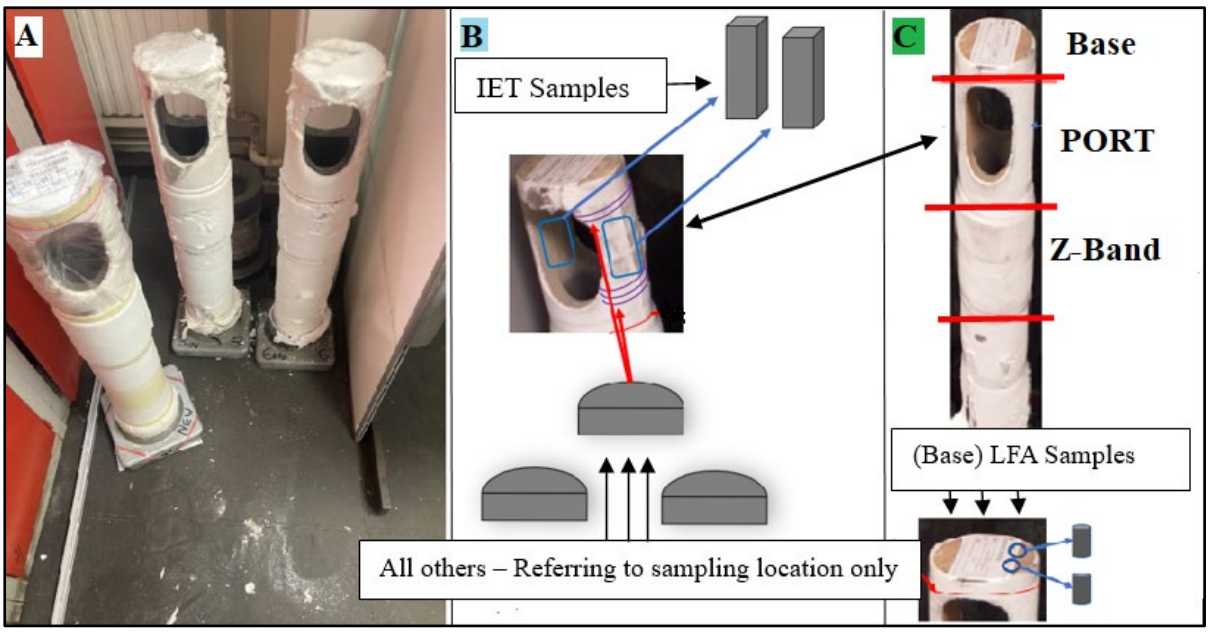

Figure 14. The three SEN provided by sponsor company and sampling locations. A) Image of the three SENs, two of which are preheated (one for 3 hours and the other for 6 hours) and a Virgin SEN (that was not preheated). B) Shows the location (Port) of IET samples (of which, only two can be obtained per SEN) and the general samples for other characterisation techniques other than LFA. C) Shows the sampling location (which is labelled as base) for LFA analysis.

Samples were cut to dimension of variable sizes depending on test method to be employed. Initially, the entire SEN was allocated to Swansea University's work-shop technician staff to section various parts of the SEN to about 3mm thickness using various saws blades/carbide or diamond blade cutters. Further cutting of samples into smaller subsection were then conducted using a variety of approaches as follows:

- Type: IsoMet 1000 precision saw with diamond blades were used for cutting through medium to small section of the SEN with precision whilst working in external facility (see Figure 15)
- Type: Magnusson 6.49" Coping saw was used to cut through smaller defined square sections
- 40 – 80 grit sanding paper was also used to remove small quantities of material for weight consistency useful for MFK analysis

Figure 15. IsoMet precision saw cutting a subsection of the SEN piece (left), the middle image shows a cut sample for IET analysis being weighed, and on the far right a set of samples mounted on a stub in readiness of µ-CT-Xray tomography scan.

The aforementioned tools were suitable for samples intended for Raman, µ-CT, thermo-analysis, XPS. The samples for the LFA and IET were specially cut by Swansea University's workshop technician staff who experience a great deal of difficulty in cutting these samples to specified work order dimensions.

For the initial characterisation of the SEN's composition, an Attenuated Total Reflectance - Fourier Transform Infrared (ATR)-FTIR spectroscopy by Themo Scientific (Nicolet iS10) was used within the range 500 – 4000 cm^{-1}. The Virgin SEN was examined in the initial stage since all of the SENs to be examined were of the same product. Furthermore, the elemental analysis or compositional analysis was only to confirm the major compositions present[REDACTED].

Subsequently, for the work reported in this thesis, elemental analysis with Energy Dispersive x-ray Spectroscopy (EDX) was used as a supplement to characterise all three SENs using various area scans on. The SEM Hitachi TM4000-plus and version TM3030-plus, Tabletop Scanning Electron Microscopy (SEM) (Hitachi High Technologies America, Inc.) couple with EDX detector (Silicon drift detector with area coverage of 30 mm^2, manufactured for Hitachi by Oxford Instrument Analytical Ltd) was used in identifying the elements with various settings. An accelerating voltage of (15000 volts) with magnification of (x30), a working distance of (9420.73 μm for TM4000-plus and 12300 μm for TM3030-plus), emission current of (43200 nA for TM3030-plus and 48800 nA for TM4000-plus). Refer to the appendices to visualise the area scans taken from the SEM version TM4000-plus using BSE signals (back scattered electron detector) to image and acquire composition detailed below using Table 1, Table 2, and Table 3:

Table 1. An EDX elemental analysis of the Virgin SEN, highlighting the major composition of elemental aluminium and silicon present that make up the refractory. These metals in the form of alumina and silica were observed by utilising ATR-FTIR analysis in conjunction. The SEM Hitachi TM4000-plus coupled with EDX SSD was used to map and analyse three areas and combined the results shown

Map Sum Spectrum of 13, 14 and 15 for Virgin SEN				
Element	**Line Type**	**Weight %**	**Weight % Sigma**	**Atomic %**
Na	K series	2.43	0.13	3.10
Mg	K series	0.99	0.11	1.20
Al	K series	73.30	0.70	79.56
Si	K series	9.55	0.27	9.96
P	K series	0.74	0.27	0.70
K	K series	0.48	0.16	0.36
Ca	K series	2.02	0.18	1.48
Ti	K series	0.98	0.22	0.60
Zr	L series	9.50	0.71	3.05
Total		100.00		100.00

The SEM TM3030-plus version was used at time where part of this literature was published in a peer reviewed journal to supplement the findings of titania present in the refractory and detectable by Raman[24]. The corresponding analysis will be found in the main text.

Table 2. An EDX elemental analysis of the 3 hours preheated SEN (3-hour), highlighting the major composition of elemental aluminium and silicon present that make up the refractory. These metals in the form of alumina and silica were observed by utilising ATR-FTIR analysis in conjunction. The SEM Hitachi TM4000-plus coupled with EDX SSD was used to map and analyse three areas and combined the results shown.

Map Sum Spectrum of 16,17 and 18 for the 3-hour SEN				
Element	**Line Type**	**Weight %**	**Weight % Sigma**	**Atomic %**
Na	K series	3.41	0.12	4.13
Mg	K series	0.95	0.10	1.09
Al	K series	72.03	0.61	74.37
Si	K series	16.51	0.29	16.37
P	K series	0.65	0.23	0.59
K	K series	0.98	0.16	0.70
Ca	K series	1.61	0.17	1.12
Ti	K series	1.65	0.21	0.96
Zr	L series	2.21	0.64	0.67
Total		100.00		100.00

Table 3. An EDX elemental analysis of the 6 hours preheated SEN (6-hour), highlighting the major composition of elemental aluminium and silicon present that make up the refractory. These metals in the form of alumina and silica were observed by utilising ATR-FTIR analysis in conjunction. The SEM Hitachi TM4000-plus coupled with EDX SSD was used to map and analyse three areas and combined the results shown

Map Sum Spectrum of 19, 20, 21 for the 6-hour SEN				
Element	**Line Type**	**Weight %**	**Weight % Sigma**	**Atomic %**
Na	K series	2.96	0.13	3.56
Mg	K series	0.43	0.10	0.48
Al	K series	70.98	0.63	72.58
Si	K series	20.45	0.33	20.09
P	K series	0.91	0.23	0.81
K	K series	0.61	0.17	0.43
Ca	K series	1.13	0.17	0.78
Ti	K series	1.86	0.23	1.07
Zr	L series	0.67	0.66	0.20
Total		100.00		100.00

From the FTIR data obtained the main constituents were attributed to alumina and silica, based on assignment peaks ranging from 951 cm^{-1} to 1381 cm^{-1}[120–122]. This was supported by EDX analysis conducted on all three SENs.

Other peaks were identified. Typical carbon peak for sp^2 hybridised C=C double bond around 1540 cm^{-1} to 1650 cm^{-1} could not be resolved, however 951 cm^{-1} was designated to C–H bending vibration of sp^2 hybridized bonding [44]. Peak position of 3645 cm^{-1} is usually attributable to adsorb water and O–H stretching[122,123]. The peak identified at 2980.5 cm^{-1} and 2881.7 cm^{-1} is associated to Al–O and alkane C–H stretching, respectively[123,124]. Instrument signatures were also observed at 1973.4 cm^{-1}, 2031.7 cm^{-1} and 2152.2 cm^{-1} [125,126]. The FTIR results can be referred to in the appendices.

No sample preparation was required for conducting the above elemental characterisation. The graphite in the refractory is conductive however, a carbon tape was used to mount samples onto the SEM holder for analysis.

3.3 Characterisation

3.3.1 Thermo-kinetic Analysis

TA thermal analysis instrument, SDT Q600 was used to gather the data required for distinguishing of carbon oxidation behaviour. The data obtained from the SDT was used in the model free kinetic evaluation. The SDT was also used to oxidised samples (from Virgin SEN) intended for Raman depth scan in the initial stages of developing method knowledge on cluster technique and sample behaviour.

- For the model free kinetics analysis, all samples assessed had the following parameters: non-isothermal heating rates of 3, 11, 27 °C/min were employed. A gas flow rate of 100ml/min (air) was used in the chamber. Weight measured for tested sample was approximately 17±3 mg[24]. The TA software provided a useful interface to visualise, extract and pre-process data into derivatives forms with units of interest and deciphering conversion. Data analysis and graphical plots of the various model fee equations were conducted in excel and Origin software.
- Both the Virgin SEN and the preheated SEN underwent the same experimental treatment aforementioned. 3 samples run were conducted for each SEN. This comes after trialling out repeated heated rate on the extreme or higher heating programs selected for better accuracy as recommended [30].

- To better understand the non-conversion method and the single activation energy achieved by this method; isothermal experiments were conducted and evaluated against predicted reaction rates (from the non-conversion predicted kinetic parameters). The Virgin SEN was utilised in this part of the study, to firstly conduct the model free experiment detailed above. An additional, three isothermal oxidation experiments were then conducted at 510 °C, 540 °C and 570 °C with an initial flow rate of 95 ml/min (in argon) in a non-oxidising environment until the required temperature was reached before changing into an oxidising environment (in air) at a flow rate of 100 ml/min[24]. The output of the model free kinetics results (slope value, intersect, DTG peak temperature in kelvin) were then used as inputs to the Arrhenius equation to firstly uncover what it predicts and then to compared against the isothermal experiments.
- For the Raman oxidation tracking capability and development of method understanding regarding the use of cluster technique, isothermal experiments were conducted on 8 samples. The first 4 sample's oxidation temperature was set to 510 °C, with time stamps of 1,2,3, and 4 minutes oxidation[24]. The lower temperature ensured that only the resin phase will oxidise to allow the unique analysis and insight or preferential oxidation[24]. The other 4 samples were oxidised at 900 °C with the same time intervals[24]. A non-oxidising environment was used (argon) at a flow rate of 95 ml/min until the desired isothermal temperature was reached before switching to an oxidising environment of air at a flow rate of 100 ml/min[24].

The SDT chamber used for the thermo-analysis contains an alumina pan of 90 µl to which samples were placed[24]. The sample pan and reference pan are inserted into the bifilar wound furnace of the chamber. The sample balance has a sensitivity of 0.1µg and it equipped with a Platinum-Rhodium (Type R) thermocouples for monitoring temperature (differential thermal analysis capability) with sensitivity of 0.001 °C[24].

3.3.2 Raman Spectroscopy Analysis

WiTec Alpha 300R Confocal Raman laser microscope was used in conducting this study with advance software capabilities. The equipment was accessed at the Material Research Facility at Culham Science fusion centre. The WiTEC project five plus software capability was used to process and analyse the data. The component identification module and the cluster analysis algorithm were used in identifying and distinguishing different carbon signatures and mapping their respective locations.

- For Raman oxidation tracking study (method development understanding of samples and cluster technique), samples were initially oxidised by SDT thermal analyser prior to the using the WiTec Alpha 300R Confocal Raman laser microscope with the following settings. Depth scans were conducted on samples, the choice of which was inspired by the amount of expected oxidation and assessment of reach required to resolve clusters. The depth scan profile was set to a scan width of 80 µm and depth of 70 µm[24]. Number of points chosen per line and line per image were set at 200. "Scan speed [s/Line], retrace speed [s/Line], and integration time were set at 4.0, 0.50 and 0.02, respectively"[24]. A fast-scanning mode was used by selecting a high speed and low intensity setting with the EMCCD detector (1600 x 200 pixels)[24]. EMCCD gain was 230 and preamplifier gain was set to 1. Laser wavelength of 532 nm, laser power of approximately 15 mw and a 600 g/mm grating were used[24]. The objective magnification which was set to 10x as the final setting parameter. The scan conducted amounted to a total of 40000 scans per image from which statistical data can be derived[24].
- For the high temperature scans, a Linkam TS1500 environmental heating stage was purged with argon gas and used to modulate the temperature whilst conducting scans. The environmental chamber crucible was 7mm in diameter and 3mm in depth. Samples investigated were approximately 2mm x 2 mm (length vs depth). The objective was set at 50x, with depth scan area of 30 µm x 30 µm[24]. Points chosen per line and line per image were both set at 100. Scan speed [s/Line], retrace speed [s/Line], and integration time were set at 5.0, 0.50 and 0.05, respectively[24]. Laser power used was approximately 14mw, with the same laser wavelength and grating as above[24].
- For Raman analysis comparing Virgin SEN, 3-hour and 6-hour SEN, lateral area scan instead of depth was adopted, building on from knowledge acquired at the previous experiment (Raman oxidation tracking study above). In a perfectly preheated condition, there is a possibility that the sample will not oxidise or in such an amount that is not is easily distinguishable. Therefore, the horizontal scan will be most suited and sensitive to surface changes. The depth scan during the method development stage would have given a good understanding of the bulk effects within the samples. Scan locations were initially tracked from the coating region to the main bulk to assess the most suitable and consistent areas for

profiling which will reveal insight of microstructure. The area dimension used was scan width of 70 μm and scan height of 80 μm. The remaining setting were the same as the Raman oxidation tracking study settings above.

3.3.3 XPS Analysis

XPS Analysis was performed using a Thermo NEXSA XPS fitted with a monochromated Al kα X-ray source (1486.7 eV), a spherical sector analyser and 3 multichannel resistive plate, 128 channel delay line detectors. All data was recorded at 19.2W and an X-ray beam size of 400 x 200 μm. Survey scans were recorded at a pass energy of 200 eV, and high-resolution scans recorded at a pass energy of 40 eV. Electronic charge neutralization was achieved using a Dual-beam low-energy electron/ion source (Thermo Scientific FG-03). Ion gun current = 150 μA. Ion gun voltage = 45 V. All sample data was recorded at a pressure below 10^{-8} Torr and a room temperature of 294 K. Depth profile was performed using Ar 4000+ eV monatomic mode with raster size of 2x2 mm^2 for 600s (etching rate 0.57 nm/s ref. Ta2O5).

Data was analysed using CasaXPS v2.3.20PR1.0. Peaks were fitted with a Shirley background prior to component analysis. Lorentzian Asymmetric Lineshapes of (1.5,3,243) were used to fit components. C KLL Auger peak analysis was conducted applying a synthetic differential to obtain the D-parameter. The D-parameter serves as a more reliable method for determining sp^2/sp^3 ratio for this work.

2 samples were taken from each SEN (the Virgin SEN, the 3 hours preheated SEN and the 6 hours preheated SEN) for scanning. Each sample had a scan that was non-etched and then another after being etched to create an opportunity for deciphering carbon phases present. The results were then combined for each SEN category during analysis of results. The groping was based on 2 factors, etched or non-etched and the SEN from which the samples were taken.

The x-ray photoelectron (XPS) data collection was performed at the EPSRC National Facility for XPS (“HarwellXPS”), operated by Cardiff University and UCL, under Contract No. PR16195.

3.3.4 μ-CT Analysis

The ZEISS Xradia 620 Versa μ-CT was used to scan samples at the Henry Moseley X-ray Imaging Facility at The University of Manchester. Samples were mounted onto a rotating stage (360) and scanned with acceleration voltage of 100 kV and current set at139.95 μA. Exposure time was set in range of 1- 2 seconds, source filter choice was LE5, and optical

magnification was set at 4X. There were approximately 2002 image projects per scan with a resolution between 1.6 and 2.7 μm per voxel (depending on exposure time). Image reconstruction was conducted with inbuilt scout and scan software version 16.0.1. Avizo-amira software at Swansea University was used to analyse the data by applying threshold segmentation to differentiate composite components and create measure for evaluation. The virgin, and preheated samples were examined during this study.

3.3.5 IET Analysis

Impulse Excitation Testing/Technique (IET) was conducted at the Materials Research Facility at Culham science fusion centre with the Grindosonic Mk7 Impulse excitation tester. Impulse excitation had a frequency range 20 Hz – 100 kHz and can provide various data such as acoustic wave dampening data, Elastic Young's modulus, Shear modulus and concrete strength. Rectangular sample geometry measurement, sample weight, and Poisson ratio (0.3) were used as input data into the instrument to determine the elastic Young's modulus. The SEN rectangular samples were excited by a small striking projectile, and its oscillation frequency was then measured using a microphone. The flexural excitation mode was used to determine the mechanical properties of the material. The Fourier transformed frequency spectrum was extracted and then used to determine dampening parameters. The virgin, 3-hour preheated SEN and 6-hour preheated SENs were all tested at room temperature. The sizes of the samples were approximately: length of 73.84 ± 0.08 (mm); width of 20.41 ± 1.63 (mm); depth of 5.54 ± 0.32 (mm) and weight of 23.02 ± 2.92 (grams). Only two samples can be taken from each SEN's port. Difficulty in cutting the samples to the exact dimensions meant that each SEN with its two samples will vary slightly.

3.3.6 LFA Analysis

Thermal analysis was examined to understand the implication of preheat on the thermal properties by utilising Netzsch 457 MicroFlash Laser Flash Analyser (LFA). Cylindrical samples were cut from the base of the SEN using precision power tooling by Swansea University's Workshop technicians. Sample size for LFA was ~ 12.8 diameter and sample thickness of ~ 3-4mm. The LFA is equipped with a Indium antimonide (InSb) sensor, laser filter was set to 100 mm, argon purged at a flow rate of 100ml/min. Samples were irradiated with a short laser pulse from one side and on the opposite side the time taken to for the heat pulse travel is measured by an infrared camera. These results in the calculating of values of thermal diffusivity, specific heat capacity and thermal conductivity by way of inference using a known calibration sample.

Chapter 4- Carbon Oxidation Phase Profiling

4.1 Assessment of Non-conversion model free via oxidation profiling of Resin phase

The non-conversion model free kinetic (MFK) methods only yield a single activation energy value and does not provide means for evaluating the complexity of a reaction behaviour[24,29]. It is however important to understand whether more information can be derived from it, despite its simplicity to use[24,29]. To determine whether the non-conversion method is representative of the rate limiting step as mentioned by Svoboda and Malek, or the maximum rate at 50% conversion as suggested by Sbirrazzuoli et al., two of the most commonly used methods were assessed and validated against isothermal experiments[117,119]. The non-conversion MFK analysis should facilitate a way to understand whether rate can be predicted if values were substituted into the famous Arrhenius equation.

Before delving into the kinetics, this section also explores how to gather meaningful information from the thermo-analytical output of a TGA and DTG data plot. The DTG from Figure 16 shows the rate of weight loss due to oxidation of carbon as a function of temperature increase for both the resin phase and graphite within the refractory. The resin phase (being a lower order carbon) as expected oxidised at lower temperatures than the graphite[24]. The DTG peaks for each respective heating rates: 3 °C min-1, 11 °C min^{-1} and 27 °C min^{-1} were distinctive enough for analysis using model free approaches[24]. The peak temperatures from the DTG (T_p (K)) curve and their respective heating rates (β) were used to plot the Kissinger and Ozawa method as depicted in Figure 16. The effect of heating rate on the resin is observed to shift the DTG peak position to higher temperatures but with lower peak maximum values. The lowering of the peak maxima is indicative oxidation resistance[24]. The shift in temperature coverage, however, is due to the accelerated heating of the sample exterior relative to its interior[127,128].

The TGA analysis clearly depicts the mass changes of the resin and graphite phase. Two major stepwise drop regions were observable. The onset of oxidation on the TGA plot was observed to vary as a function of heating rate by shifting slightly to higher temperatures. The onset of oxidation may be of prime importance in design solutions. A reasonable rate of heating can be explored to delay the onset of oxidation so long as it does not compromise the material integrity[1,24]. Industrials trials conducted by Svensson et al, demonstrated that a steel plant with the highest heating was more effective

in protecting the SEN from oxidation[1]. They attributed this to reaching the desired temperatures that densifies the glass protective coating much faster[1]. This is, therefore, an additional benefit when the kinetics (onset delay) is also considered as highlighted in this study.

The kinetic values of activation energy and Arrhenius constant are displayed in Table 4. The values of activation energy for both methods produced were equivalent (242 kJ/mol). Their graphical representation is show in Figure 16 b, and Figure 16 c. From the slope of each graph, their activation energy values were determined (Kissinger and Ozawa) with good linear fitting (R^2 of 098453 and 0.98598 respectively)[24].

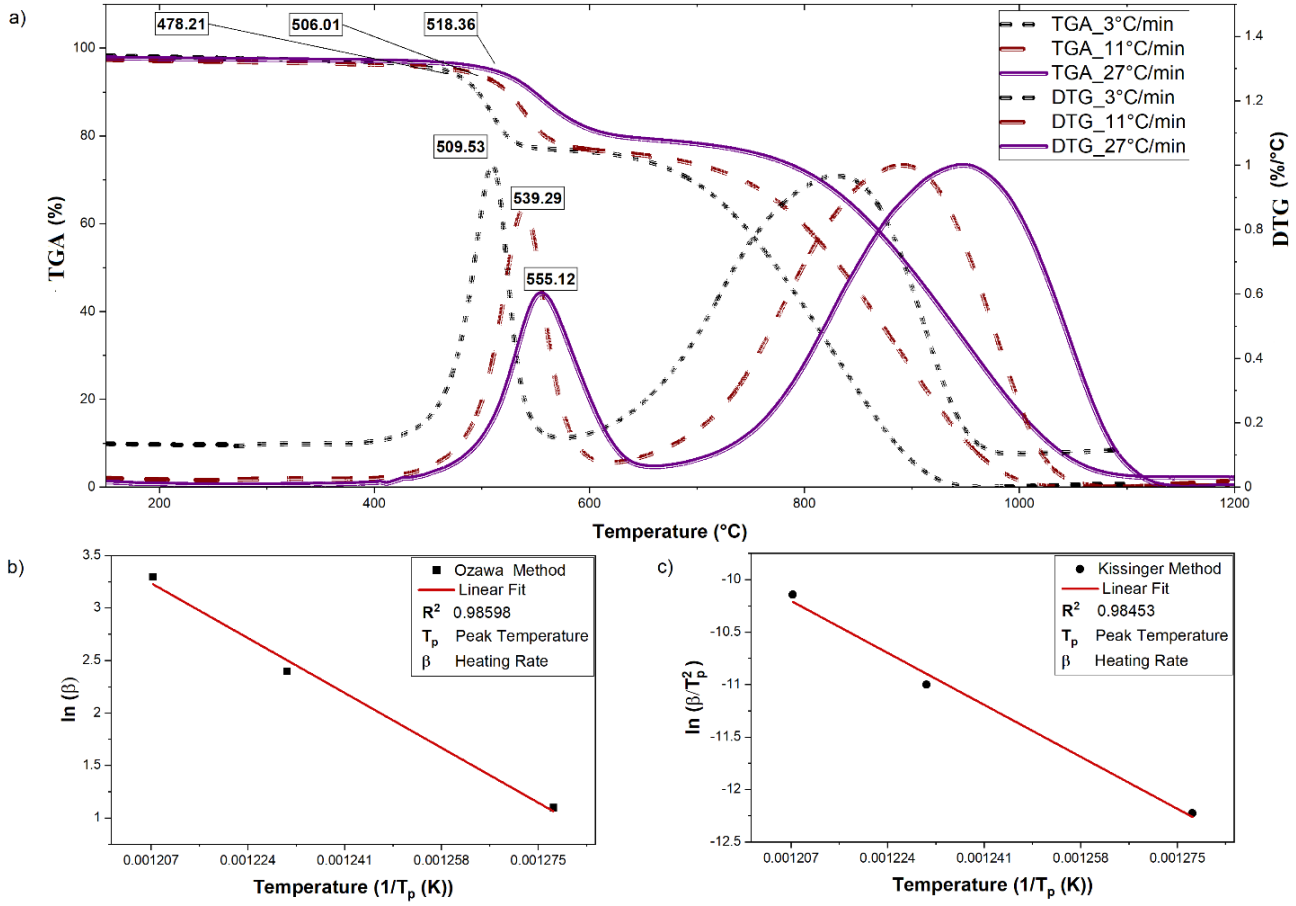

Figure 16. a) Shows the weight loss due to oxidation of carbon as a function of temperature increase for both the resin phase and graphite within the refractory the refractory. Peak positions of resin and DTG highlighted alongside their respective onset oxidation point b) shows the Ozawa Arrhenius Plot, c) Shows the Kissinger Arrhenius plot. The heating rate is β; T_p denotes peak temperature[24].

Table 4. The activation energy and Arrhenius parameter values for both Kissinger (α) and Ozawa (β) are displayed. The symbol "(*)" is indicative of Arrhenius parameter using variable heating rates with Kissinger's equation re-arrangement. The symbol "(Δ)" refers to the Arrhenius derived from intercept of the slope[24].

E(kJmol^{-1})	**ln A**	**A**
	$35.28_{(*)}$	$2.09E+15_{(*)}$
	$35.13_{(*)}$	$1.82E+15_{(*)}$
$242.11_{(\alpha)}$	$35.31_{(*)}$	$2.17E+15_{(*)}$
$242.84_{(\beta)}$	$40.34_{(\Delta)}$	$3.31E+17_{(\Delta)}$

For the Ozawa method, its value of arrhenius constant was derived from the intercept of the slope. For the Kissinger method re-arrangement of its equation can generate values of Arrhenius constant as a function of heating rate that show a better prediction[24]. The same equation was used by xu et al., in their study of curing kinetics[129]. Nevertheless, their intercept values, from the slope of each graph were compared. The order of magnitude difference between their constants decreased from 7 to 2, when the equation method was used to calculate the Arrhenius constants for the Kissinger method[24]. This could suggest an improvement in Kissinger's prediction with the use of the equation-based method since the activation energy values of both methods were practically the same[24].

The differences between their Arrhenius were analysed using equation 3 rate constant formulae by using the kinetic values obtained from the model free predictions and isothermal experimental temperatures as inputs. The isothermal temperatures that were used to validate findings were: 510 °C, 540 °C and 570 °C[24]. The broad choice of selected temperatures was conducted in order to clarify the capabilities of these MFK models in predicting initial DTG rates or their peak maximum rate at these temperatures[24].

For each isothermal experiment conducted their maximum DTG peak value was determined as follows: 0.3367%/min for 510°C, 0.3675%/min for 540 °C, and 0.4637%/min for 570°C[24]. The predictive rates constants calculated for the Kissinger were deemed be too low (~ 0.0025 %/min for 510 °C) and therefore considered inaccurate in terms of predicting initial rate or even peak maximum derivative/rate[24].

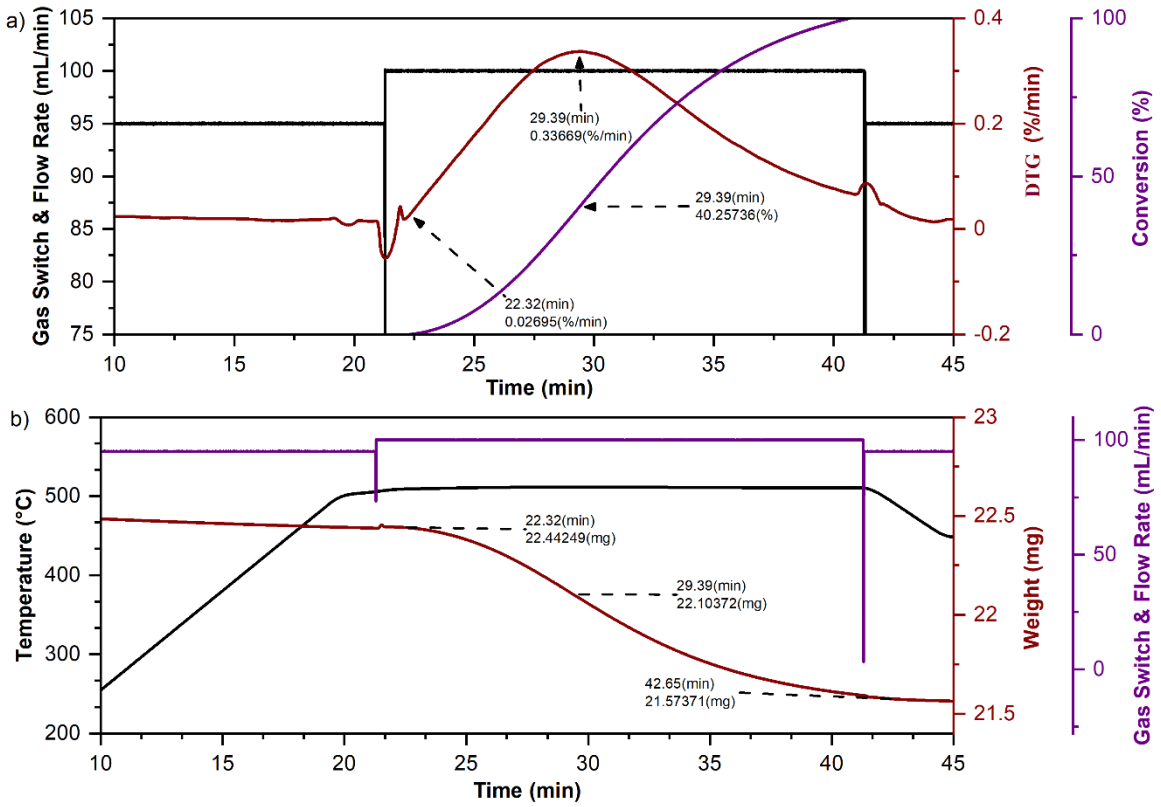

Figure 17. The isothermal experiment at 510 °C which is initiated after the gas flow was switched from an argon source to air. a)The DTG rate of mass loss against time is shown as a brown line. The purple line shows the conversion in graph with a peak DTG measured at 40% conversion. b) Represents the TGA plot of weight loss with time (brown line). Temperature profile and Gas-Switch instances are also depicted in each graph[24].

In contrast, the Ozawa rate constants (K(T)) calculated were as follows : 0.30575%/min for 510°C, 0.54875%/min for 540 °C, 0.7915%/min for 570°C[24]. The prediction that was closest in agreement with the isothermal experiment was the one with temperature of 510 °C[24]. From these observations it is safe to conclude that the kinetic parameter obtained from the Ozawa method are suitable for practical use in predicting maximum rates but restricted within a small temperature region from the onset of oxidation (487 °C -510 °C)[24].

The isothermal experiment at 510 °C is shown in Figure 17, with its maximum peak at 0.33669%/min and has an initial rate of approximately 0.027%/min which was extrapolated at 0.1% conversion from the start of oxidation[24]. The initial rate was not determined by either of the methods employed[24]. These observations have shed some light in the meanings behind these equations, their usefulness and capabilities when used in the context of refractory oxidation profiling[24].

Interesting observations were also noticed when trying to use the Arrhenius equation to predict the rate constants for the MFK models. To get a prediction, activation energy in

the form of joules and Arrhenius constant taken from the MFK as described previously without any assumption applied mathematically (i.e., in attempt to change the value of Arrhenius by converting from per minute to per second or vice versa) was effective. The predicted rate constant values made sense only if interpreted as function of time unit in seconds (i.e., mass loss per second). This was then converted to minutes for comparison with isothermal data. Temperature was also converted to Kelvin during calculations.

In terms of the Arrhenius constant, it is clear from this observation that its accurate prediction relies heavily on the MFK method used (i.e., if model-based method is not employed). The above is also the reason why its units will not be annotated when Arrhenius is referred to in this literature. It will be used in a similar fashion to Ozawa non-conversion method in the subsequent sections with the help of the compensation effect to get better predictors.

4.2 Isoconversion Analysis of Resin Phase

The determination of the activation energy as a function of conversion reveals the complex nature of reaction behaviour[24,26,27]. This section therefore explores how reaction behaviour can be understood from the kinetic data produced and assesses the accuracy or limitations with regards to the model free methods of KAS and OFW methods[24].

Figure 18 a, and Figure 18 b, shows the Arrhenius plots of OFW and KAS methods respectively. The compensation effect was used in order to optimise the values of Arrhenius constant[24]. The kinetic predictions from the KAS method were higher than that of the OFW but their overall trend remained similar (see Figure 18 d). There was a decreasing trend associated with the activation and Arrhenius constant as a function of conversion (see Table 5). It is often understood in simple reactions that a decrease in activation in the case where Arrhenius does not significantly change, amounts to a decrease in rate[24,27]. However, the reaction profile of the DTG showed that there was a steady increase in rate of mass loss, which then reaches its peak at 60% conversion before steadily decreasing. This complex sigmoidal behaviour, therefore, re-enforces the need to analyse the effect of the Arrhenius constant in order to explain reaction behaviour[24,27].

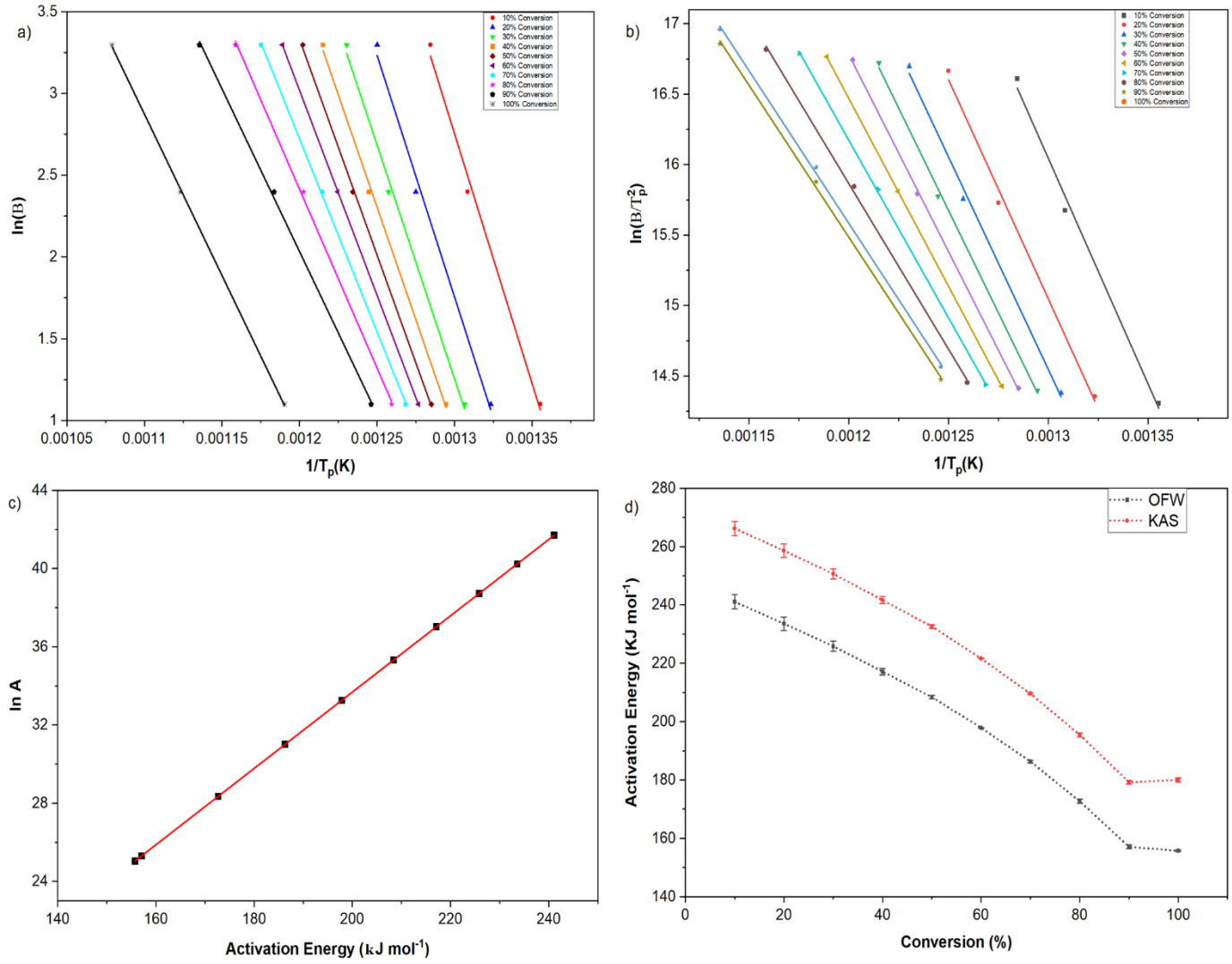

Figure 18. Graphical representation of the Arrhenius plot of a) OFW and b) KAS; linear regression applied on conversion with each slope and intercept producing an activation energy and Arrhenius constant. c) Graphical illustration of compensation effect displaying the linearity between "ln A" and activation energy. d) Shows the activation energy values for both KAS and OFW with respect to conversion (KAS displaying higher kinetic parameters but sharing the same trend)[24]

Table 5. The isoconversion oxidation kinetic predictions of the Ozawa Flynn Method. "*" is indicative of the optimised “ln A" factor through the use of the compensation effect[24].

OZAWA-FLYNN WALL METHOD			
Conversion (%)	**Ea (kJ mol^{-1})**	**R^2**	*** lnA**
10	241.1 ± 2.5	0.98699	52.4 ± 3.3
20	233.6 ± 2.3	0.98804	51.0 ± 2.9
30	225.8 ± 1.8	0.99248	49.4 ± 2.2
40	217.1 ± 1.1	0.99662	47.7 ± 1.4
50	208.4 ± 0.6	0.99902	46.0 ± 0.7
60	197.9 ± 0.1	0.99998	44.0 ± 0.1
70	186.3 ± 0.4	0.99947	41.7 ± 0.5
80	172.7 ± 0.7	0.99782	39.1 ± 0.9
90	157.1 ± 0.6	0.99814	36.0 ± 0.7
100	155.8 ± 0.7	0.99959	35.8 ± 0.3

To analyse the effect of Arrhenius constant, the rate dependency of the activated complex theory approach was used[24,27]. The Arrhenius constant was then associated with entropy to explain the reaction behaviour using a thermodynamic approach[24,27].

From the Gibbs free energy equation, a symbolic representation can be adopted in MFK, utilising, the knowledge of the shift in equilibrium between the reactants and activated complex evaluated as follows according to Vyazovkin[24,27]:

$$\Delta G = \Delta H - T\Delta S \quad [16]$$

Where (ΔG), is referred to the free energy of activated complex formation. The equilibrium is shifted to the formation of activated complex when the entropy (ΔS) increases, lowering the Gibbs free energy (ΔG)[24,27]. It is the “difference in entropy of reactant (S_R) to the entropy of activated complex (S_{AC}) that determines the total change of entropy (ΔS) (represented in Figure 19)[24,27]. To calculate this entropy change (which

will be referred to total entropy or entropy for simplicity) the following equations are provided [24,27]:

$$A = \frac{k_B T}{h} \exp\left(\frac{\Delta S}{R}\right) \quad [17]$$

$$\Delta S = R \ln\left(\frac{Ah}{k_B T}\right) \quad [18]$$

The activated complex theory makes use of a rate dependency relationship similar to that of the Arrhenius rate constant in equation 3., as shown below (i.e., replacement of ΔH with E (activation energy), and taking equation 17 as the Arrhenius constant (A), the rate equation 3 can be derived as a symbolic representation)[24,27].

$$k(T) = \frac{k_B T}{h} \exp\left(\frac{\Delta S}{R}\right) \exp\left(\frac{-\Delta H}{RT}\right) \quad [19]$$

Where, the Boltzmann constant, Planck constant, change in entropy and change in activation enthalpy are represented by k_B, h, ΔS and ΔH respectively[24,27].

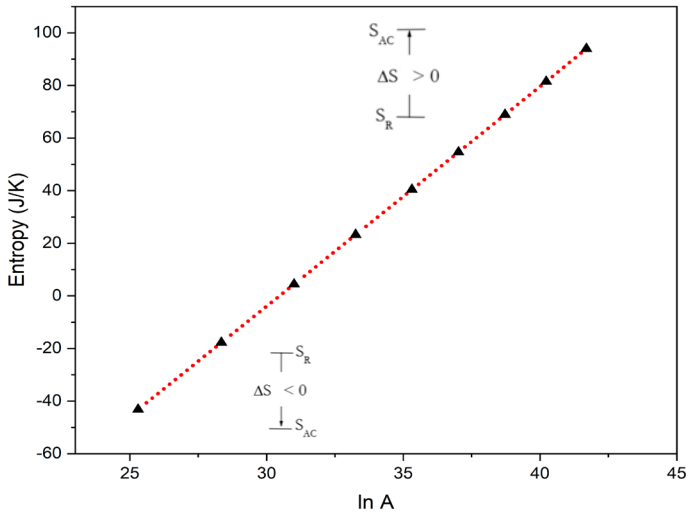

Figure 19 Graph showing the change in entropy change versus the Arrhenius parameter in this case represented as logarithmic value " ln A". Adapted from already publish work to include the thermodynamic descriptors of S_{AC}, S_R, and ΔS, with arrows indicating directional increase or decrease in the gap between S_{AC}, and S_R [24]

By plotting the values of entropy against the values of ln A, a linear relationship was formed as shown in Figure 19. Entropy is highest at the beginning of the oxidation reaction and decreases along the reaction pathway if we refer to concept proposed by Vyazovkin symbolically to assess the frequency factor[24,27]. To understand where this decrease may originate, one must explore what is already known about the microstructure of these type refractories and their behaviour. Around the same temperature where this refractory carbon composite starts to oxides, Luchini et al., highlighted in their study that these were the same initial temperatures (~ 500 °C) where the effects of thermal expansion mismatch on the microstructure were noticeable[24,47]. The effect itself is described as causing pore closure, densification, and a rise in the elastic Young's modulus of the material as temperature was increased[24,47]. The most affected part of the refractory was also discussed. Alumina and graphite were noticeably more influenced by this effect when temperature rose above the critical onset temperature of oxidation[24,47]. Luchini et al., attributed this to the constituents (Alumina and Graphite) having a higher thermal expansion than that of their resin/glassy carbon counterpart[47].

From the above we can therefore deduce that pore closure is a key parameter in controlling the oxidation mechanism[24]. The pore closure in other words would restrict the mobility of the activated complex when entropy decreases as depicted in Figure 19, but with the caveat that this is held to be true only when the entropy change is deemed positive[24,27]. The decrease in the observable total entropy values in the positive region indicates that there is a decrease in gap between activation entropy of reactant and activation entropy of active complex[24,27]. Vyazovkin, describes this to only occur by either increasing the activation entropy of reactants or by the decrease in the activation entropy of activated complex [24,27]. Due to the fact that oxidation is a dissociative process, the latter seems more plausible[24]. It will be expected that gaseous transport into and out of refractory will be impeded. Active sites and surface of resin phase will diminish as the pore closure mechanism increases as a function of temperature[24]. The surface characteristic changes showing reduced surface area of resin and increased presence of graphite due to expansion is shown in Raman image (Figure 39 and Figure 47), in chapter 7 and 8.[24]

As the reaction reaches the end, the entropy takes on negative values. The depletion of reactants at this point will undoubtedly change the orderliness of the reaction interface (i.e., presence of remaining higher molecular weight or more ordered resin structures and

the remaining ordered graphite carbon reaction interface), the expansion of graphite causing further densification subsequently driving the pore closure mechanism all support this associative process toward the end of reaction. The more negative values (bigger numbers) the number is the more resistance to oxidation[24,27]. This was the direction of entropy towards the end of the reaction[24].

Finally, the reliability of the kinetic methods used were assessed by evaluating them against their temperature integral approximation (see Figure 20). The temperature integral approximations are useful to consider when applying these method as they indicate the accuracy of prediction or whether in fact these methods can be used (it is often overlooked in literature)[24,36,39,114].

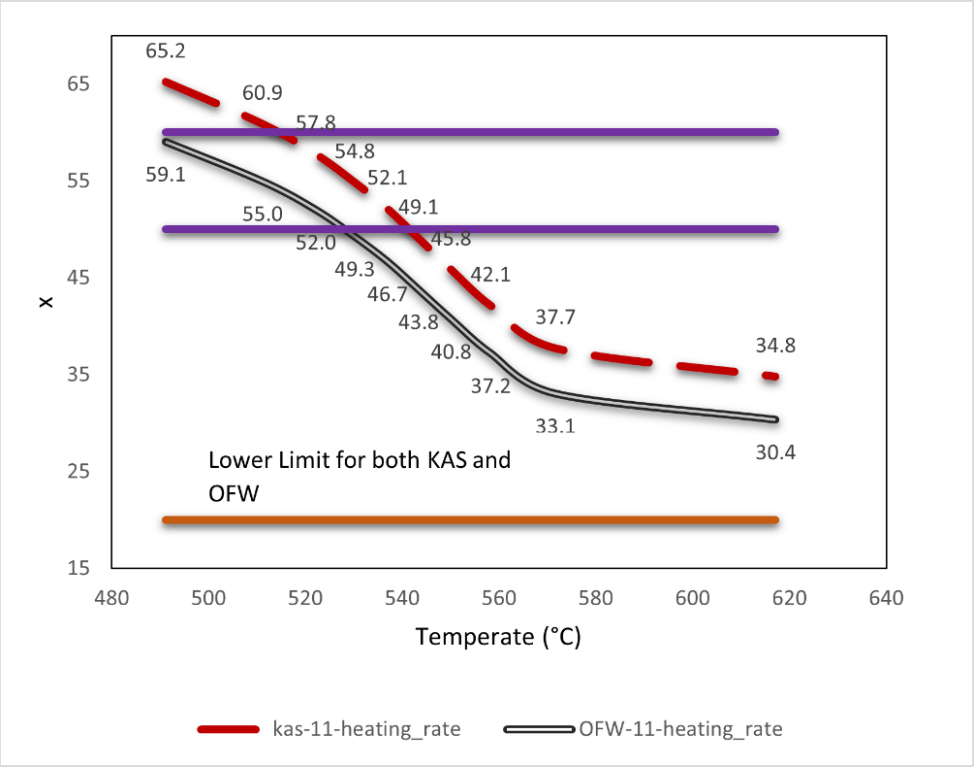

Figure 20. "X" the temperature integral approximation derived from KAS and OFW against the average temperature in each conversion (heating rate of 11 °c/min was used and X=E/RT). The X values of the OFW stayed within its limits of approximation and was therefore considered more accurate than KAS.

Performance of the KAS and OFW method are therefore expected to work best when they stay within their temperature integral limit approximations from which they were derived[24,36,39,114]. For the KAS approach, the limits tested were: $20 < x < 50$ where the $x = E_a/RT$ (where E_a is activation energy per conversion, and T is the average temperature from the isoconversion plot)[24]. And for the OFW method the limits tested were: $20 < x < 60$ where the x is also $= E_a/RT$[24]. The OFW was seen to be more

accurate than KAS especially during the initially stages of reaction and therefore the KAS method was disregarded for further use in this study[24]. All values assessed from the OFW method stayed within the limits discussed above[24].

In summary the reaction complexity can be described by combining kinetics with entropy. This evaluation however requires the use of Arrhenius constant and cannot solely rely on just the change in activation energy values. The OFW isoconversion method is more accurate in terms of its kinetic capabilities than KAS.

4.3 Assessment of isoconversion predictive capabilities and mechanistic association to model-fitting and model-free approaches

To assess the effectiveness of using model free approaches in predicting isothermal reactions from non-isothermal isoconversion data, the Friedmann approach of equation 20, was explored. The Friedmann equation below can be used to determine the time taken to reach a set conversion (with, t = time taken, T= temperature, α = conversion, f(α) is the reaction model)[130]:

$$t_\alpha = \int_0^t dt = \int_0^\alpha \left[\frac{d\alpha}{A_\alpha \, f(\alpha) \exp\left(\frac{-E}{RT_\alpha(t)}\right)} \right] \qquad [20]$$

Evaluation of this equation with kinetic inputs from the OFW method was inadequate in terms of accuracy in predicting comparable values to the isothermal experimental data (510 °C 540 °C 570 °C)[24]. The inaccuracy can also be compounded by the fact that the reaction mechanism under investigation is quite complex (in the non-isothermal approach)[24].

To overcome this issue a better integral method known as the Vyazovkin method was instead utilised for predicting more accurate values of activation energy (Table 6).These values were derived from a freely available kinetic software program[116]. It was then possible use the values of “a” and “b” from the compensation effect of OFW. However, a systemic error is carried over from OFW method by utilising the compensation effect constants of “a” and “b” in this manner[30].

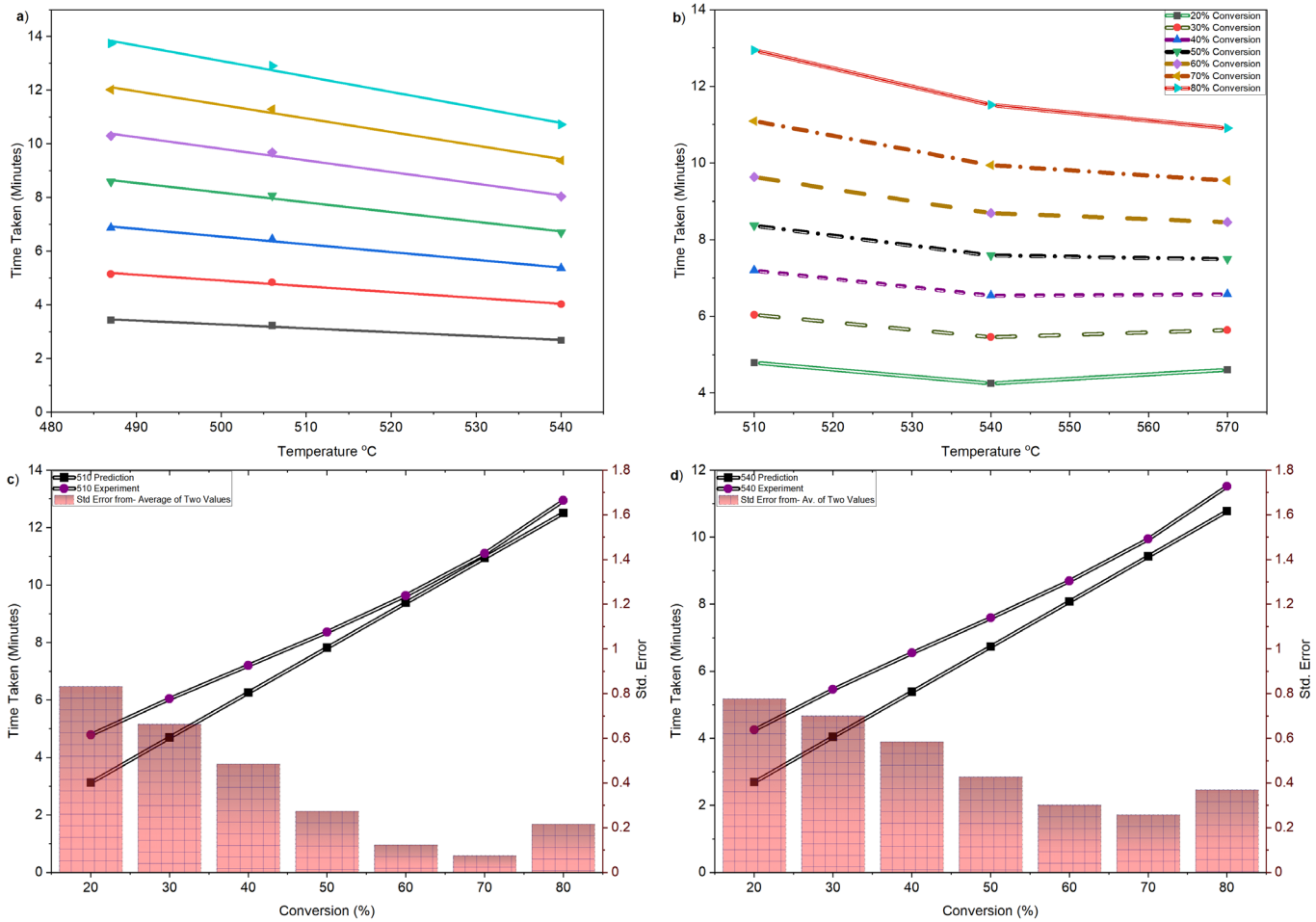

Figure 21. a) Time taken to reach a set conversion point versus temperature (model generated for predicting isothermal experiments). b) Isothermal experimental data at 510 °C, 540 °C, and 570 °C for the time taken vs temperature. c) Theoretical prediction for 510 °C compared with experimental data. d) Theoretical prediction for 540 °C compared with experimental data. Standard error is used to assess the difference between theoretical and actual experimental values[24].

Table 6. Shows the Vyazovkin activation energy values with respect to conversion that served as inputs for calculation improvement in this section

Conversion (%)	Activation Energy (kJ/mol)
20	226.7822
30	218.8131
40	209.81461
50	199.02974
60	185.8929
70	169.8032
80	150.4979

An extra step was then taken to modify the way in which the method of Friedman is used. A carefully selected combinations of kinetic parameters served as inputs for activation energy, Arrhenius constants alongside a set of selected temperatures[24]. These kinetic combinations with their associated temperatures produced a linear graphical trend with the same R^2 values (0.983 see Figure 21 a)[24]. The equation that emerged from the linear regression analysis was then used as the basis for calculating the time taken variable which is novel approach itself[24].

Three inputs of activation energy and Arrhenius constant were taken from the following conversions: 60% (peak maximum), 70% and 80%. Aside from the peak maximum conversion, it was realised that the selected conversions that worked in this manner happen to fall within the regions of the latter stage of the non-isothermal reaction[24].

Three subsequent temperatures were selected from the non-isothermal reaction consistent with 10%conversion (487 °C), 20% conversion (506 °C), and the peak maximum at 60% conversion (540 °C). These temperatures were then associated with the kinetic parameters from the order of the lowest to highest, i.e., 487 °C was coupled with kinetic parameters obtained at 60% conversion, 506 °C was associated with kinetic parameters obtained at 70% conversion and lastly, 540 °C was associated to the kinetic parameters obtained at 80% conversion[24]. Any other combination failed to meet this high linearity of coefficient alluded to previously[24]. It was also observable that the first two choices of temperature are taken from the beginning stage of the reaction, this is in contrast to the way the kinetic parameters were selected. Finally, the reaction model f(α) was kept the same for all three calculations and selected at 20% conversion[24]. The reaction model of f(α) was calculated in a model free approach as depicted below (Equation 21)[24,26]:

$$f(\alpha) = \frac{d\alpha/dt}{A_\alpha \exp\left(\frac{-E_\alpha}{RT}\right)} \quad [21]$$

The theoretical predictions suggest that the time taken reduced as temperature increased for each respective conversion[24]. However, when compared against the experimental isothermal data, a subtle difference was uncovered. From the experimental data, the trend of reduction in time, as a function of temperature increase, still holds true for all tested temperature with a slight exceptional case for the temperature at 570 °C[24]. The trend at

this temperature increased but only for conversion less than 50% (see Figure 21 b). The remaining conversion followed the same reduction in time as observed with the theoretical predictions and lower tested temperatures[24].

This anomaly also shed light into the pore closure mechanism since the decreasing trend/slope steepness of the time taken above 50% was lesser, when compared to the previous temperatures (see Figure 21 b). When the overall behaviour is considered (i.e., increase in time and only marginal decrease), this may suggest that at higher temperatures the slight delays in reaction time is as a result of the pore closure mechanism having a greater effect at higher temperatures[24].

Perhaps the use of the Friedman approach in obtaining the kinetic parameter might be an alternative option (although regarded as more accurate often suffers from poor analytical output data that requires pre-processing which can introduce more errors), however the use of single activation energy to predict extends of conversion or time taken to reach it, is feasible, but should be verified against a broad range of temperatures to find its limits.

The isothermal prediction accuracy was highly dependent on both conversion and temperature (see Figure 21 a, and b)[24]. It is safe to extrapolate from the empirically modified approach that the predictions would work best at lower temperatures[24]. To test this hypothesis, a baseline standard error of < 0.5 was set, to investigate the prediction capabilities with respect to 510°C, 540°C and 570°C; by comparing the theoretical predictions from the modified empirical approach versus the actual isothermal experimental data (see Figure 21 c, and d)[24]. 510°C performed the best when used in the modified model and gave a good prediction between 40% to 80% conversion (see Figure 21 c). 540 °C gave good predictions from 50% to 80% conversion (see Figure 21 d), however, 570 °C could not be used due to margins of error being greater than the baseline that was set[24].

Results obtained from the kinetic isoconversion study of the resin were also assessed against common solid-state kinetic models using $Z(\alpha)$ master plot (see Figure 22)[24]. There were no overall fit for the models tested. However, the experimental curve seems to follow a mixture of Avarami and exponential/power law in terms of trend/shape[24]. The experimental curve never quite fit any of the models and varied largely as a function of conversion[24]. It was observed that at lower conversions of 20% and below, a reasonable relationship can be drawn with certain models in terms of proximity[24]. Assessment of the 10% conversion cross point indicated that the avarami models of A4 and A3 and the power law of P4 were in better agreement with experimental curve[24]. F3 (third order) and A4

model exhibited better the agreement at 20% conversion[24]. The agreement at these lower conversions could mean model fitting approaches may be suitable for predicting kinetic parameters but only at lower temperatures for the complex reaction under investigation[24].

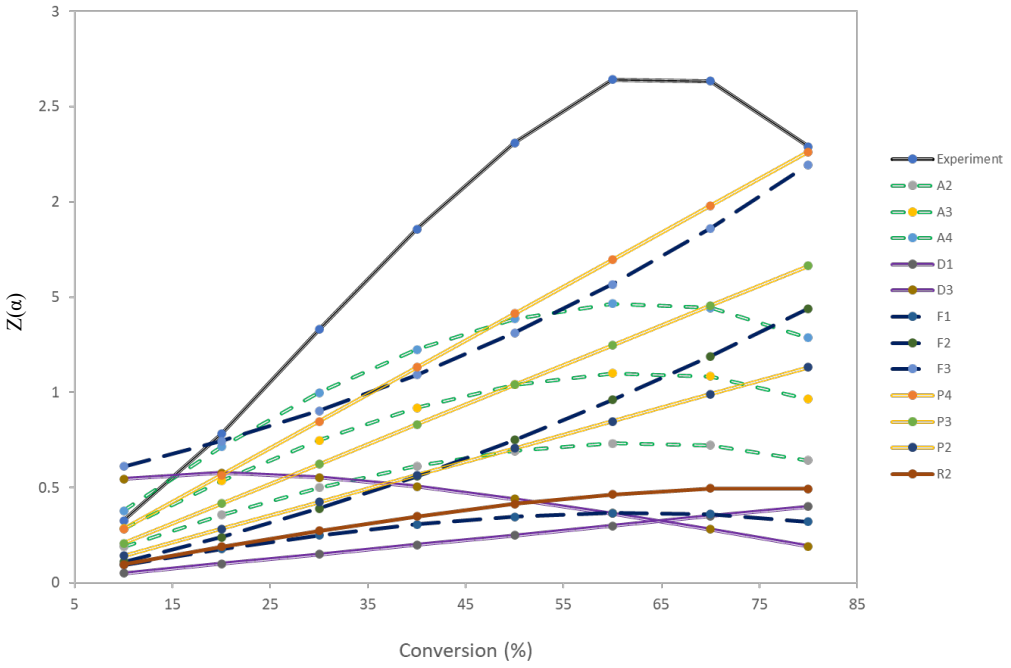

Figure 22. Z(α) master plot of common solid-state theoretical models compared against experimental plot. Z(α) theoretical output was calculated by multiplying the differential with the integral forms of reaction mechanism equations below. Experimental values were determined using dα/dt (3°C/min) in the equation: Z(α) =(dα/dt) T2. [π(x)/βT][30]; where π(x) can be determined by the fourth rationale of the Senum-Yang approximation[116]

This observation clearly shows that model-fitting approaches although useful may not necessarily be needed in terms of the practical application that is sought after in this industrial context. The rapid characterisation, predictive capabilities, profiling reaction mechanism presented by model-free therefore makes the use of model-fitting trivial and not necessary in this case[24,26]. Furthermore, there are other simple methods that can be used to know whether a reaction follows a particular trend. For instance, one can use an isothermal experiment in deciphering various common-solid state mechanism if the following was met:

a) If the reaction reaches the maximum rate as soon the isothermal temperature tested was reached, then this would be regarded as a deceleratory model[30].
b) If the reaction is not the above case, then it falls within the sigmoidal models or acceleratory models. If the reaction does not peak and carries on to the

end then an acceleratory model such as the power/law model can be used, otherwise if it peaks and drops the sigmoidal model will be more appropriate[30].

There are other methods which involve plot of ln(dα/dt) against time, and the shape obtain from this isothermal data can be used to determine whether a reaction is first order, contracting volume or even increasing diffusion[30]. Finally, it is important to understand that the reaction itself may have its own unique model not described by the common solid-state models which can also be derived by way model free[26,30,116].

In summary, the results obtained from the predictions proves the extent at which these isoconversion methods can be used. From a simple non- isothermal experiment, one can predict isothermal data. Reaction mechanism can be inferred does not always have to match known kinetic models as the reaction itself has its own unique path and not always required for explaining reaction behaviour.

4.3 Isoconversion Analysis of Graphite Phase

The previous sections have mainly focused on deriving meaning behind reactions and ways to utilise various model-free kinetic models, specifically the integral models in obtaining isoconversion kinetic parameters. In this section, the graphite oxidation phase will be analysed using an additional method that is based on a differential method known as the Friedman method[29,39]. The differential method is supposedly more accurate than its integral counterparts but is often limited by the quality of data output produced from thermo-analytical instrument[29,30,39]. Smoothing or pre-processing of the derivative noisy data can introduce faults and errors into calculation which is why the integral methods are often preferred[29,30]. It is important to note that in terms of kinetic prediction capabilities, the Vyazovkin is an exception to this and performs better than the differential form of Friedmann[29,30].

Guo et al., compared the Friedmann differential method with KAS and OFW integral methods whilst investigating the oxidation of graphite and found it to be more accurate[39]. It is therefore crucial to know whether this will also be the case for a carbon refractory composite. In an industrial context it may be more suited to use a single model for kinetic profiling rather than multiple. This therefore necessitates the understanding of whether the integral form of OFW can still give equivalent predictions as their thermo-analytical data (i.e., integral form) is deemed more reliable [29,30].

From the SDT analysis, the graphite oxidation initiates at temperatures above 600 °C. There is an observable shift in the onset of oxidation as a function of heating rate similar to

what was observed and discussed in the previous sections regarding the resin phase. A clear difference between the peak derivatives of mass loss to resin was noticed. A decrease was observed with regards to the resin phase as a function of heating rate (using temperature derivative of percentage weight change/units referenced) depicted in Figure 23. In contrast to graphite, where there was a marginal increase of the peak (DTG) as a function of heating rate from 3 °C/min to 11 °C/min, however there was not much of a change in the DTG peak between 11 °C/min to 27 °C/min.

Guo et al., describes the temperature regions of graphite oxidation in three: a) a region 400-600 °C is regarded as the chemical reaction dominated region, b) the in-pore diffusion control region was from 600-800 °C and lastly the boundary layer contribution regime was at temperatures above 800 °C[39]. In summation, it is the combined nature of chemical reactivity and diffusion driving the reaction[11,39]. With an increased temperature it is expected that the chemical rate increases, however this will be restricted by gaseous product layer formation [11,39]. Therefore, the positive shift observed with the DTG may appear as a marginal increase in rate, but its feature is indicative of both of these effects.

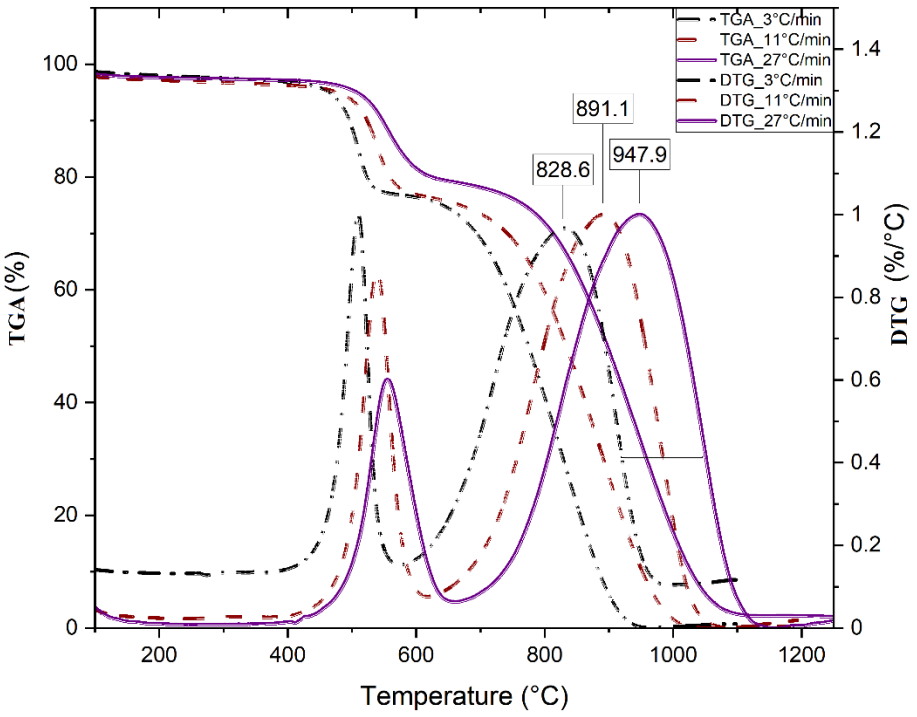

Figure 23. A graphical representation showing the oxidation of both resin and graphite oxidation as a function of temperature increase. The graphite maximum DTG peak temperature are highlighted for reference.

Perhaps the best way to show the effect of temperature increase in this situation is to utilise the time derivative of percentage weight change of the DTG instead (see Figure 24). The

rapid heating delays the onset of oxidation and therefore preserves the amount of surface area available for chemical reaction to occur (with expanding graphite)[46,47], and at higher temperatures. Once oxidation occurs (at the initial stages), it subsequently increases the reactive surface area and thereby increasing the effect of oxidation itself[39]. The DTG plot shows this behaviour (temperature effect) with a rapid increase in chemical reactivity for sample heated at 27 °C/min (see Figure 24).

The slower heating rate exemplifies the in-pore diffusion properties more readily. Oxidation will also increase at the beginning stage of the reaction as a function of temperature, but as the reaction progresses to higher temperature their surfaces will be cover with stagnant gas layer comprised of reaction products and air[39]. The oxygen required to react with the carbon therefore must diffuse through this layer and the pore structure in order to react with the carbon[39].

And towards the end of the reaction there is a reduction in surface area available for reaction to occur [11,39]. The dominant mechanism at that temperature will also be factor in modulating reaction, hence a rapid a decrease in rate is expected [11,39].

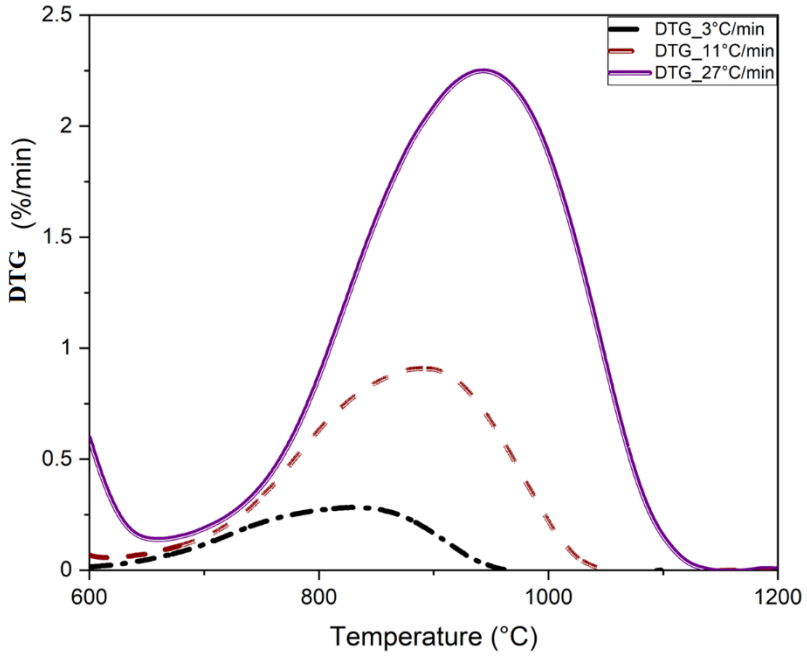

Figure 24. DTG time derivative of percentage weigh change as function temperature increase during oxidation (%/min) of graphite showing the effect of heating rate on the mechanisms influencing oxidation.

The isoconversion methods of Friedmann, OFW and Vyazovkin were used to gain more insight into the reaction properties by looking at the changes of activation energy and Arrhenius constant with respect to conversion and temperature. The plot of Friedmann was

simply achieved by plotting the logarithmic rate ln(dα/dt) versus the 1/ T_p (which is a temperature of the associated heating rate i, and conversion in their respective equations); for the OFW the ln(β) versus the $1/T_p$ were used, where β refers to the heating rate (Figure 25). Their Arrhenius plots are depicted with high correlation coefficients.

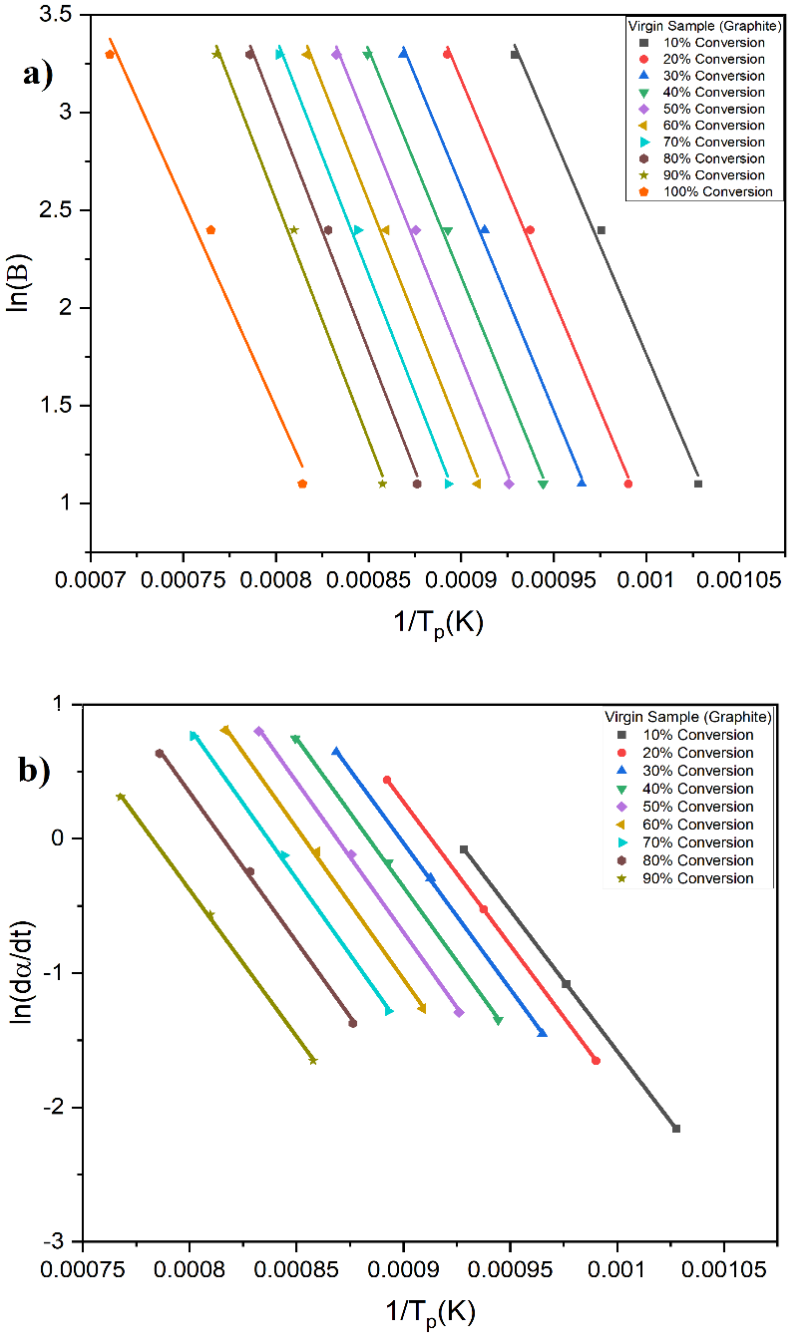

Figure 25. The Arrhenius isoconversion plot of a) OFW method and b) the Friedmann method used for profiling the oxidation behaviour of in the graphite phase of a virgin sample.

All of the methods employed seem to agree with respect to activation energy that there is a gradual increase in their trend. This is at least true to 70% conversion where a slight decrease was noticed only with the OFW method (refer to Figure 26). The OFW method also predicted similar values of activation energy to that of Friedmann suggesting that it can be used to determine kinetic parameters with respect to the composite under investigation. The OFW and Vyazovkin do share a similar shape/or curve in terms of activation energy. And at the latter stages of the reaction the Vyazovkin seems to suggest that the activation energy plateaus rather than increasing when compared against the Friedmann method (Figure 26).

Since all of their respective Arrhenius constants tend to decrease as a function of conversion (only marginal increase was observed with Friedmann between 20% to 30% conversion: ln A 19.50925 to ln A 19.5656), it can be inferred that the reaction intensity reduces slightly as a function of temperature increase based on the previous mechanisms described above (gases layer and diffusion). The evaluation of entropy values of ln-A may not be necessary in this case.

The Vyazovkin method being the most accurate can be used solely to describe the reaction behaviour in this instance. In terms of Arrhenius constant predictions, the Friedmann method seemed to have lower values than OFW making it more accurate (that if we used Vyazovkin method as a reference point of accuracy). The values produced from the Friedmann approach, however, does not follow the compensation effect linearity that was observed with the OFW and Vyazovkin method. A plot of the ln A against activation energy does not produce a linear regression with regards to the Friedmann approach.

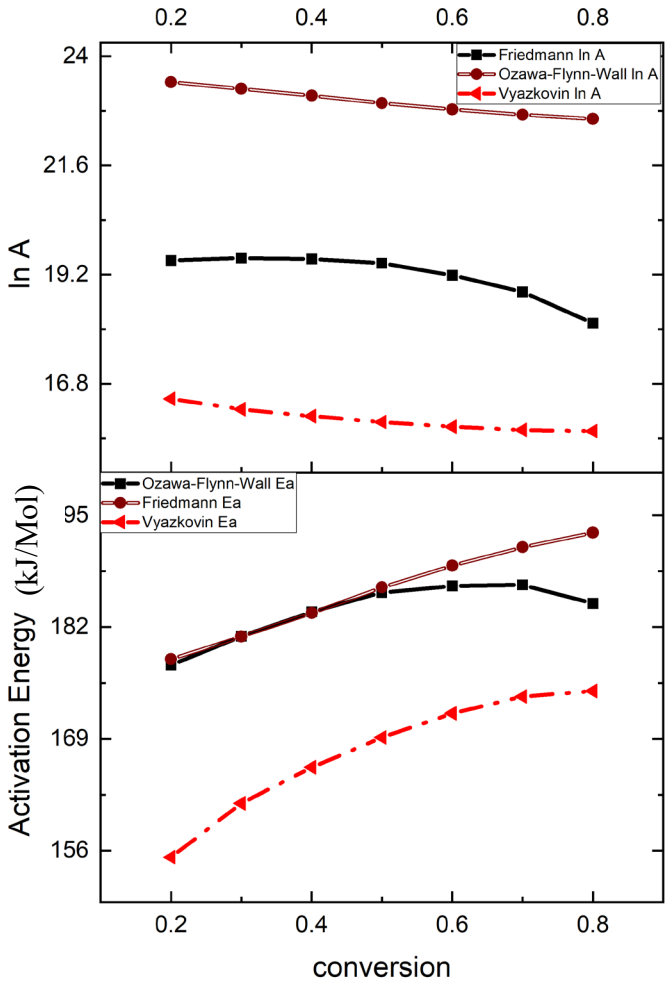

Figure 26. Graph of activation energy and ln A for various model free-kinetic models: Friedmann, OFW and Vyazovkin. Each models shows their predictive capability in analysing the graphite phase in a virgin refractory sample.

For the final analysis of this work the kinetic software that was utilised to obtain the activation energy of Vyazovkin was also used to derive the kinetic triplet at 50% conversion[116]. This allows for the determination of a unique theoretical mechanism that can used to predict the experimental data[116]. This can be achieved using Sestak and Berggren model by inputting the values of m, n and p from the software to obtain the model (equation 22)[116]. The Sestak and Berggren empirical model is often used to derived many of known solid state-kinetic models that exist[30,116]:

$$f(\alpha) = \alpha^m(1-\alpha)^n[-\ln(1-\alpha)]^p \qquad [22]$$

The predicted values of m, n, and p were 0.1, 1.08 and 0 respectively. The Arrhenius constant predicted at 50% conversion was $8.53x10^6$ (ln A = 15.9591) with the activation energy value of 167.69 kJ/Mol. The 3 °C/min heating rate adapted by the software was used in the theoretical calculation. From these number we can therefore describe the reaction using the following (equation 24):

$$\frac{d\alpha}{dT} = \frac{8.53x10^6}{3} . e^{\left(\frac{167.69\ x\ 10^3}{R.T}\right)} . \alpha^{0.1} (1-\alpha)^{1.08}$$

[24]

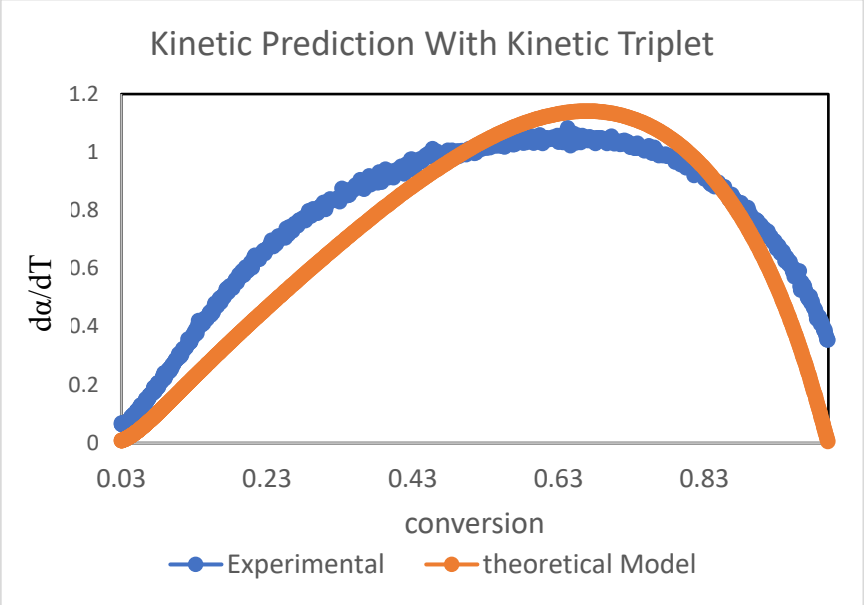

Figure 27. The use of kinetic triplet to predict experimental data with the use of Vyazovkin kinetic parameters.

The two curves in Figure 27, shows the plot of experimental data compared to the predicted curve derived from the empirical equation describing the reaction. The software can also predict OFW activation energy values and uses it to calculate the relative error against the Vyazovkin's activation energy at 50% conversion[116]. It is mentioned that if the error obtained is greater than 10% then one can consider the reaction to be multistep[116].

We can therefore conclude that the reaction mechanism can easily be understood, profiled, and predicted using model-free approach of Vyazovkin without issues encountered in

previous chapters. The need for a kinetic triplet (activation energy, Arrhenius constant, and reaction mechanism) prediction is also satisfied if required.

Chapter 5-Influence of preheat on oxidation kinetic profiling

5.1 Isoconversion Preheat Analysis of Resin Phase

Industrially preheated SENs were provided by sponsor company to evaluate whether their heating practices contribute to a kinetic profile change that can significantly impact the performance of their SEN. The preheating regime can last from 1 hour to 6 hours [17,18]. After preheating the SEN, it is then expected to be used in service for various heats (approximately 4 hours)[84,85]. It is crucial to know whether there will be significant changes when heated (correctly), as this can inform whether time should be reduced, kept the same or increased (or bring about new solutions/strategies). Since a lot of waste is attributed to unused preheated SENs in practice, and it is of value knowing whether their oxidation profiles (resistance) differ during the preheating regime[17].

Based on the fact the Vyazovkin method is far more superior and accurate in its prediction as discussed in the previous chapters, it will be the main method used for this analysis. From the activation energy values obtained in Figure 28, it is clear there is a major difference in prediction from the virgin SEN sample (0 hour) compared to the preheated sample group (3 hour preheated and 6 hours preheated). Higher activation energy values were obtained for the virgin SEN. The same can be said about the Arrhenius constant of the virgin SEN in terms of having much higher values reported (see Figure 33). The higher activation energy values may suggest better resistance to oxidation; however, this is overshadowed by the influence of the Arrhenius constant being too high in contrast with the preheated group. As a result, it is expected that the resin phase of the virgin material will oxidise at a much faster rate than the preheated samples.

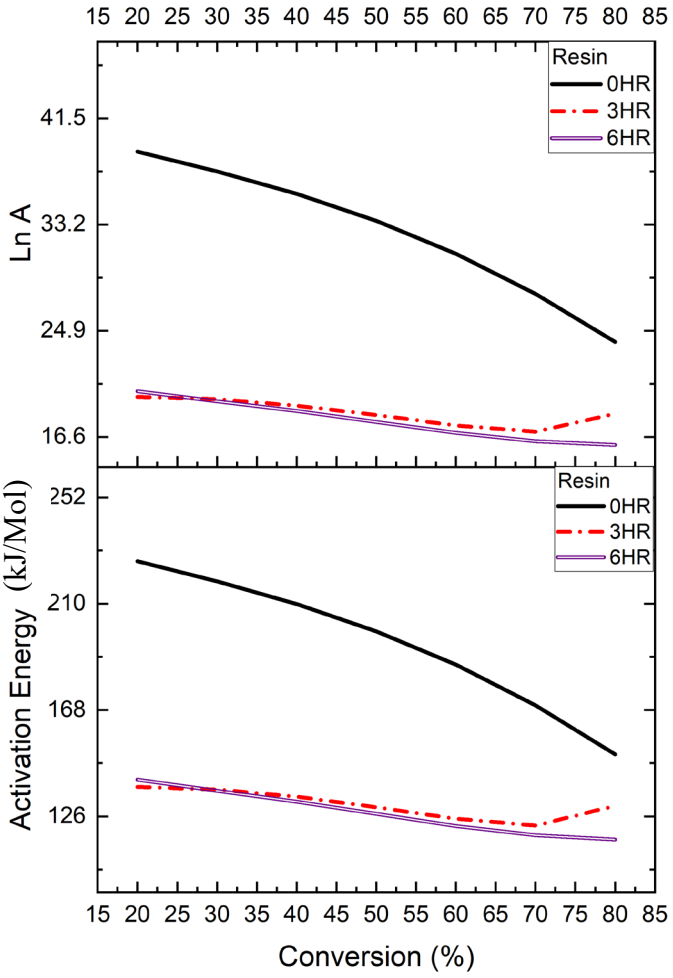

Figure 28. A graph showing the Vyazovkin kinetic parameters of activation energy and Arrhenius constant for a virgin SEN, 3-hour preheated, and 6-hour preheated when analysing the resin phase of a carbon-bonded refractory composite

Since the entropy behaviour of the virgin SEN has both positive and negative values, and the preheated SENs only possess negative values; we can compare them at the conversions where their negative values coincide in order to obtain a fair understanding on the deductive reasoning applied above. At 0.5 conversion the preheated SENs has values of: -101.07 and -105.59 for the 3-hour and 6-hour sample respectively. The virgin SEN has a value of -6.98 (small negative value) which is regarded as having higher/or is larger total entropy value (see Table 7). Due to this higher entropy value, we can safely conclude that the virgin SEN will react much faster than the preheated at or above conversion mentioned and its corresponding temperatures. This would also suggest the presence of microstructural influences causing the reduction of Arrhenius constant dramatically with regards to the preheated SEN given them an advantage of oxidation with regards to the preferential oxidation of the resin.

Table 7. Kinetic and thermodynamic parameter obtained from Vyazovkin method. An improvement was applied to the values a and b of the compensation effect by using the predicted Arrhenius constant from the kinetic software that allow for a better prediction of entropy compared to the earlier report values using OFW compensation effect values of a and b.

conversion	*Ea Vyzk (kJmol^{-1}).*	*Ln A*	*T(Kelvin)*	*Entropy (J/K)*
0.2	226.78	34.40	779.95	33.10
0.3	218.81	33.02	791.161	21.55
0.4	209.81	31.47	799.57	8.56
0.5	199.029	29.61	806.73	-6.98
0.6	185.89	27.34	813.58	-25.89
0.7	169.80	24.56	820.83	-49.04
0.8	150.497	21.23	829.53	-76.821

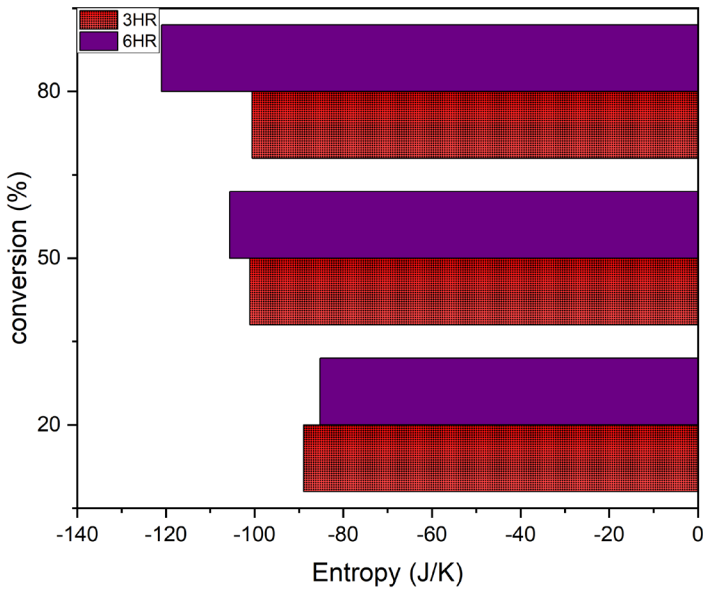

Figure 29. Entropy (change) evaluation of preheated samples (3-hour vs 6-Hour preheated): Analysis of the resin phase applied for the resin phase only.

Without the entropy evaluation, it is quite difficult to uncover what the true difference is between the 3-hour heated versus the 6-hour preheated due to their closeness in prediction for both kinetic parameters. Overall, they both share a similar trend and thus should have similar microstructures. The values of activation energy are slightly higher for the most part with regards to the 3-hour preheated sample, the effect of which is dampened by also having a slightly higher Arrhenius constant overall. Evaluation of the entropy values shown in Figure 29, gives a better insight. At 0.2 conversion (20%), the 6-hour preheated sample has a smaller negative value meaning it has a larger total entropy therefore making it more reactive and less resistance to oxidation compared to the 3-hour preheated sample. At 0.5 and 0.8 conversion the situation changes and its now the 3-hour sample that has the smaller negative value in contrast to the 6-hour. Consequently, this makes the 6-hour sample more resistance to oxidation. Since the kinetic parameter that decides the reaction mechanism of Vyazovkin is determined at 0.5 conversion, the theoretical obtained would describe the 6-hour preheated SEN as more resistance to oxidation. This at least true for moderate to high temperature where the resin phase oxides.

5.2 Isoconversion Preheat Analysis of Graphite Phase

The graphite region of oxidation perhaps holds a greater significance in terms of preheating practises and temperatures that SEN frequently experiences. As well as under heating of the SEN due to burner misalignment, cooling is also likely to occur at temperatures just below 800 °C during off-gas time (i.e., time between SEN taken away from flare until it is in direct contact with molten steel) which is highly undesirable[2,17,52]. Lack of effective heating to activate the glass coating at the required temperature during prolong heating periods can also increase the risk to oxidation which can happen at temperature just slightly above the 800 °C but less than the temperature required to densify the glass coating[1,2,17]. The profiling of the graphite phase as a function of conversion can therefore provide behavioural insight that may help improve how the material is treated[24].

The Vyazovkin approach was used in deriving the kinetic parameter as a function of conversion. A clearly distinguishable trend was observed from the SENs that were heated in comparison to the virgin material. The SENs that were preheated shared the same trend for both their activation energy and Arrhenius constant values which suggest that may share a similar microstructure. The activation energies of the 3-hour preheated sample was higher than the 6-hour preheated sample, however this effect is dampened by the fact that the 3-hour preheated SENs also had higher Arrhenius constant values (see Figure 30). The

activation energies of the preheated SEN tend to decrease at the beginning stages of the reaction coupled with a decrease of Arrhenius constant, all the way to about 50% conversion. Beyond this point the kinetic parameter tend to plateau as if in steady state (which can be observed in diffusion dominated mechanisms[39]). After 70% conversion there is a noticeable increase in both kinetic parameters of the preheated.

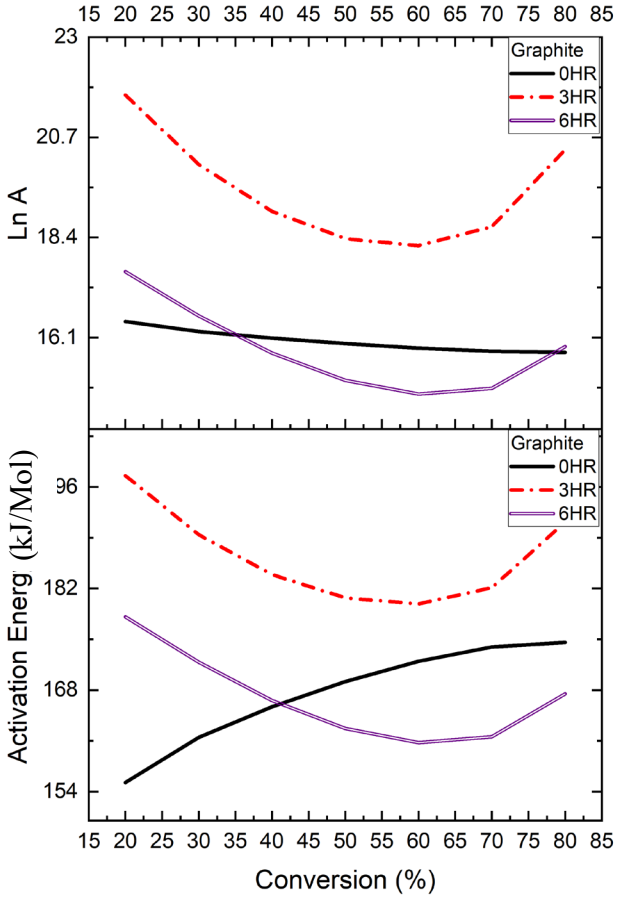

Figure 30. A graph showing the Vyazovkin kinetic parameters of activation energy and Arrhenius constant for a virgin SEN, 3-hour preheated, and 6-hour preheated when analysing the graphite phase of a carbon -refractory composite

The profile of the virgin SEN is differing greatly in graphical pattern observed. The activation energies of the virgin sample behave opposite in trend compared to its Arrhenius counterpart (i.e., in contrast to the preheated SENs). The activation energy increases as a function of conversion whereas the Arrhenius constant decreases. However, the decrease of the virgin sample's Arrhenius is only marginal and may not be regarded as significant compared to those observed with the preheated samples. Another interesting analysis to note is that the Arrhenius constant values of the virgin sample is closer to those observed in

the 6-hour pre-heated sample. To truly understand the overall effect of these parameters an entropy analysis was undertaken to evaluate their resistance to oxidation.

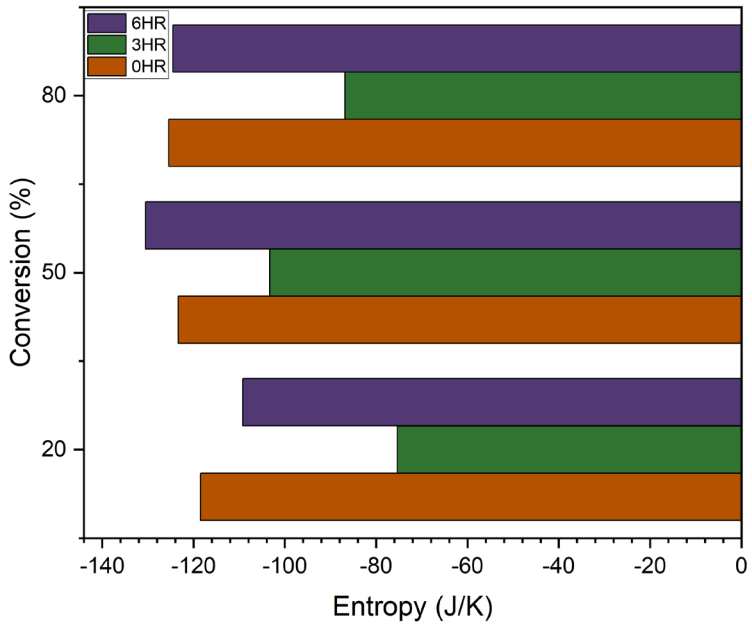

Figure 31. Entropy (change) evaluation of virgin SEN sample, and preheated samples:3-hour and 6-Hour. The analysis comprises of the graphite phase only. Entropy is used symbolically to assess the magnitude difference between SENs

Starting with the comparison between virgin and the preheated group, at 20% conversion the virgin sample had a bigger negative number which translate to lower total entropy. This would make it more resistance to oxidation than the preheated SENs at this conversion and its corresponding average temperatures (803.67 °C ± 2.92). At the 50% conversion it is observed that the virgin sample is only more resistant to oxidation than the 3-hour preheated sample, with respect to their corresponding temperatures (879.50 °C ± 3.28). And for the last assessed conversion of 80% the same trend is observed as previous and with respect to their associated temperatures (949.46 °C ± 5.94).

When comparing between the preheated SEN samples, the more resistant to oxidation is the 6-hour preheated SEN at all conversions. It is only outperformed by the virgin SEN at 20% conversion or corresponding temperatures.

In terms of resistance preheating at the correct temperature may actually improve the microstructure at certain temperatures and thus improves its oxidation resistance. Longer preheating therefore may pose a risk to oxidation only if the glass coating densification

was not achieved by rapid heating that is required. The virgin sample is seemingly also more resistance to oxidation than a SEN that was preheated for short period of time.

Chapter 6-Raman Oxidation Tracking and Assessment of Preheated SENs

The ability to use Raman in synergy with the Model-free approach brings together two simple yet sophisticated techniques that bring with them a wealth of information[24]. Raman has recently been adopted to study SEN inclusions that causes clogging and negatively impacts the steel quality and output[86]. If Raman can also be adopted in the study of oxidation behaviour and mechanical implication of the SEN, then it will be a versatile tool worth adopting in an industrial context for assessing SEN's integrity. Raman is known to be effective at deciphering the order of carbons, the defect types that are present, calculation of crystallite size, stress and strain effects and oxidation[24,45,51,94,104].

To investigate the tracking ability of Raman on oxidation of carbon-bonded refractory, four samples were oxidised incrementally at 1, 2, 3, and 4-minutes duration using the SDT. The isothermal temperature was set to 510 °C to preferentially oxidise the resin. The sample remained in bulk state to preserve the microstructure for both Raman analysis and further analysis using μ-CT tomography.

The WiTec software used in this study has an in-built cluster analysis algorithm that allows one to automatically set the number of clusters for the program to learn and distinguish features based on similarities of features on thousands of automatically scanned Raman data points from a map[24,25]. The software was therefore used in this study as an advanced technique to distinguish between the carbon types present and those carbons whose signals were affected by substrates (i.e., specific compositions or elements) present within the refractory[24].

An automatic depth scan map was selected to scan a region of interest from each oxidised sample. These map scans would generate 40000 data points with each scan point representing an image pixel(see Figure 32)[24]. After conducting the map scan, the clustering algorithm made it possible to locate the graphite rich regions (co-existing with resin) and resin rich regions (co-existing with graphite) based on features of similarity [24]. Each map of an oxidised sample area was then divided into 4 clusters. The clusters that were the least affected by substrate effects was then used to determine the oxidation

relationship with respect to their Raman signals after the software averages them into one Raman spectrum. The same step was applied across each sample.

Determining which cluster to use and number requires knowing what constitutes to bad signal or interference i.e., fluorescence effect or Raman signal with raised background coupled with noisy data and at times a sharp reduction in a Raman feature with noisy data or its sudden amplification[24,89]. Cascading between different graphical representation can help visualise these effects as shown in Figure 33.

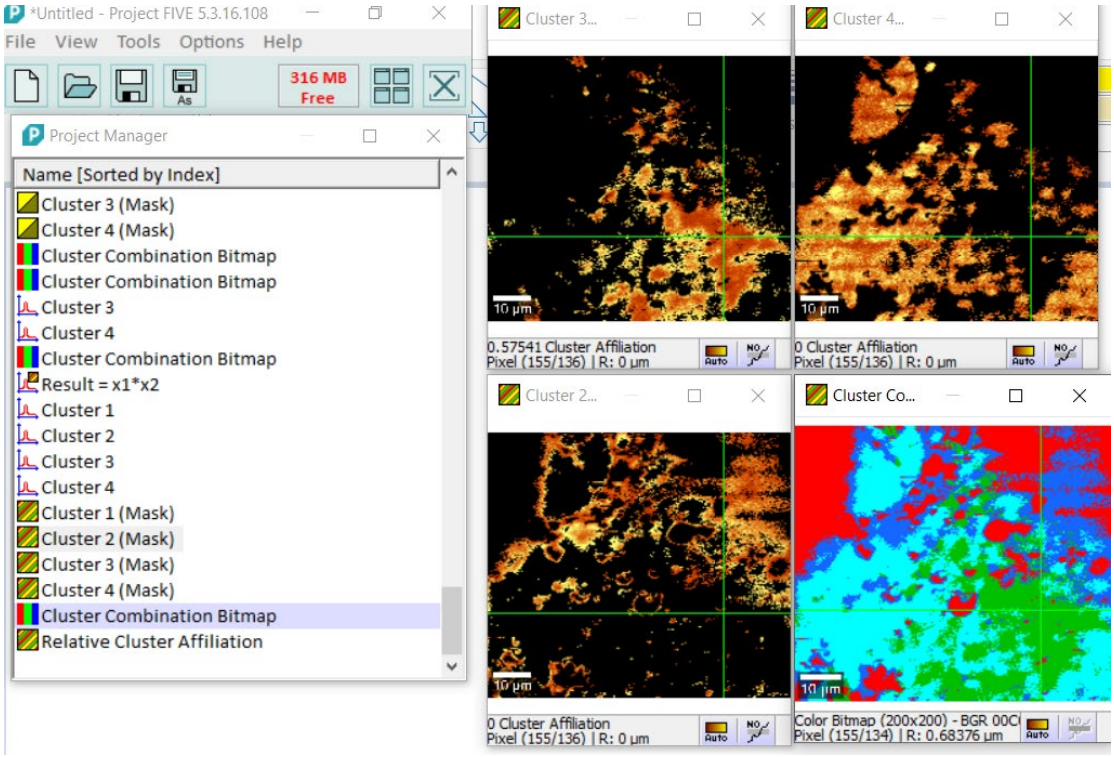

Figure 32. WiTec cluster analysis map output data, with location tracking of different carbon regions in a sample comprising of 40,000 data points. Automatic colour assignment is given unless changed manually when cluster technique is applied to show grouping of similar clusters shown. The green colour selected is a single Raman spectrum of carbon belonging or affiliated to cluster 3 averaged map of all cluster within the selected group. The green represents 1 out of 4 cluster that can be represented graphical form shown in Figure 33.

To analyse the data a single Lorentzian fitting to the G and D peaks of the elected clusters were obtain (to get information in terms of width, height and errors associated)[24,93]. The single deconvolution method is simply a recommendation taken from Mallet-Ladeira et al., in their study to improve how to determine crystallite size of carbon materials using Raman [24,93]. The main measurements of interest to which a correlation can be determined was the ratio of the intensity peaks of D to G (I_D/I_G ratio) and the crystallite size of the carbons derived from the width of their G-peak [24,93,131]. To determine crystallite size of the

resin region/cluster a method proposed by P. Mallet-Ladeira et al., was used[93]. However, for graphite a different method was used that was proposed by Maslova et al[51]. The choices of which to method to use was presumed based on the expected sizes of each carbon type in literature[51,93,131].

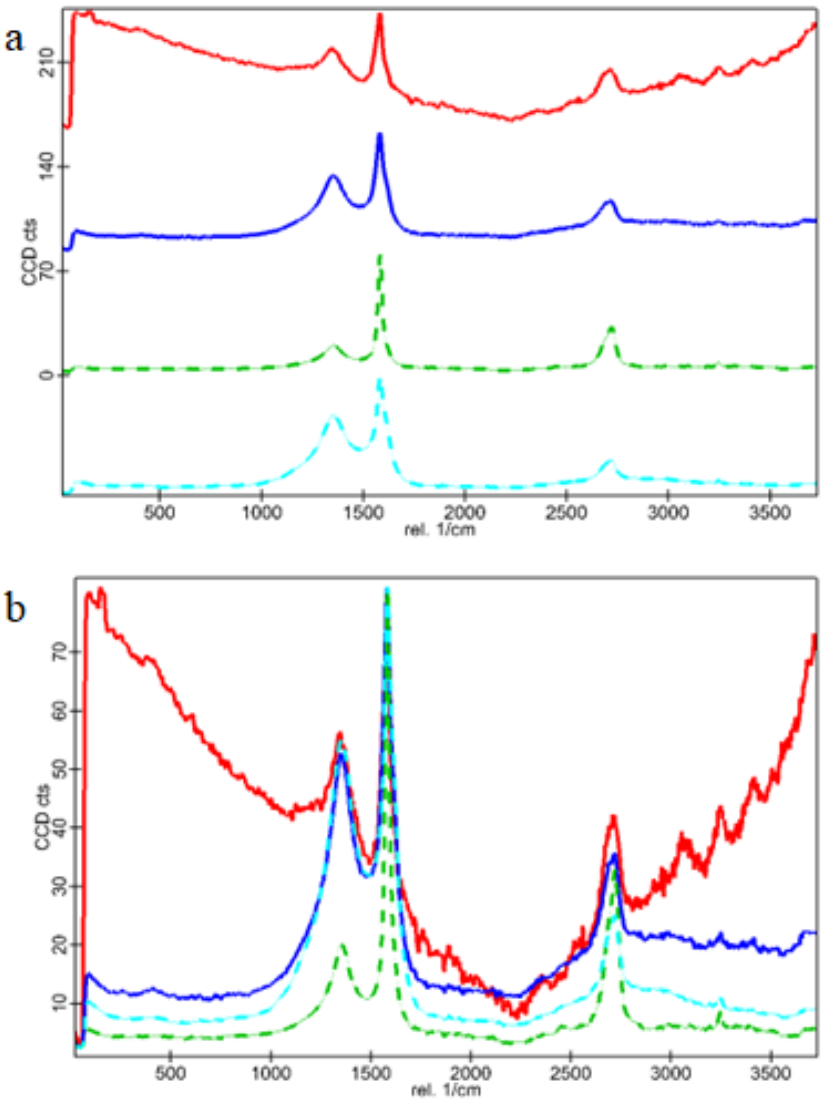

Figure 33. Re-position of the graphical output of 4 carbon cluster to select the best feature less impacted by the proximity of substrates around it; a) and b) are different representations from cascade mode to single merge respectively.

As commonly observed with graphite and graphite like structures, the main Raman modes that were detected was the G, D and 2D peak as shown in Figure 34. The resin cluster being more of a disordered carbon will have a more pronounced D-peak which is defect induce band[24,45]. The G-peak is observed in all sp^2 hybridized structures and can used

as a measure of highly ordered carbon when its intensity is high, and the D-peak is low in the case of graphite [24,45].

The analysis of the result shown in Figure 35, demonstrates the correlation potential in using Raman to track oxidation in carbon bonded refractories[24]. The analysis indicates that the intensity order ratio decreased for both the resin and graphite cluster as a function of oxidation[24]. For the resin a limit, was observed in terms of how far the cluster can be used to track oxidation[24]. This limit was observed at the 4-minute oxidation time-point which suggests that the substrate effects were too high at this level of oxidation for the resin features to be used (the limit amounts to about 20% conversion of resin phase)[24]. Aggregates within the refractory composite such as alumina and titania were observed to influence the G and D peak features at certain levels of oxidation[24]. The graphite phase was also affected by substrate effects at the same time-point, but the effect was less[24].

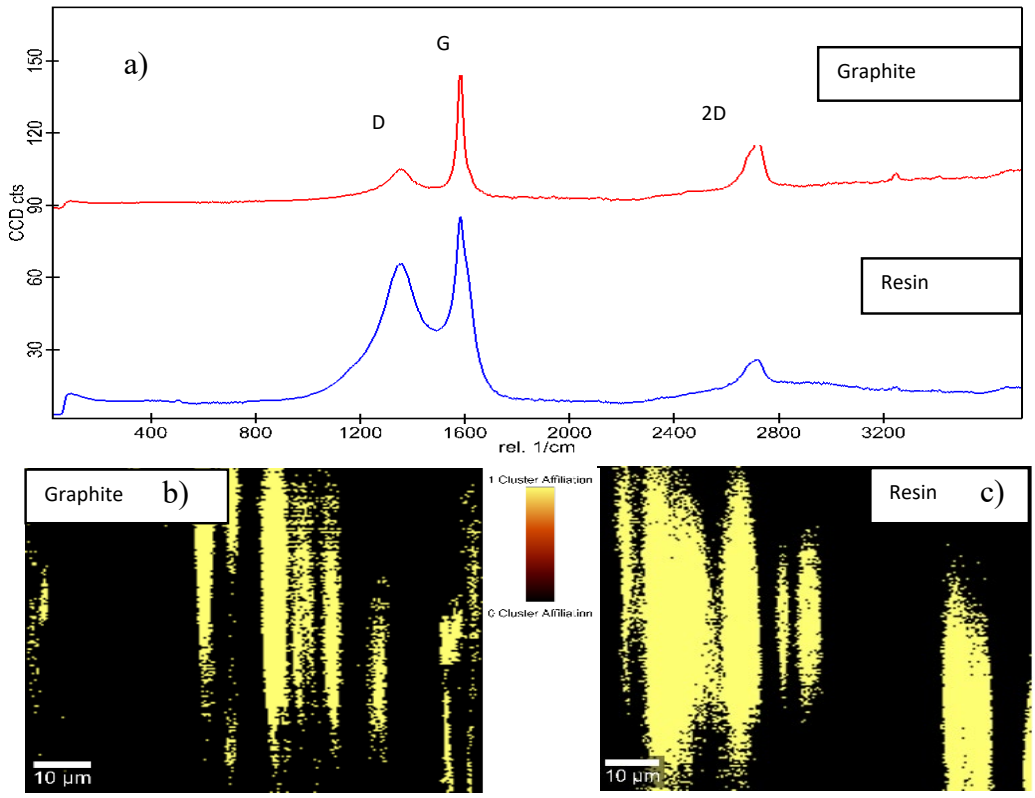

Figure 34. a) A Raman depth scan profile with applied cluster mapping using WiTec software to distinguish carbons. The top Raman spectra in red is Graphite (region) and the one below it in blue is the resin (region). b) and c) are their associated locations mapped in yellow with each pixel representing a Raman spectrum. The black regions are for masking other carbon regions affected by substrates[24].

Crystallite sizes increased as function of oxidation for the resin phase with the same the substrate effect occurring at the 4-minute oxidation time-point[24]. The crystallite size of

graphite remined the same throughout but an anomaly was measure at the 3-minute oxidation time-point which can be attributed to the fitting method used as well as the effect of substrates within that particular scanned region[24,132].

The correlation found within this work seems to suggest that correlation of carbon features in Raman Spectra to oxidation is material specific[24,131]. Studies in these areas are rare, however one such studies that can be used to contrast findings were those conducted by Lu, et al on grades of nuclear graphite[131]. The only correlation found in their study was with FWHM (full width half maximum) often used to determine crystallite size of carbon materials[131]. The trend of increase crystallite size with respect to oxidation as observed in this study was also the same trend observed in their study with respect to their FWHM maximum assessment[24,131]. The additional correlation found in this work in relation to I_D/I_G ratio which they were unable to find may also be attributable to the mapping technique and statistically cluster algorithm software that can help uncover features otherwise difficult to assess in the absence of advance techniques as used in this work[24]. Lu, et al., summarises the oxidation tracking behaviour as the monitoring of preferential oxidation of binders which by default have smaller nano-crystallite sizes, and with the progression of oxidation larger nano-crystallite sizes in the filler part of the material are exposed[24,131]. Due to the density of and microstructure of fillers, the oxygen reacts with the fillers by starting from their outer surface [24]. This meant that oxygen could not diffuse in between the nano-crystallites sizes in the filler as it does in resin binder phase and therefore the crystallites do not change in size for the filler[24]. Extrapolating from the judgement made by Lu, et al., about the constancy of crystallite size with respect to filler, a similar observation can be drawn from the analysis of this work regarding the constancy of crystallite size measured with the graphite cluster region as shown in Figure 35 b[24]. Further oxidation with graphite beyond the resin temperature region therefore should not affect the graphite crystallite sizes apart from the effect of substrates as observed in this study[24,131].

A higher temperature isothermal oxidation experiment was however attempted to oxidise graphite phase with the same time-points and environmental conditions as resin; however, the degree of oxidation was severe enough for the substrates to have a great influence on the signals obtained at each time interval. Out of the signal that could be obtained which we were also affected greatly by substrate effects their crystallite sizes remained similar.

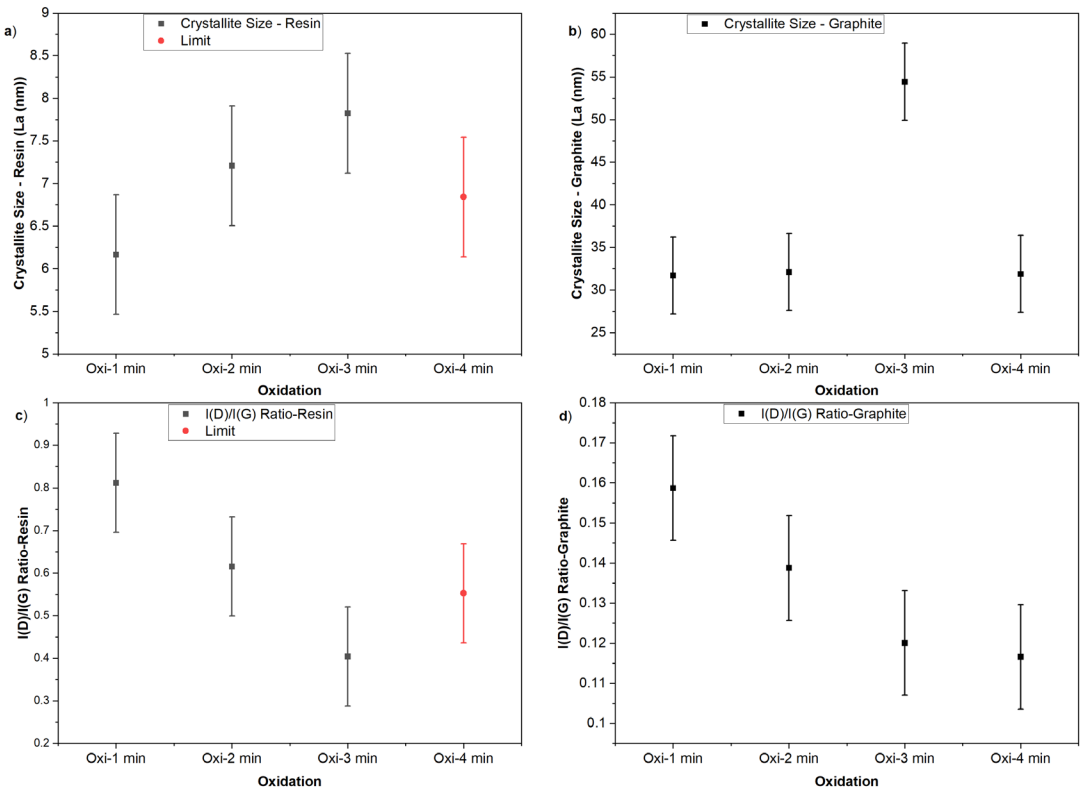

Figure 35. a) Crystallite size measured for resin as a function of oxidation time, b) Graphite crystallite size as a function of oxidation, c) The change in I_D/I_G ratio of resin phase with respect to oxidation and d) The I_D/I_G ratio change of the graphite phase with respect to oxidation point[24].

Further analysis of the substrate effect during the lower temperatures experiment conducted to preferentially oxidised the resin, highlighted some interesting features. The G intensity may have been expected to increase as resin oxidised however it was realised that this may not always be the case[24]. Sample oxidised at the two-minute interval decreased in signal compared to the previous time-point, which suggest a suppressive effect on the signals obtained[24]. Upon investigation of the map obtained within the scanned region (2-min oxidation sample), high intensity TiO_2 signals were observed[24]. The G-peak and D-peak intensity for both the resin and graphite clusters decreased (depicted in Figure 36). Beyond this point of oxidation, the intensity of the G-peak did increase and TiO_2 was not found in the map of those regions. TiO_2 is known as an oxidation inhibitor in refractories that stabilises the electronic configuration structure of graphite by donating electron which explains its presence[81]. Since, the effect observed was similar to what was observed in studies pertaining to the improvement of catalytic behaviour of titania, where an increase in titania decreased graphene signals and vice versa; the same conclusions were applied in this work[24,133–135]. Peaks of titania were

identified at 158, 399, 501 and 615 (rel.cm^{-1}) on the Raman spectra as shown in Figure 36 [24,133–135].

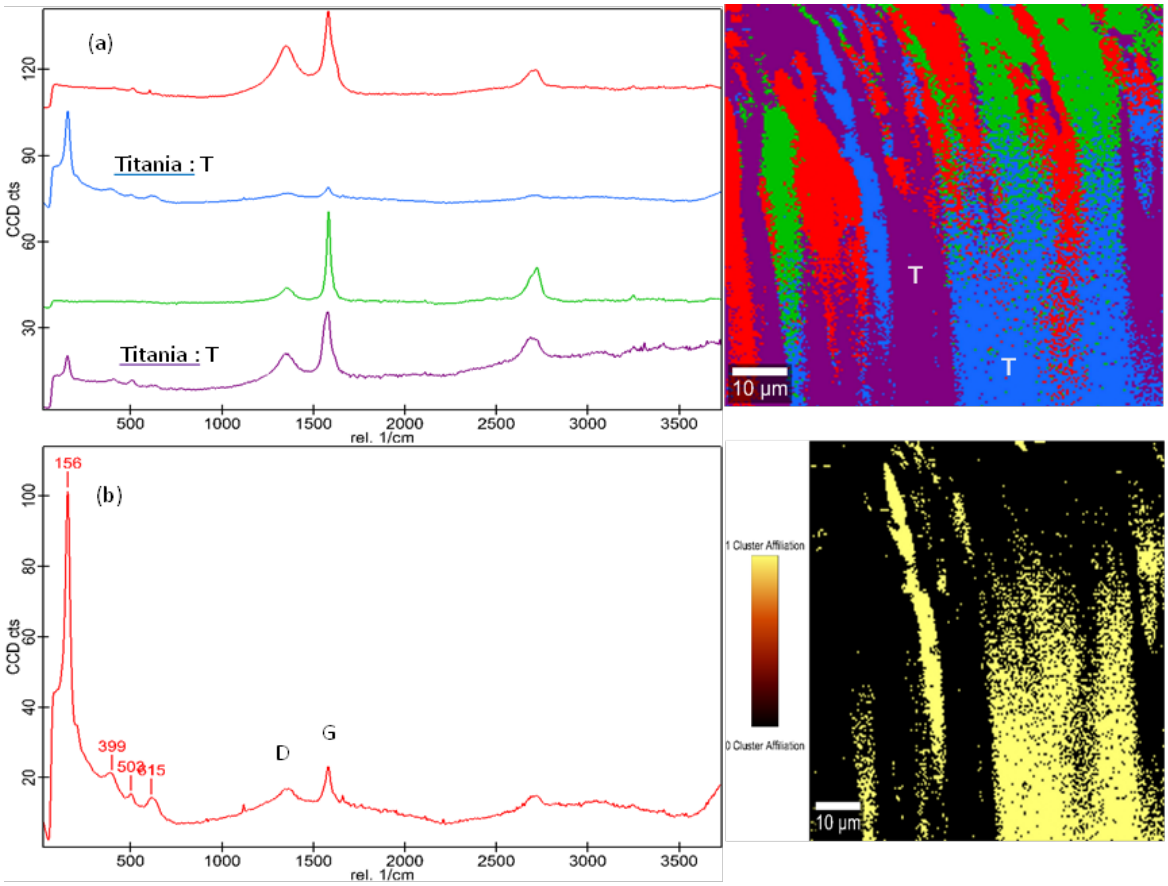

Figure 36. Effect of titania suppression on the G and D peak clusters at 2-minute oxidation point. (a) 4 cluster mapped with their respective locations; Two clusters show high intensities of titania peaks: 156, 399, 503, and 615 rel.cm^{-1}. (b) b) A single graphical output from the cluster showing the peaks of titania and suppressed signals of the carbon peaks (G and D).

Aggregate such as alumina, and silica can also impact signals obtained on heavily oxidised samples in a process known as interference[24,49]. The also includes metallic antioxidants such as silicon and aluminium often found in refractories[49]. The presence of these major aggregates and their metallic counterparts can amplify signals obtained [24,49]. The effect of these major aggregates was clearly observable at 4-minute oxidation time-point (see Figure 37 a).

When the changes in peak components were assessed for the resin cluster, only its hwhm (half width half maximum) of its G peak remained slightly stable[24]. All assessed components increased significantly from the previous oxidation time point. This meant that at the 4-oxidation time-point all clusters would have been affected by substrates within the refractory. Graphite components remained fairly stable but exhibited a significant increase in peak intensity (see Figure 37 b). Another reason why the resin clusters was more

affected is due to its poor suppression of the alumina fluorescence effect compared to graphite[24,49].

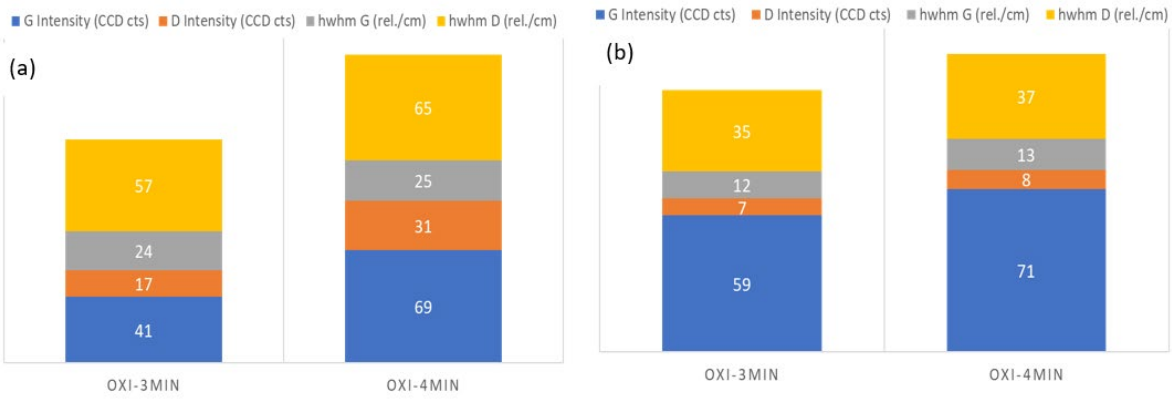

Figure 37. Changes in peak components due to substrate effects; from 3-minute oxidation to the 4-minute oxidation time point. a) component cluster of resin least affected at each oxidation level, and b) component of the least affected graphite cluster at each oxidation level.

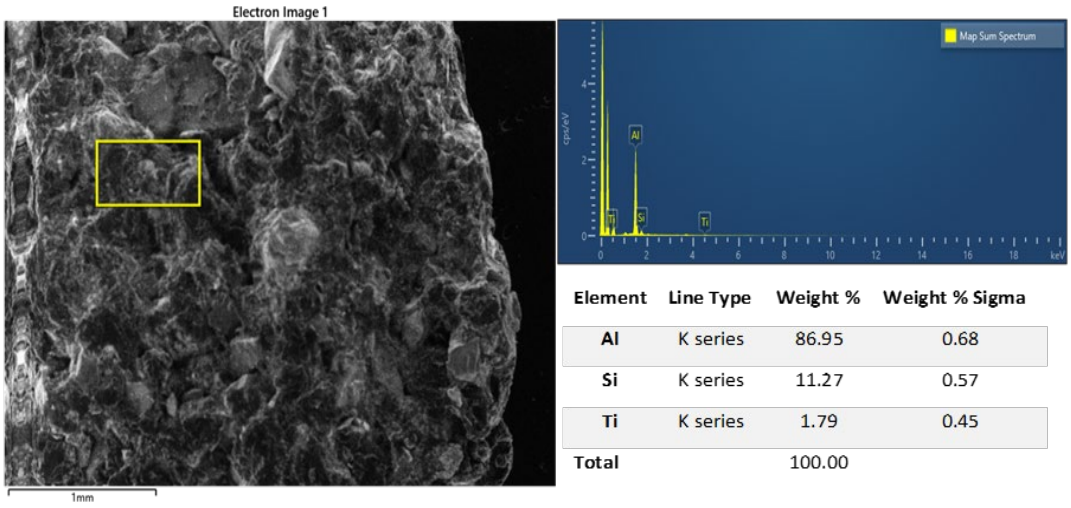

Element	Line Type	Weight %	Weight % Sigma
Al	K series	86.95	0.68
Si	K series	11.27	0.57
Ti	K series	1.79	0.45
Total		100.00	

Figure 38. EDS map of elements of in the refractory that can impact signals obtained by Raman (Aluminium silicon and titanium) using the oxidised sample at 1 minute oxidation timepoint.

Finally, the shift in peak position was assessed with respect to oxidation to evaluate the strain effects of the composite[24]. In the resin cluster region, the G-peak position changed from its compressive state at room temperature and decreased with respect to oxidation, up to the 3-minute interval (1586 rel.cm^{-1};1582 rel.cm^{-1}; 1579 rel.cm^{-1})[24]. It therefore transforms into a tensile state at the 3-minute interval. Contrasting this to the graphite cluster, which only changed from the 3-minute oxidation time point to 4-minute oxidation time point[24]. The graphite G-peak decreased in peak position value (1576 rel.cm^{-1}) putting into a tensile state, the effect of which can be attributed to substrates within the refractory composite[24]. The G-peak as explain in the literature review is positioned by default (without any strain effects) at ~ 1581 rel.cm^{-1}, an increased in value is therefore

attributed to a compressive state and a decrease in value is reference to a tensile state[24,91]. The non-oxidised samples of graphite and resin peak positions were 1582 cm^{-1} and 1583 cm^{-1}, respectively.

Chapter 7-Synergistic uses of Raman with XPS and μ-CT to evaluate chemical and microstructural influence on oxidation

The oxidation behaviour observed within the refractory composite at high temperatures will be govern by both chemical reaction and diffusion as discussed in previous chapters[11,39]. At different stages one process may be more pronounced than the other[11,39]. It is therefore important to understand both the chemical and microstructural influences that contribute to these processes and assess where Raman can bring value if adopted in industry.

XPS is a highly sensitive technique for surface analysis and is less affected by bulk effect observed (as observed in previous section) in Raman[44]. It is especially useful when used to study and quantify the bonding hybridisation of carbon (i.e., sp^2 $sp^{3)}$[45]. The sp^3 feature (an indicator of a compound being less graphitised/amorphous) in a Raman spectrum that appears for diamond is typically 50 – 100 times smaller than the sp^2 graphite feature[45]. This is due to resonant effects making it difficult to accurately determine the correct amounts of sp^2 to sp^3 ratio when using Raman[45]. XPS therefore supplements Raman by providing this ratio using it owns carbon order parameter known as the D-parameter[43]. This parameter will be evaluated with respect to the preheated industrial SEN samples and Virgin SEN samples.

The cluster algorithm was used as applied to initially distinguish between carbon regions unaffected and regions where, due to the close proximity of aggregates, the signals obtained were affected influenced negatively(by aggregates)[24]. The best signal out of each map representing a graphite phase (graphite rich region) and resin phase (resin rich region) was then used to evaluate their chemical order as function of preheated time.

The combined (averaged) carbon signal of the entire map that contained all the clusters in one sample was also assessed to see if this feature can be as reliable as selecting a single cluster from each sample as a comparator between SENs.

Location tracking the WiTec Raman microscope was used to navigate through sample precisely and store location of scans which was quite when learning about the material. Multiple scans were initially conducted using the above tool to understand carbon

signatures at different regions and the number of clusters that can give the best information about the sample's microstructure.

A lateral scan approach was taken in this instance to map samples so that changes to surface characteristic can be easily picked up and not skewed by other influences as alluded to in previous sections. Scanned regions were carefully selected in the inner part of the bulk away from the interface of coating to avoid poor carbon signals.

In terms of XPS, a surface scan and depth scan were conducted on samples (taken from Virgin SEN and preheated SEN) to reveal the chemistry of the carbon that may influence their sensitivity to oxidation (see Figure 43). The carbon auger peak was used in this part of the study for analysis of carbon features. It was transformed by way of synthetic differential to obtain the D-parameter (see Figure 43 c and Figure 43 d) which is relatable to sp^2/p^3 ratio. Pure graphite value for D-parameter with 100% sp^2 is documented as 22.5 by Lascovich[50]. For the less ordered carbons, their values would be less than this number due to higher percentage of sp^3 [43].

The mapped scan of the Raman spectra displayed very unique characteristics in terms of which features were more visible with respect to preheating. The virgin sample shown in Figure 39 (labelled Top), evidenced that the resin phase (labelled A in area colour map) was a visibly dominant feature in terms of area covered (in pixels) (refer to brown area map labelled A in Figure 39). Three out of the four clusters (carbon signals with respect to their D-peak) in the Virgin SEN sample are thus more influenced by the resin phase much more so than the 3-hour preheated (labelled Middle on Figure 39) and 6-hour preheated SEN (labelled Bottom on Figure 39). These are also represented by the arrows pointing upwards indicating the intensity/concentration of the D-peak (i.e., due to the contribution of resin). Their D-peaks intensity if compared across samples is therefore much higher. The other contrasting differences in surface characteristics is that graphite phase becomes more clearly visible for the 6-hour preheated SEN sample (labelled Bottom on Figure 39). The pristine nature of the graphite (i.e., the lowest D peak intensity) can be detected more so with this sample when using cluster of least affected cluster rule from previous section (labelled LG). At all levels of heating condition and in each map, the influence of aggregates is observable by noisy data, dampened signal or raised background/signal[24].

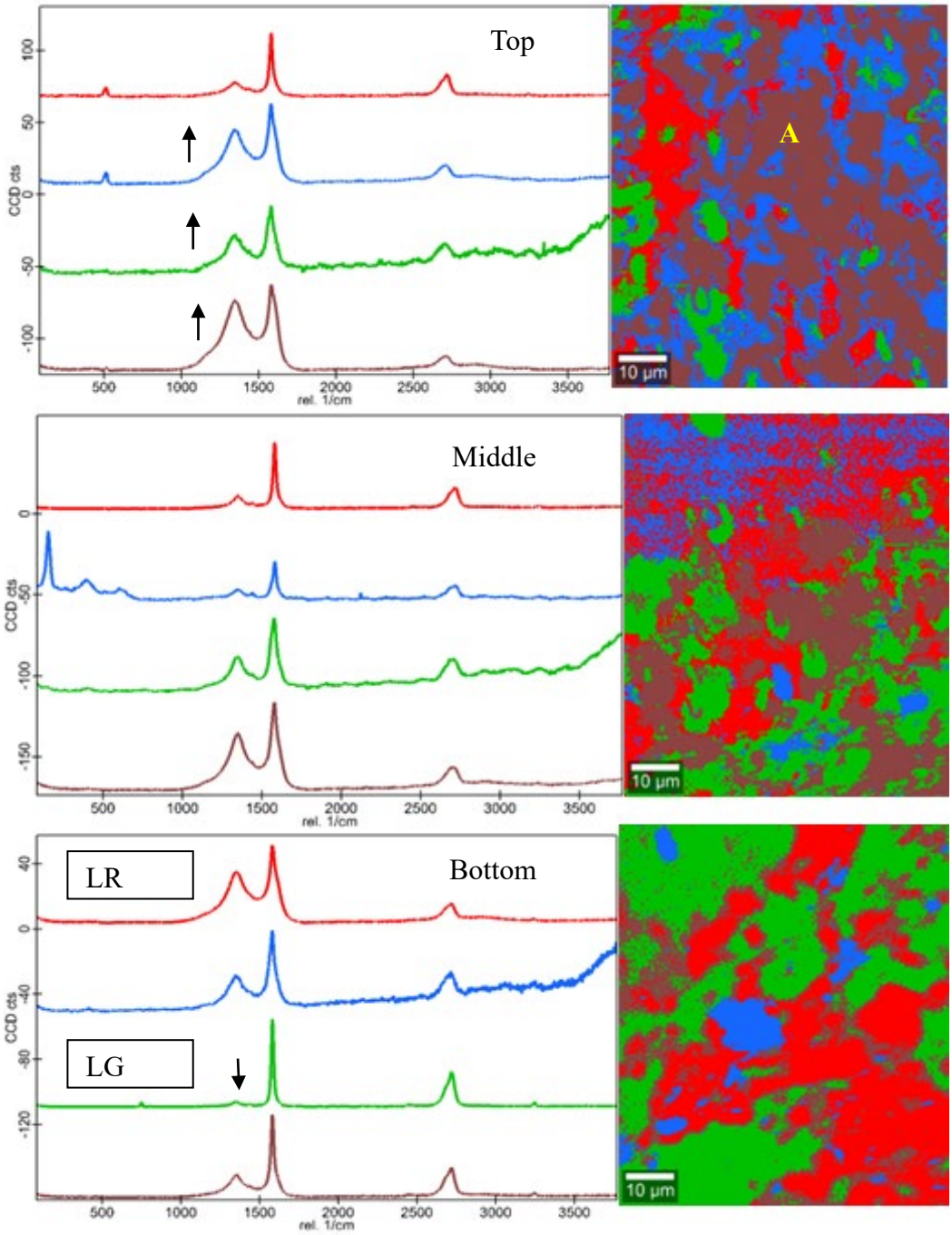

Figure 39. Cluster lateral Map of a virgin (Top), 3-hour preheated (Middle) and 6-hour preheated sample (Bottom) showing distribution of carbon and their respective location.The least affect cluster in each map be resolved by intensity of D peak and whether data is influenced by aggregate. LG represent least graphite rich region, LR represnts least affected resin rich region. A is showing an area coverage of a single cluster. Arrow pointing upwards due to higher defect and downwards due to lower defect.

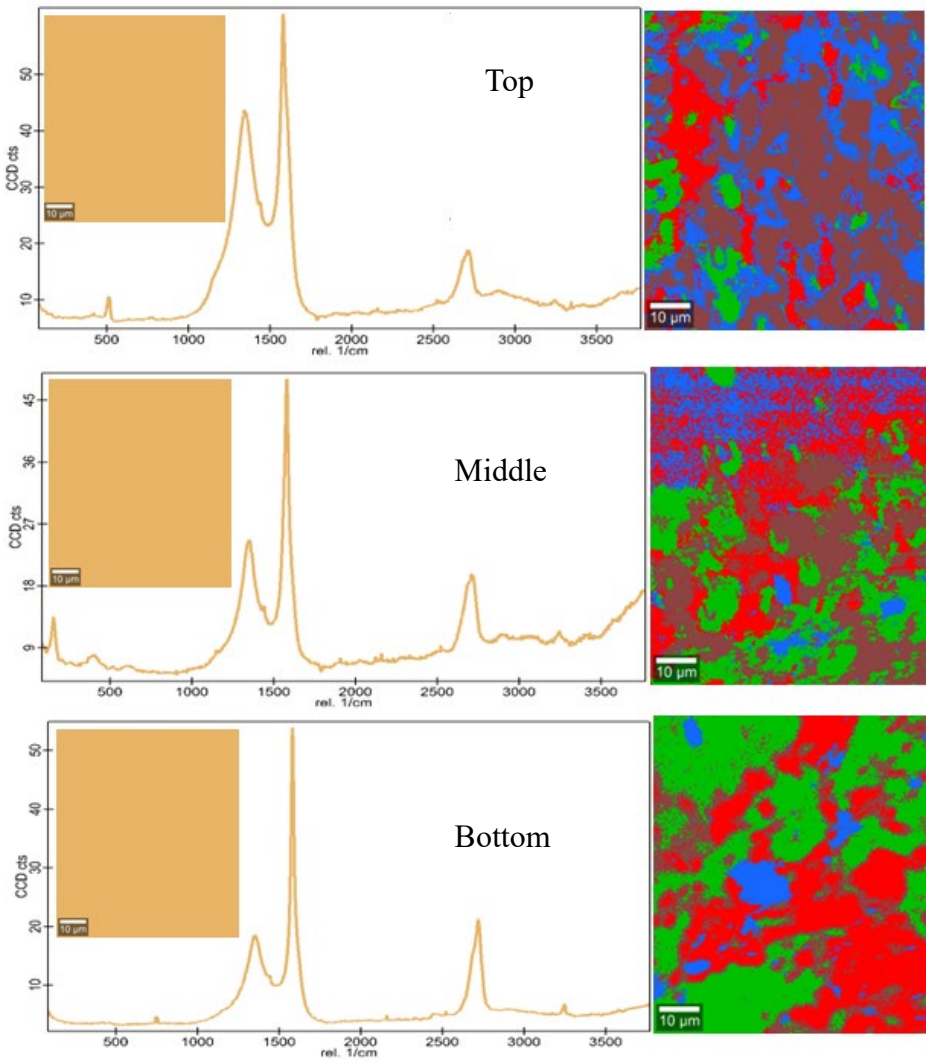

Figure 40. Combine (averaged) map of the entire cluster in each SEN sampling showed a clearer difference in terms D peaks Intensities. The D-peak decreases from image labelled Top (Virgin SEN sample) to Middle (3-hour preheated SEN sample) and then Bottom (6-hour preheated SEN sample) which has the lowest D-peak intensity.

The combined statistical output of the entire mapped area produces an averaged carbon signature representing the total change in surface characteristics as depicted in Figure 40. There is an obvious change in the order of carbon from virgin to 3-hour and 6-hour preheat. The surface becomes seemingly more graphitised/ordered which can be explain by the reduction of the resin phase at the surface and the expansion of graphite when heated[24,46]. Since there were no obvious signs of oxidation on the scanned region the reduction of resin phase can thus be attributed to it pyrolytic degradation as observed by Sallah et al., during high temperature Raman scan in inert atmospheres and other studies pertaining to the transient change of elastic Young's modulus upon heating [24,46,47]. Additionally, the aggregate or substrate effect is less visible in the 6-hour (bottom image Figure 40) due to the higher presence of graphite suppressing the effect of fluorescence as

previously alluded to in prior chapters [24,133,134]. From the scaling factor on the y-axis (CCD counts/cts) of the combined map, it is observable that the middle image appears to have least CCD cts (i.e., Intensity). As noted in the previous chapters this effect was due to the presence of titania peaks on the spectra whose influence depends on the carbon to titania amount present within the scanned region[24,133,134]. To quantify these effects the crystallite sizes and I_D/I_G ratio were determined for the combined map and for those where clustering was applied to obtain the least affected graphite and resin phase (seen Figure 41).

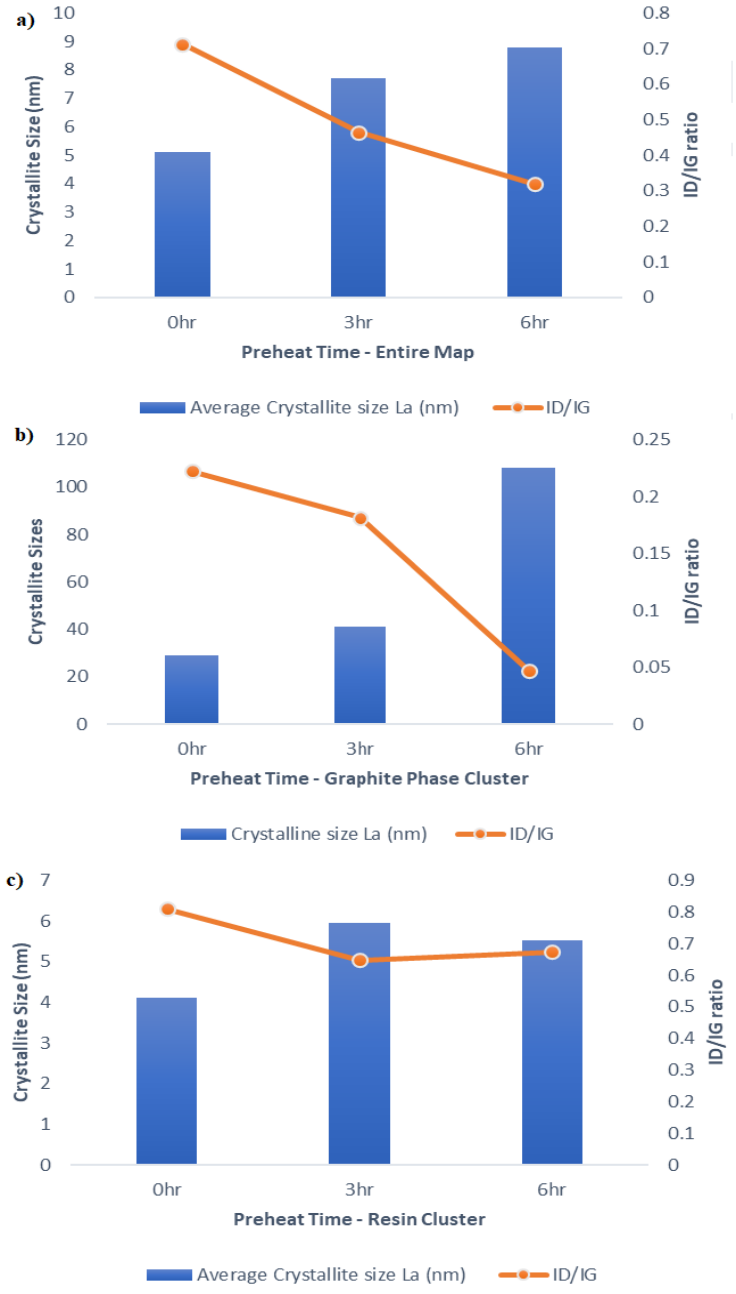

Figure 41. The crystallite size of graphite and I_D/I_G ratio of virgin, 3-hour preheated, and 6-hour preheated SEN sample determine.

From Figure 41, It was observed that the combined map and graphite cluster follow a similar trend. The crystallite size measured increased as a function pre-heat time. The I_D/I_G ratio decreased as a consequence resulting in better ordering on of the mapped surface carbons. For the resin cluster analysis, the preheated samples had higher crystallite sizes and lower I_D/I_G ratio indicating again, the ordering of surface characteristics. However, when comparing between the 3-hour to 6-hour preheated sample, it is more complex since their differences in minimal and the influence of aggregate cannot be ignored. The result for resin clusters indicates that the 3-hour preheated sample may have a higher crystallite size than the 6-hour preheated which is not expected give the overall assessment of the trend observed with the combined map analysis. To understand why there can be such an anomaly, the resin carbon signature from their respect maps were assessed. The Raman carbon signature of the 6-hour preheated resin cluster (see bottom image in: blue colour line) has features of noise with raised background due to the fluorescence effect which is not observed with the Resin cluster 3-hour preheated sample (middle image: Brown colour line). Therefore, the effect of aggregate in the 6-hour preheated sample causes peak broadening resulting in lower crystallite size than the 3-hour sample. This also changes the lorentzian fitting parameters of the D and G peak intensity values resulting in slightly higher I_D/I_G ratio[24]. The same broadening effects were also observed in the oxidation Raman tracking study of preferential oxidation of binder[24].

For further validation and clarity on surface characteristics and the possible carbon reactions occurring, an XPS analysis was conducted for both etched and non-etched samples. It was observed that the etching samples exposed the graphite features more readily and were therefore attributed to graphite. The non-etched sample were used to reference to the resin phase (see Figure 42). By combining and then averaging the values of the etched (graphite) and non-etched (resin) samples in each respective category of samples: virgin, 3-hour and 6-hour preheated sample, a measurement of D-parameter representing the total surface characteristics of was calculated. This similar to having the combined map feature as observed with the Raman analysis. In each category of samples (virgin, 3-hour and 6-hour preheated sample), the D-parameter of the non-combined features (etched/graphite and non-etched/resin) were also assessed separately in resemblance to how Raman was used to assess resin phase and graphite phase with respect to pre-heat time (see Figure 42).

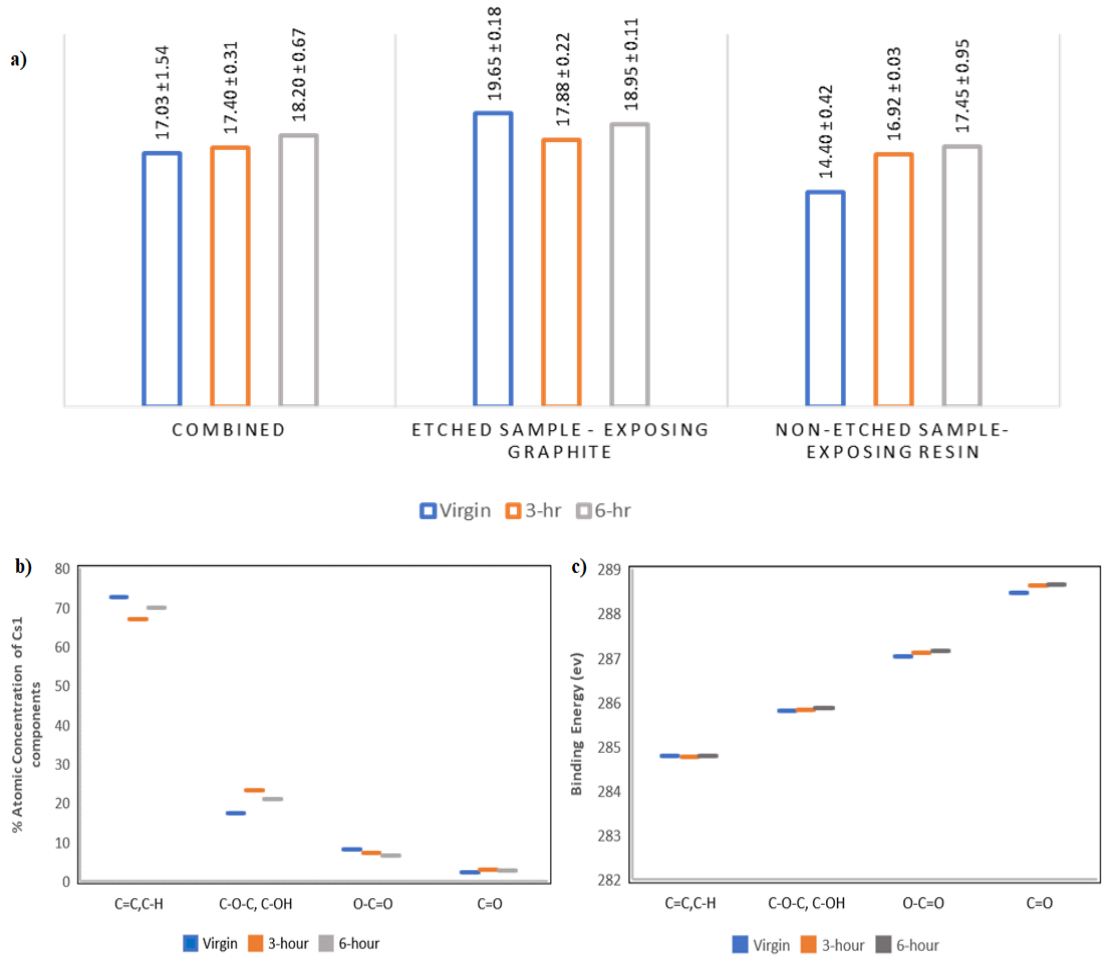

Figure 42. a) The average D-parameter of the combined etched and non-etched sample for virgin, 3 hour preheated and 6 hour preheated sample, b) Shows the %atomic concentration of the averaged combined C1s peak components for virgin (blue), 3-hour preheated (orange) and 6-hour (grey) samples, and c) is the binding energy (ev) of the averaged combined C1s peak components for virgin (blue), 3-hour preheated (orange) and 6-hour (grey) samples.

Similar to the Raman observation the XPS analysis of the combined D-parameter showed the that overall surface characteristics became more graphitised as a function of preheat time. In the non-etched sample, it was clear that the resin feature also became more graphitised which was not easily detected with Raman due to substrate effects. Graphitisation here does not imply that the resin is graphitised as a single entity (i.e., improvement in structure), rather this should be understood as the influence of graphite becoming more prevalent on the surface as the resin degrades changing the overall measure of surface features.

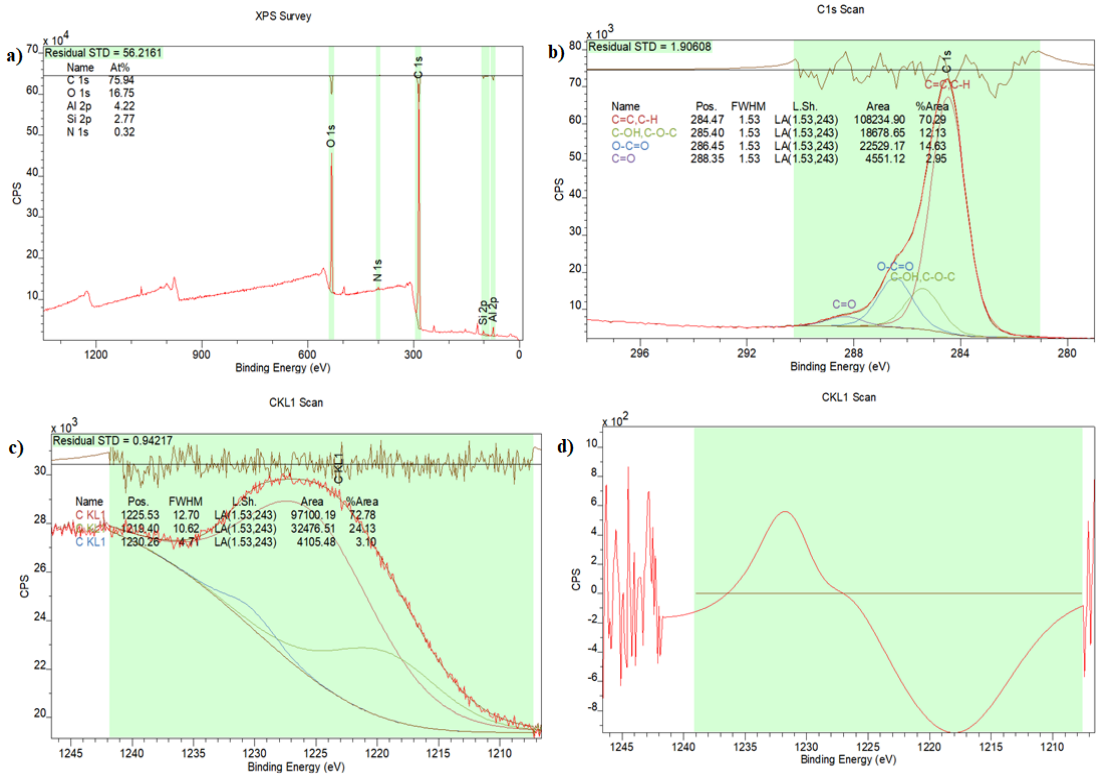

Figure 43. a) An xps survey scan of non-etched sample for identification for C1s peak, b) Deconvolution fitting of peak components into the C1s carbon peak, c) Carbon auger peak fitting and synthetic differential to produce the D parameter from d) graphical representation of the result produced from the differential of carbon auger peak (fitting of the component with sp2/sp3 type background gives a FWHM equivalent to the D-parameter)

From the analysis of the etched samples a new insight is uncovered in terms of graphite phase behaviour not otherwise observable with Raman. The virgin sample when etched produces higher D parameter value close to ~ 20. Contrasting this with the preheated group which have values less than the virgin indicating that the graphite chemistry has increased in sp^3 formation which is possibly through the interfacial reaction of the resin (its trapped pyrolytic products) with graphite. The sp^3 formation however decreases from the 3-hour to 6-hour sample which can either be a contribution of the chemical evolution of trapped pyrolytic products and/or expansion of graphite exposing the graphite phase region more readily than the 3-hour sample. The lower D parameter at the 3-hour sample can therefore be used to explain the reason why graphite oxidation was easier to occur with this sample than both the virgin and 6-hour pre-heated sample, since the reaction of graphite will occur at the surface edges/interfaces as explained by Lu et al., [131] (refer to oxidation results at Figure 31). The higher D-parameter of the virgin exposed graphite therefore also proves why the reaction at 0.2 conversion and its corresponding temperatures was less likely compared to the preheated group (refer to oxidation results at Figure 31). Furthermore, as a proposition as to why the 6-hour sample was more resistant to oxidation can also be

deduced. When the process of diffusion increases in effect at higher temperatures, the thermal expansion of the graphite and alumina causes further reduction in surface area of the interfacial site of reaction. The healing or closing of pore is described in detail by Werner et al. in carbon bonded refractory pyrolyzed samples during reheating and holding time at the pyrolysis temperature[46]. This physical effect (observed from the lower Arrhenius constant) and improved chemistry in the interfacial sites is the reason for being more resistant to oxidation at higher temperatures. These chemical bonding interfacial reactions are seldom investigated if not all in the context of carbon bonded refractories and their possible influence in oxidation studies.

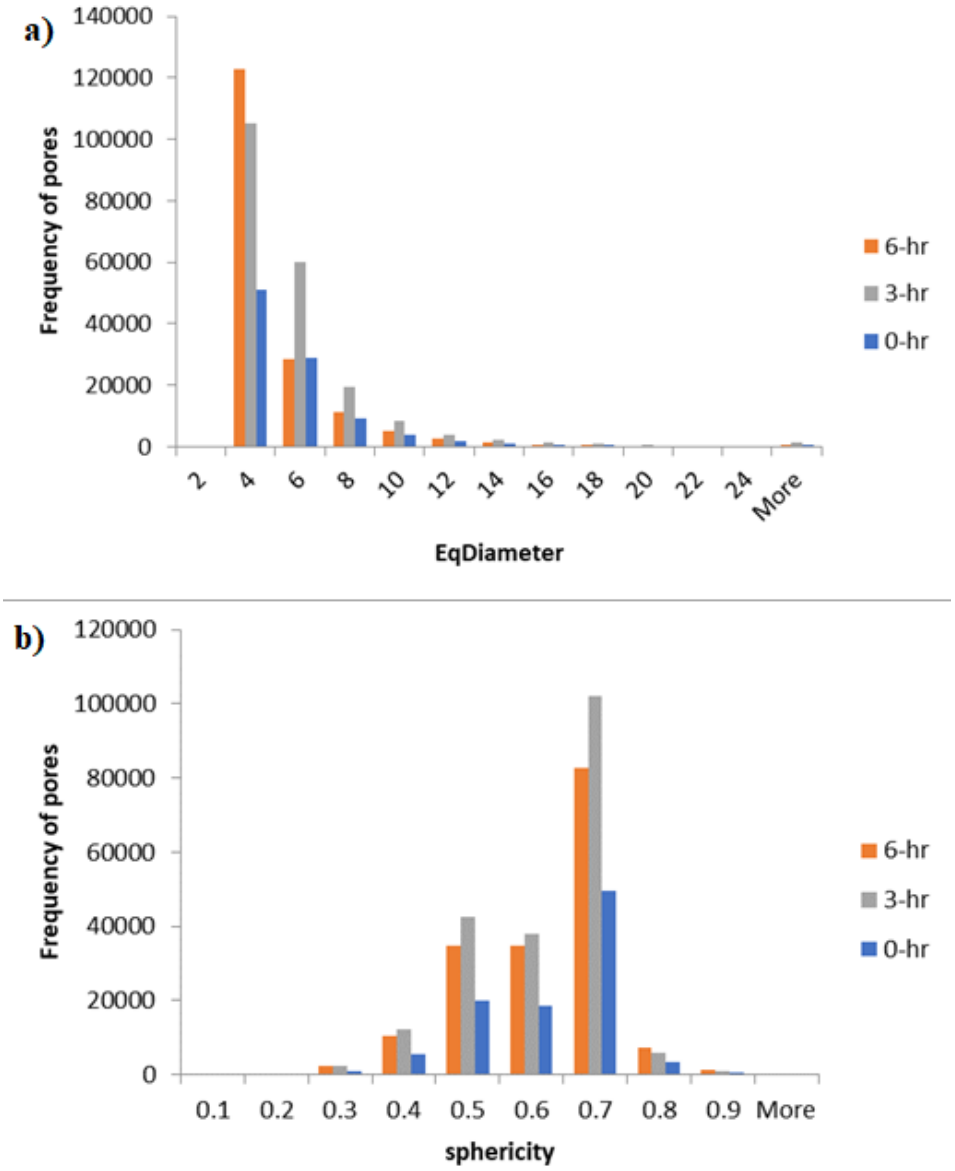

Figure 44. CT-scan native measure of Equivalent Diameter of the segmented refractory pores and b) Sphericity of pores calculated as reciprocal of the native measure of feretShape3d using avizo software.

As a final corroboration to support the findings discussed above, μ-CT analysis was performed to seek out microstructural influences that could shed more insight into the reactivity of these carbons. The refractory was segmented into high density aggregates, low density aggregates, combined region (small particles low density that are embedded within the carbon matrix), matrix phase 1 (high density) equivalent to graphite, matrix phase 2 (lower density) equivalent to resin and finally the pores. The pores were then analysed using the avizo software to produce measures of average area (3D), average volume (3D), average equivalent diameter < 25 μm, average ferret shape (3D) and a sphericity index using a reciprocal of the ferret shape (3D) measure (see Figure 44 and Table 8). The sphericity index can also be used to arrive at the same conclusion in terms of numbers of generated pores, however from this distribution their shape factor is practical the same on average. They had the same average sphericity of 0.6 and shape factor of ~1.8.

Table 8. CT-Scan measures of the segmented pores for a virgin sample (0-hour), 3 hour preheated SEN and 6 Hour preheated SEN. The main discriminatory measures are the average aread3d and average volume 3d which show a decline in with respect to preheat

Measures	**Preheat Time**		
	0-Hour	3-Hour	6-Hour
Average Area3d	425.4	420.9	275.0
Average Volume3d	959.9	802.4	450.0
Average EqDiameter (<25)	4.7	4.7	3.8
Average FeretShape3d	1.8	1.8	1.8

The μ-CT results indicates that the preheated SENs would generate higher number of pores than the virgin SEN, when comparing the frequency distribution of pores with respect to their equivalent diameter (Figure 44). However, when comparing between the preheated SENs, overall, it indicates that the 3-hour SENs had generated greater numbers of pores than the 6-hour preheated SEN which indicates declining trend for those within preheating regime. The two main discriminatory measures that support the microstructural evidence that give the 6-hour preheated SEN an advantage at higher oxidation temperatures when the effect of diffusion is more sensitive are the average area 3d and average volume 3d; which are significantly less than both the virgin material and the 3-hour preheated SEN.

This therefore supports the proposition that the surface area reduction of the generated pores by graphite expansion and alumina at longer preheat time does have an effect. Apparent porosity does not always provide a direct indicator of refractory gaseous permeability as evidence by authors investigating alkali attack on alumina refractories[136,137]. The authors have noted that it is more useful to understand how pore sizes at different categories, their structure and volume may contribute to gaseous refractory attack[136,137].

The use of Raman in synergy with XPS and μ-CT has therefore, unveiled reaction differences of closely related structures. When structures are closely related it becomes challenge to find a suitable measurement parameter when trying to profile their behaviour. Obtained quantifiable parameter rather the reliance of interpretation of microstructural images would make it easier in future to correlate data from industrial practise with material performance. Interfacial reaction (i.e., affecting graphite active site) insight that can impact oxidation resistance of refractories and healing pore phenomena highlighted by the use of μ-CT discriminatory value, has highlighted the complementarity of these techniques with Raman analysis on chemical and structural changes observed.

Chapter 8-Implications of preheat on thermal Shock profiling of carbon-bonded refractory

This section examines the efficacy of using IET in profiling the thermal shock resistance of the Virgin and preheated SEN samples. Further insight will be probed using thermal diffusivity measurements from LFA and Raman.

Major studies have already been conducted in the area of thermal shock of ceramics laying the theoretical foundations we know today based on Hassleman's unified facture theory[23]. Monolithic ceramics have been the main focus of thermal shock studies in the past century[23]. With regards to composite, their predictability of in-service thermal shock still remains a challenge due to complexity of structures[23].

The investigation is this work therefore does not aim to emulate studies in trying to induce shock through cyclic quenching. Rather, the focus is more geared towards the industrial evaluation of the SEN's integrity during preheat treatment and its resistance to thermal shock. The insight obtained should enable better decisioning in terms of preheating practise, gathering data (process and material) to support to failure investigation and finding suitable quantitative methods to quantify damage observed in service.

Both LFA and IET are techniques that have been used to assess the thermal shock resistance of refractories in a non-destructive manner, however geometrical implications of the samples must be taken into consideration as they serve as inputs for calculation of properties[22,23,46]. The elastic Young's modulus produced from an IET has been used to understand implication of oxidation, pyrolytic degradation, and other physical effects[46]. Its sensitivity to microstructural changes makes it a suitable technique to apply in understanding the implications of preheating practises [46].

Another measurement produced from an IET instrument is the dampening factor[22,23]. The dampening or decaying of an acoustic wave signal depends on the amount of fault that lies in the material. A high Q factor value indicates that there is more fault (in this case cracks of networks cracks) impeding the travelling of the excited waves within the material[22]. Although the instrument can produce estimates of dampening from the vibrational frequency velocity data, it does not discriminate against bad signal. A range of frequencies also occurred during testing which needed averaging to determine the natural frequency of vibration of specimen. Some scholars have in the past found using dampening measurement incapable of detecting early stages of thermal shock fracture due to the measurement tool not being sensitive at all to small cracks with especially if only a few is present[23]. Additionally, the width of the frequency velocity curve, which is used to calculate dampening, has presented a challenge in relatively brittle materials. It often produces low Q values[23].

To overcome this challenge a series of test were conducted to find the natural frequencies of vibrations from the most frequently occurring, during testing. Using the test data corresponding to the determined natural frequency of vibration observed, the velocity plots were extracted and pre-processed with a curved fitting data analysis software. The fityk software made it possible to hide signals or neighbouring peak that may affect the width of the resonance frequency curve and by applying a lorentzian fitting model in each extracted peak a more consistent value of dampening Q value was obtained for each run.

The analysis of the elastic Young's modulus yielded values of 7.77 ± 0.01, 5.55 ± 0.10, 5.69 ± 0.02 (GPa) for the virgin, 3-hour preheated, and 6-hour preheated samples respectively (as depicted in Figure 45). The decrease in Young's modulus has been associated with both pyrolysis degradation in the absence of oxidising agents and oxidation where oxygen is present, by Werner et al[46]. However, in the examined samples no visible oxidation was inferred so the former is taken to be the reason for the decrease. It is also understood that heating causes the pore closure mechanism to occur, however cooling

causes the detachment of grains with the matrix[46,47]. Therefore, the more heated the product, the more the damaging factor to be expected, at least at room temperature. It is therefore clear why the preheated group had a lower elastic Young's modulus than the virgin.

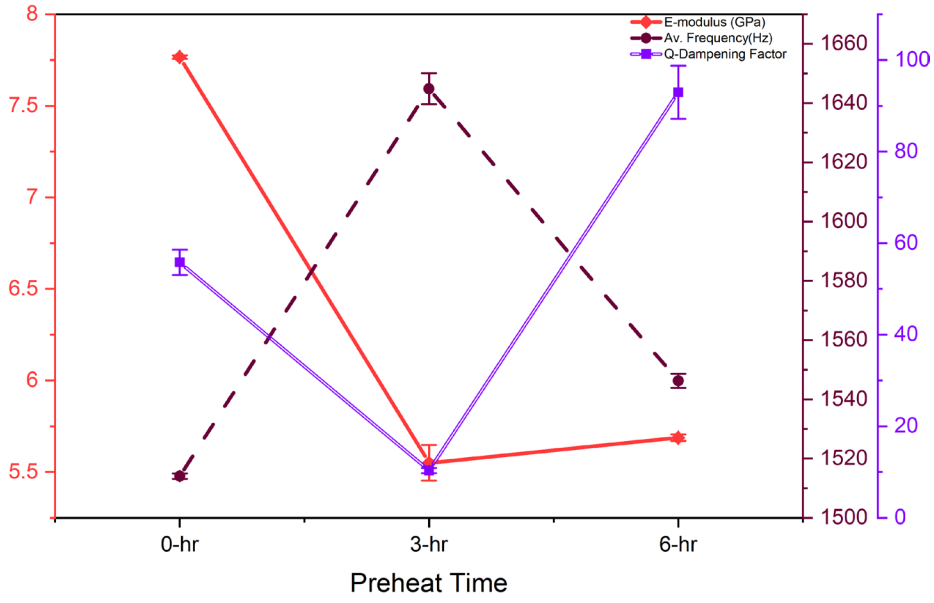

Figure 45 Results of IET test showing Elastic Young's Modulus (red diamond), Natural frequency of vibration (brown -circle), and Dampening factor Q (purple - square) for the virgin 0-hr, 3-hour preheated (3-hr) and 6-hour preheated (6-hr) sample.

The natural expectation therefore is to expect the longer preheated 6-hour sample to have a lower Young's modulus but in fact a slight increase was observed when compared against the 3-hour preheated SEN. Extrapolating from Werner et al.'s experiments on the study of elastic Young's modulus of alumina-carbon bonded refractories, this can happen in two ways[46]. It is either due to a sintering process at holding temperatures due to the expanding alumina grains (only limited by graphite or carbon content) which would manifest itself as an increase of elastic modulus at room temperature (if repeatedly heated and compared to previous cycle measurement)[46]. In the case where sintering does not occur room this phenomenon would be associated with microstructural changes owed to the fact that all single material expands in their own ways, and it is expected that the material undergoes a healing process with regards to pores and the micro-cracks formed[46].

Another question that may arise as to how this relates with its oxidation resistance, if the 6-hour preheat is the more damaged sample due to grain and matrix separation at cooling. Werner et al., also provides the evidence that the effect of gap closure upon reheating was more pronounced in the samples observed with more damage/network cracks than those

with lesser damage in their study[46]. The observations noted about oxidation in this study is therefore consistent in terms of behavioural interpretation.

Although the elastic Young's modulus is a sensitive measure for detecting changes in the material, the dampening provides a more contrasting view that helps in examining thermal shock resistance of closely related products. When we compare the thermal shock resistance of the three sample categories, it is clear that the 3-hour pre-heated sample is far more resistant than both the virgin and 6-hour preheated samples (see Figure 45). The 6-hour pre-heated SEN is the least thermal shock resistant of the samples, having the highest Q factor (see Figure 45).

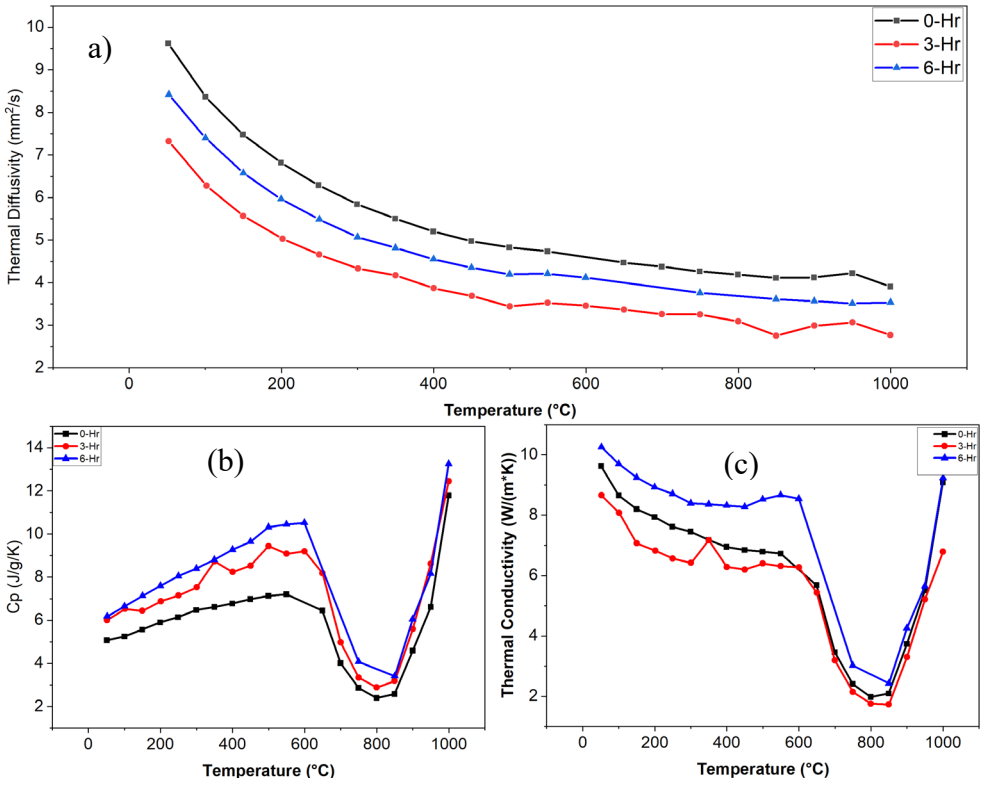

Figure 46. a) Image shows the thermal diffusivity of a refractory SEN sample as function temperature, b) show the change in Cp as and c) represents the changes in thermal conductivity all as a function of temperature increase for the Virgin SEN sample (0-Hr), 3-hour preheated SEN (3-Hr) and 6-Hour (6-Hr) preheated SEN sample.

The thermal diffusivity was also assessed as a profiling technique to see whether there will be a difference between the samples observed. The virgin and 6-hour preheated SEN samples demonstrated higher thermal diffusivity measurements than that of the 3-hour. This should have an effect on cooling time which is an important service parameter (see Figure 46). It advised that SENs should not cool below 800 °C during off-gas time, which therefore means that the risk of this happening is reduce more with the 3-hour preheated SEN[1,2,17,18]. The 6-hour preheated SEN had the highest thermal conductivity evidence

to support carbonisation/pyrolysis at longer preheating time improving the surface characteristics as observed with Raman, XPS, and LFA observation by Hu et al[138].

However, what is more pertinent for future implementation is to understand how each thermal shock event in service change the diffusivity profile. What would be the profile for a given preheat time that experiences thermal shock in service after spending a specific time period in contact with molten steel. It will be the answers to these question that would drive better failure classification in an industrial setting. The collection of preheat time data, in service or casting time data and the recovery of SEN that have failed will yield more insight, complementing the cyclic thermal quench test often conducted in laboratory environments. The diffusivity measurement can also be used to determine the type of cracks formed based on dimensional sensitivity of the technique[23].

An interesting feature was observed for the change in C_p and thermal conductivity. A dramatic decrease of measurement was observed at temperatures slightly above 500 °C and a recovery stage beginning at ~ 900 °C (see Figure 46). These temperatures coincide well with the pore closure phenomenon that is expected with carbon-bonded refractories due to thermal expansion mismatch (and its pyrolytic degradation). This insight may also suggest that care must be taken when bringing the SEN in contact with molten metal in avoiding installation at these temperatures where major changes are occurring. The starting position of the pore closure mechanism is known to be dependent on the sample microstructure and it can change depending on how the material is treated[46]. It is therefore a useful measure to consider if significant changes are imposed on the material unexpectedly.

Finally, a high temperature Raman analysis of the virgin sample was conducted inside an inert environmental chamber, which corroborated the microstructural findings of the pore closure mechanism (which was seemingly detected by the laser flash analyser)[24]. The analysis for the preheated samples were, however, unsuccessful due to pyrolytic release effects and the dramatic change in structure making it difficult to visualise and track the same position of interest.

Cluster analysis approach was used to distinguish between regions of carbon affected by aggregate and those that were least impacted[24]. A region dominant in resin and a region dominant in graphite phase were both evaluated with respect to temperature and their strain states (i.e., the shift in the G peak positions as a function of temperature). Each map was divided into three clusters comprising of one region that was the least affected by substrate effected (the same principle applied in previous sections)[24].

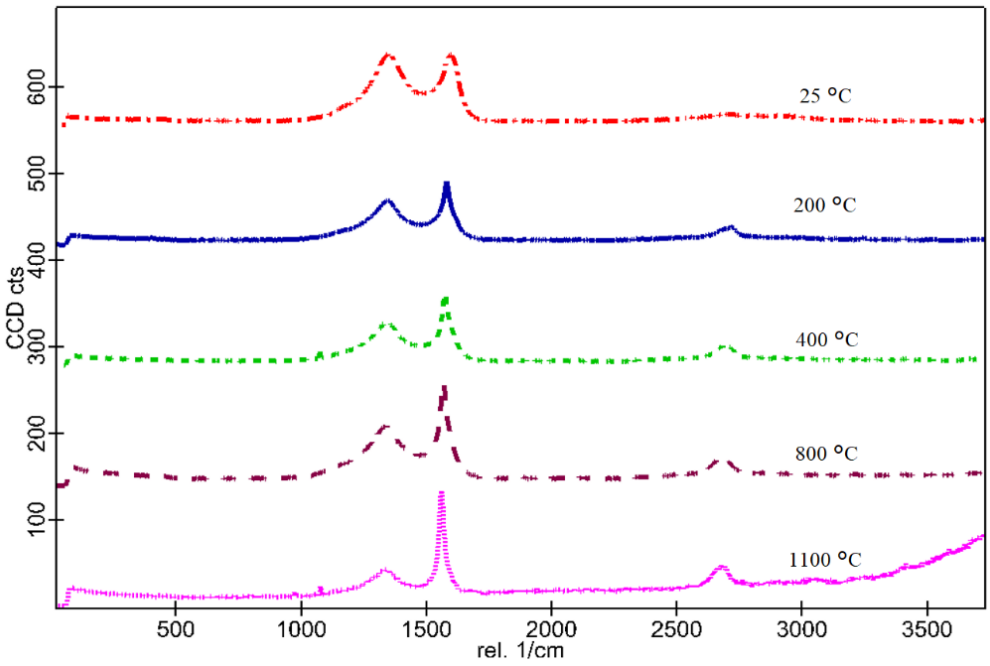

Figure 47. Resin cluster map of the least impacted signal by the substrate effect scanned with high temperature modulated Raman spectroscopy. Pyrolysis effect, followed by microstructural changes are observed with the decrease in D-peak and increase in 2D-peak exposing the graphite phase.

The shifting of the G-peak from its original position (1580 cm^{-1}) where no strain is imposed to higher values is considered a compressive strain whilst a decrease in value from this position is associated with a tensile state in a material[24]. A lorentzian peak fitting model was applied to both the G-peak and D-peak from which the calculations were derived[24].

The analysed resin cluster was in a compressive state at 25 °C and upon heating to 200 °C, it changed from a compressive state to a tensile state (i.e., from 1587.88 $rel.cm^{-1}$ to 1578.06 $rel.cm^{-1}$)[24]. This in stark contrast to graphite which only changed to a tensile state at 400 °C[24]. What was also interesting is that the remaining clusters of the resin and graphite that were influenced by the substrate effects all followed a similar trend to that of graphite least affected cluster[24].

Therefore, the changes from a compressive state to a tensile state for all the clusters point to 400 °C as the critical temperature/starting position, if we exclude the isolated resin cluster that is least affected by substrate (see Table 9)[24]. These findings therefore affirms that the microstructural changes that occur during pore closure phenomena is dominated by aggregate and graphite interaction as observed with by Werner et al and Luchini et al[24,46,47]. This also validates that Raman is a sensitive technique that may prove useful for detecting the starting position of these temperatures and can therefore be used to infer temperatures where the SEN should not be installed upon cooling.

Table 9. Table of G-Peak shifts peak position in support of the microstructural evolution at high temperature. Cluster A: represent clusters least impacted by substrates effect; Cluster B and C are clusters affected by substrate effect (graphite and aggregates).

Resin Rich Region				Graphite Rich Region			
Cluster A	Temperature (°C)	G-Peak (rel.cm^{-1})	Error	**Cluster A**	Temperature (°C)	G-Peak (rel.cm^{-1})	Error
	25	1587.88	1.11		25	1583.82	0.10
	200	1578.06	0.90		200	1582.37	0.05
	400	1575.29	0.62		**400**	1577.51	0.05
	800	1567.93	0.65		800	1569.83	0.05
	1100	1560.99	0.18		1100	1562.53	0.10
Cluster B	Temperature (°C)	G-Peak (rel.cm^{-1})	Error	**Cluster B**	Temperature (°C)	G-Peak (rel.cm^{-1})	Error
	25	1593.85	0.92		25	1583.49	0.31
	200	1582.72	0.60		200	1581.72	0.18
	400	1577.77	0.60		**400**	1577.99	0.21
	800	1570.44	0.57		800	1569.67	0.19
	1100	1563.56	0.36		1100	1563.17	0.26
Cluster C	Temperature (°C)	G-Peak (rel.cm^{-1})	Error	**Cluster C**	Temperature (°C)	G-Peak (rel.cm^{-1})	Error
	25	1590.18	0.92		25	1584.37	0.14
	200	1582.21	0.20		200	1582.32	0.10
	400	1577.29	0.56		**400**	1577.8	0.08
	800	1569.18	0.579		800	1569.73	0.06
	1100	1563.04	0.441		1100	1564.39	0.56

As well as detecting the critical temperature of pore closure within the composite, changes in surface characteristic were also observed. The reduction in resin features is indicative of pyrolysis taking place[24]. There is a noticeable decrease in the D-peak intensity as a function of temperature and an increase in the intensity of the 2D peak. As temperatures increases the graphite is exposed more to the surface, as it expands, and this will be occurring in combination with the effect of resin pyrolysis (see Figure 47)[24].

From these observations we can conclude that dampening factor Q, can be a critical measure for damage induced and resistance to thermal shock profiling in service. The additional use of diffusivity gives insight to best practise but can be further developed as a study to determine changes in profile due to thermal shock events based on its stability as a measure. Raman also provides a useful measure that is extremely sensitive to both

microstructural and chemical changes that can be used to support interpretation of behaviour or detect critical process induced changes within the observed refractories.

Conclusive Summary

This study has laid a foundation on the rapid oxidation kinetic profiling of refractories in a unique approach using model-free kinetic methods. Various model free methods have been tested to evaluate their effectiveness and the way in which to derive meaning from the kinetic parameters they produce. The non-conversion method of Ozawa, which is the simplest of the techniques can be used for determining the initial rate at the onset temperatures of a reaction for a given arbitrary temperature. A new empirical method was derived as an extension of the Friedman kinetic method to predict isothermal data from non-isothermal kinetic data successfully. The Vyazovkin method was the most accurate method for predicting kinetic behaviour and was therefore utilised with aid of software to profile the SENs.

The use of thermodynamics in conjunction with the isoconversion method in explaining oxidation resistance of closely related products in a quantifiable manner was successfully demonstrated by associating entropy with the Arrhenius constant kinetic parameter.

The success in explaining oxidation behaviour and pyrolytic degradation in this study was also made possible with the synergy of Raman instrumentation and advanced software capability that utilises a clustering algorithm to identify, track, and map microstructural features. New insight about substrate effects and signal processing were uncovered to help build a trackable relationship between Raman carbon signal and oxidation behaviour. With the use of Raman, it was possible to distinguish carbons, track oxidation using I_D/I_G ratio and crystallite sizes, infer pyrolytic degradation of resin, and evaluate the pore closure mechanism phenomena.

The final measurement tools used were XPS, IET, LFA and μ-CT which were all sensitive techniques that demonstrated usefulness in providing a comprehensive understanding of refractory behaviour in terms of chemistry, thermal shock resistance thermal property and microstructural behaviour respectively. The XPS D parameter highlighted interfacial chemical reaction changes that can occur between graphite and resin during preheat treatment, which can impact the oxidation resistance of the material. Q factor and thermal diffusivity gave a good insight as to how each SEN will behave in service in terms of their thermal shock resistance and thermal property changes. The μ-CT provided validation of the pore healing phenomenon and can be used for future studies to obtain useful

discriminatory measures for crack network (refer to appendices). For instance, the maximum pore size was observed with the 6-hour preheated SEN which in fact was considered the most damaged according to dampening Q factor. The dampening technique is more sensitive to larger pores, therefore establishing a rule of thumb that measures the critical pore sizes greater than or equal to 100 μm can be a useful examination in future studies.

The findings of this study suggest that the 3-hour preheating regime is more suitable in preventing thermal shock incidents than the extended preheated regime of 6 hours. The oxidation resistance of the bulk material improves over extended periods of preheating time (6-hour). As long as the bulk material is protected by the glass coating the material can sustain long preheat treatments with only the risk of a compromised thermal shock resistance and faster cooling during off-gas time.

These profiling techniques can be adopted to give a comprehensive insight on performance tracking and failure assessment when couple with process data in future if data analytic strategies are adopted. The foundational study also provides a means by which insight can be drawn in the absence of process data in way that overcome myriad of sample challenges and shorten causality analysis of failure by way of profiling expected characteristic from samples.

Future Recommendations

Since the profiles observed in some of the techniques used in this study is affected by the steel user process, it may be feasible to predict missing process data if it can be correlated. The profiling methods can also be used as a mechanism for improving failure classification and to distinguish causes of failure originating from material integrity or steel user's process. However, further work needs to be conducted to benefit from such an approach. Process information such as the burner selected, off-gas time, preheat time, casting time before failure needs to be measured for a reasonable period for the purpose of gathering process data that can influence failure. Therefore, the recovery of failed SENs must also be assessed with the same techniques followed by a reference journey of normal case with no failure. The latter can be conducted in a laboratory setting and validations can be achieved through industrial trials of normal case scenario to verify the profile expected. The combination of process data and profiling techniques will then be used to make a judgement on best practice to adopt. The gathering of data and utilisation of industrial

revolution 4.0 technologies can then be applied for better predictive analysis as the direction for future research.

The interaction of coating mix with the base bulk material was not assessed and therefore can be a useful area to apply the same techniques. Instead of utilising carbon as a sensor, one can use the transportation of silicon into the bulk and its densification on the coating to oxidation as an indicator of preheating practise and oxidation.

Since the dampening is more sensitive to larger pores correlating this with μ-CT pore analysis by establishing a rule of thumb that measures critical pore sizes greater than or equal to 100 μm as an example can be useful for understanding, profiling, and quantifying damages experience on refractories. The use of μ-CT in thermal shock analysis will therefore provide a unique opportunity for overcome dimensional and sample challenges involving when assess the SEN against techniques such as IET (which may not accommodate failure samples taken from the SEN is certain difficult areas to access).

Finally, these robust yet simple approaches (i.e., Raman and MFK) can be adopted to study other areas of refractory research such as inclusion on SEN and the slag crawling phenomena. It can be used to create future projects aimed at finding ways to extend the life of the SEN or adopt better strategies in practise.

Industrial Impact

There is an expected 2 % failure rate with the product. Some products (the type I worked on) are expected to be in service for 4 hours after preheat treatment (which varies in time). The cost per piece of the product varies depending on the type with the lowest cost at £120 per product piece.

Out of these varied products approximately 7000 were purchased/or used from only one type during 2018, where failures spiked in an unprecedent manner. From my analysis of the plant supplies data, just over 70% of all failures during that year occurred within the first hour in service which is not ideal.

In summary: 1400 out of 7000 of these are expected to fail yearly for only one type of product, and if it took 10 minutes to resolve each failure (which is a small estimate depending on severity), the total downtime per day amounts to 0.64 hours. The cost of downtime for a major company such as my sponsor company can be approximated to be 9000€/hr (Reference Source No. 172176 sponsor company internal report).

Eradicating failure within the hour (70%) by adopting the strategies from this study (data driven/informed decision and risk strategies) can save approximately £43Million (M)

worth of cost due to downtime. This also means less pieces used with saving of £168,000 (1400 pieces less).

Additional understanding provided by this study about the influence of the process (variable heat treatment times) on the product, means we can start to determine whether or not to increase sequence length of casting/or casting time which will also reduce the number of products pieces used per day. A mere increase of an hour in casting with the product can reduce 20% of the product used per day. An additional benefit is that it will also reduce the downtime required to swap over/installation of new product from 0.3 hours per day to 0.24 hours per day (approximately 3 minutes for installation). The cost of downtime will therefore reduce from about £20M to £16M.

Aside from the above points a peer-reviewed journal has been published detailing part of the method employed to hopefully generate more use cases across steel user's process. The published article can be found as follows: https://doi.org/10.1016/j.cartre.2022.100174;

References

[1] J.K.S. Svensson, A. Memarpour, V. Brabie, P.G. Jönsson, Studies of the decarburisation phenomena during preheating of submerged entry nozzles (SEN) in continuous casting processes, Ironmaking and Steelmaking. 44 (2017) 108–116. https://doi.org/10.1080/03019233.2016.1156900.

[2] J. Madias, E. Brandaleze, M. Bentancour, G. Walter, Behaviour during preheating of continuous casting refractories, CN Refractories(Germany). 5 (2002) 9–13. https://www.academia.edu/49940502/Behavior_during_preheating_of_continuous_casting_refractories (accessed February 18, 2023).

[3] S. Ge, M. Isac, R.I.L. Guthrie, Progress in strip casting technologies for steel; Technical developments, ISIJ International. 53 (2013) 729–742. https://doi.org/10.2355/ISIJINTERNATIONAL.53.729.

[4] A. Vakhrushev, A. Kharicha, M. Wu, A. Ludwig, Y. Tang, G. Hackl, G. Nitzl, J. Watzinger, J. Bohacek, On Modelling Parasitic Solidification Due to Heat Loss at Submerged Entry Nozzle Region of Continuous Casting Mold, Metals (Basel). 11 (2021) 1375. https://doi.org/10.3390/met11091375.

[5] F. Saldaña-Salas, E. Torres-Alonso, J.A. Ramos-Banderas, G. Solorio-Díaz, C.A. Hernández-Bocanegra, Analysis of the Depth of Immersion of the Submerged Entry Nozzle on the Oscillations of the Meniscus in a Continuous Casting Mold, Metals (Basel). 9 (2019). https://doi.org/10.3390/MET9050596.

[6] A.A. Diego, L. Demuner, G.R.D. Santos, K. Matos, M.C. Bezerra, C. Valadares, R.D. Duda, F. Vernilli, THE IMPACT OF CHEMICAL COMPOSITION CHANGE OF MOLD FLUX APPLIED IN LOW CARBON STEEL IN THE WEAR OF, (2015).

[7] L. Zhang, B.G. Thomas, X. Wang, K. Cai, EVALUATION AND CONTROL OF STEEL CLEANLINESS-REVIEW, Steelmaking Conference Proceedings. 85 (2002) 431–452. http://ccc.illinois.edu/PDF Files/Reports02/Clean_Steel_Review-ISS2002.pdf (accessed May 15, 2018).

[8] B.H. Reis, W.V. Bielefeldt, A.C.F. Vilela, Efficiency of Inclusion Absorption by Slags during Secondary Refining of Steel, ISIJ International. 54 (2014). https://doi.org/10.2355/isijinternational.54.1584.

[9] M. Andersson, M. Hallberg, L. Jonsson, P. Jönsson, Slag-metal reactions during ladle treatment with focus on desulphurisation, Ironmaking & Steelmaking. 29 (2002) 224–232. https://doi.org/10.1179/030192302225004106.

[10] E.M.M. Ewais, Carbon based refractories, Journal of the Ceramic Society of Japan. 112 (2004) 517–532. https://doi.org/10.2109/jcersj.112.517.

[11] B. Chatterjee, K. Singh, Oxidation Phenomena in Carbon containing Refractories and their Protection, NML Technical Journal. 34 (1992) 27–34.

[12] B.M. Thethwayo, J.D. Steenkamp, A review of carbon-based refractory materials and their applications, J South Afr Inst Min Metall. 120 (2020). https://doi.org/10.17159/2411-9717/1011/2020.

[13] P. Das, S. Sinhamahapatra, K. Dana, S. Mukhopadhyay, Improvement of thermal conductivity of carbonaceous matrix in monolithic Al2O3–C refractory composite by surface-modified graphites, Ceram Int. 46 (2020) 29173–29181. https://doi.org/10.1016/j.ceramint.2020.08.090.

[14] A. Kumar, R. Khanna, M. Ikram-Ul-Haq, J. Spink, V. Sahajwalla, Effect of Glaze on the Corrosion Behavior of ZrO2-Graphite Insert of the Submerged Entry Nozzle in the Continuous Casting of Steel, Steel Res Int. 86 (2015) 1004–1013. https://doi.org/10.1002/srin.201400266.

[15] A. Memarpour, V. Brabie, P. Jönsson, Studies of effect of glass/silicon powder coatings on clogging behaviour of submerged entry nozzles when using REM alloyed stainless steels, Ironmaking & Steelmaking. 38 (2011) 229–239. https://doi.org/10.1179/1743281210Y.0000000005.

[16] E. Brandaleze, M. Ávalos, E. Benavidez, Thermal analysis techniques applied to study corrosion mechanisms of SEN used in the steel continuous casting process, J Therm Anal Calorim. 147 (2022) 219–228. https://doi.org/10.1007/s10973-020-10275-z.

[17] [REDACTED], SES burner preheating survey Tata Port Talbot: Power Point Presentation [REDACTED].

[18] [REDACTED], Tata Port Talbot, 8D Tip failures 8D Vertical Crack in the Sleeve: Power Point Presentation [REDACTED].

[19] [REDACTED], BZ20445 incident rate review: Power Point Presentation [REDACTED], [REDACTED].

[20] Y. Li, B.G. Thomas, Transient model of preheating a submerged entry nozzle, in: AISTech - Iron and Steel Technology Conference Proceedings, 2014: pp. 2907–2922. http://ccc.illinois.edu/PDF Files/Reports14/SEN Models/LI-Y Transient Model of Preheating a SEN, AISTech2014.pdf (accessed April 8, 2023).

[21] G. Wei, B. Zhu, X. Li, Z. Ma, Microstructure and mechanical properties of low-carbon MgO–C refractories bonded by an Fe nanosheet-modified phenol resin, Ceram Int. 41 (2015) 1553–1566. https://doi.org/10.1016/j.ceramint.2014.09.091.

[22] J. Podwórny, J. Wojsa, T. Wala, The Influence of Thermal Shocks on the Microstructure and Elastic Properties of Refractories, in: 2008. https://www.researchgate.net/publication/274380914 (accessed April 4, 2023).

[23] H. Wang, R.N. Singh, Thermal shock behaviour of ceramics and ceramic composites, International Materials Reviews. 39 (1994) 228–244. https://doi.org/10.1179/imr.1994.39.6.228.

[24] E. Sallah, W. Al-Shatty, C. Pleydell-Pearce, A.J. London, Distinguishing of carbons and oxidation behaviour (Part 1): Exploring model-free kinetics and RAMAN spectroscopy as a synergistic approach for evaluating carbon-bonded-refractories, Carbon Trends. 8 (2022) 100174. https://doi.org/10.1016/J.CARTRE.2022.100174.

[25] T. Dieing, W. Ibach, Software requirements and data analysis in confocal raman microscopy, in: Springer Series in Surface Sciences, Springer Verlag, 2018: pp. 89–120. https://doi.org/10.1007/978-3-319-75380-5_5.

[26] S. Vyazovkin, Model-free kinetics. Staying free of multiplying entities without necessity, J Therm Anal Calorim. 83 (2006) 45–51. https://doi.org/10.1007/s10973-005-7044-6.

[27] S. Vyazovkin, Determining preexponential factor in model-free kinetic methods: How and why?, Molecules. 26 (2021) 3077. https://doi.org/10.3390/molecules26113077.

[28] S. Vyazovkin, C.A. Wight, Isothermal and non-isothermal kinetics of thermally stimulated reactions of solids, Int Rev Phys Chem. 17 (1998) 407–433. https://doi.org/10.1080/014423598230108.

[29] H. Schulz, From the Kissinger equation to model-free kinetics: reaction kinetics of thermally initiated solid-state reactions, ChemTexts. 4 (2018) 1–10. https://doi.org/10.1007/s40828-018-0062-3.

[30] S. Vyazovkin, A.K. Burnham, J.M. Criado, L.A. Pérez-Maqueda, C. Popescu, N. Sbirrazzuoli, ICTAC Kinetics Committee recommendations for performing kinetic computations on thermal analysis data, Thermochim Acta. 520 (2011) 1–19. https://doi.org/10.1016/j.tca.2011.03.034.

[31] A.K. Coker, Industrial and Laboratory Reactors – Chemical Reaction Hazards and Process Integration of Reactors, in: Ludwig's Applied Process Design for Chemical and Petrochemical Plants, Elsevier, 2015: pp. 1095–1208. https://doi.org/10.1016/b978-0-08-094242-1.00021-8.

[32] A.A.A. Youssef, A.H. Salas, N. Al-Harbi, N.M. Basfer, D.I. Nassr, Determination of chemical kinetic parameters in Arrhenius equation of constant heating rate: Theoretical method, Alexandria Engineering Journal. 67 (2023) 461–472. https://doi.org/10.1016/j.aej.2022.12.046.

[33] S. Welch, S.C. Paul, J.L. Torero, Modelling fire growth and toxic gas formation, in: Fire Toxicity, Elsevier, 2010: pp. 637–667. https://doi.org/10.1533/9781845698072.6.637.

[34] L.D. Smoot, M.D. Horton, G.A. Williams, PROPAGATION OF LAMINAR PULVERIZED COAL-AIR FLAMES., in: Energy and Combustion Science, Elsevier, 1976: pp. 375–387. https://doi.org/10.1016/b978-0-08-024780-9.50015-0.

[35] A. Gómez-Barea, Modelling of fluidized bed gasification processes, in: Fluidized Bed Technologies for Near-Zero Emission Combustion and Gasification, Elsevier, 2013: pp. 579–619. https://doi.org/10.1533/9780857098801.2.579.

[36] A. Dhaundiyal, M.M. Hanon, Calculation of Kinetic Parameters of the Thermal Decomposition of Residual Waste of Coniferous Species: Cedrus Deodara, Acta Technologica Agriculturae. 21 (2018) 75–80. https://doi.org/10.2478/ata-2018-0014.

[37] S. Habibu, N.M. Sarih, N.A. Sairi, M. Zulkifli, Rheological and thermal degradation properties of hyperbranched polyisoprene prepared by anionic polymerization, R Soc Open Sci. 6 (2019). https://doi.org/10.1098/rsos.190869.

[38] A. Mianowski, T. Radko, T. Siudyga, Kinetic compensation effect of isoconversional methods, Reaction Kinetics, Mechanisms and Catalysis. 132 (2021) 37–58. https://doi.org/10.1007/s11144-020-01898-2.

[39] W.M. Guo, H.N. Xiao, G.J. Zhang, Kinetics and mechanisms of non-isothermal oxidation of graphite in air, Corros Sci. 50 (2008) 2007–2011. https://doi.org/10.1016/j.corsci.2008.04.017.

[40] P.J. Hacker, G.B. Neighbour, B. McEnaney, The coefficient of thermal expansion of nuclear graphite with increasing thermal oxidation, J Phys D Appl Phys. 33 (2000) 991. https://doi.org/10.1088/0022-3727/33/8/316.

[41] L. Babout, B.J. Marsden, P.M. Mummery, T.J. Marrow, Three-dimensional characterization and thermal property modelling of thermally oxidized nuclear graphite, Acta Mater. 56 (2008) 4242–4254. https://doi.org/10.1016/j.actamat.2008.04.045.

[42] A. Bernard, S. Hamdy, L. Le Corre, E. Dirlewanger, F. Lheureux, 3D characterization of walnut morphological traits using X-ray computed tomography, Plant Methods. 16 (2020) 1–11. https://doi.org/10.1186/s13007-020-00657-7.

[43] S. Kaciulis, Spectroscopy of carbon: From diamond to nitride films, Surface and Interface Analysis. 44 (2012) 1155–1161. https://doi.org/10.1002/sia.4892.

[44] M. Varga, T. Izak, V. Vretenar, H. Kozak, J. Holovsky, A. Artemenko, M. Hulman, V. Skakalova, D.S. Lee, A. Kromka, Diamond/carbon nanotube composites: Raman, FTIR and XPS spectroscopic studies, Carbon N Y. 111 (2017) 54–61. https://doi.org/10.1016/j.carbon.2016.09.064.

[45] J.R. Dennison, M. Holtz, G. Swain, Raman spectroscopy of carbon materials, Spectroscopy. 11 (1996) 38–46. https://api.semanticscholar.org/CorpusID:54670456.

[46] J. Werner, C.G. Aneziris, S. Dudczig, Young's Modulus of Elasticity of Carbon-Bonded Alumina Materials up to 1450°C, Journal of the American Ceramic Society. 96 (2013) 2958–2965. https://doi.org/10.1111/jace.12526.

[47] B. Luchini, J. Grabenhorst, J. Fruhstorfer, V.C. Pandolfelli, C.G. Aneziris, On the nonlinear behavior of Young's modulus of carbon-bonded alumina at high temperatures, Journal of the American Ceramic Society. 101 (2018) 4171–4183. https://doi.org/10.1111/jace.15575.

[48] J. Werner, C.G. Aneziris, The influence of pyrolysis temperature on Young′s modulus of carbon-bonded alumina at temperatures up to 1450 °C, Ceram Int. 42 (2016) 3460–3464. https://doi.org/10.1016/j.ceramint.2015.10.143.

[49] M. Aguilar-Pujol, R. Ramírez-Jiménez, E. Xifre-Perez, S. Cortijo-Campos, J. Bartolomé, L.F. Marsal, A. de Andrés, Supported Ultra-Thin Alumina Membranes with Graphene as Efficient Interference Enhanced Raman Scattering Platforms for Sensing, Nanomaterials. 10 (2020) 830. https://doi.org/10.3390/nano10050830.

[50] J.C. Lascovich, R. Giorgi, S. Scaglione, Evaluation of the sp2/sp3 ratio in amorphous carbon structure by XPS and XAES, Appl Surf Sci. 47 (1991) 17–21. https://doi.org/10.1016/0169-4332(91)90098-5.

[51] O.A. Maslova, M.R. Ammar, G. Guimbretière, J.N. Rouzaud, P. Simon, Determination of crystallite size in polished graphitized carbon by Raman spectroscopy, Phys Rev B Condens Matter Mater Phys. 86 (2012). https://doi.org/10.1103/PhysRevB.86.134205.

[52] P. van Beurden, Subject : Thermomechanical evaluation of the [REDACTED], DSP SEN Introduction Thermomechanical model Conclusions & recommendations, 2019.

[53] Y. KATO, Refractories for Continuous Casting, Nippon Steel Technical Report. 125 (2020). https://www.nipponsteel.com/en/tech/report/pdf/125-11.pdf (accessed February 16, 2023).

[54] R.I.L. Guthrie, M.M. Isac, Continuous Casting Practices for Steel: Past, Present and Future, Metals (Basel). 12 (2022) 862. https://doi.org/10.3390/met12050862.

[55] K. Chattopadhyay, M. Isac, R.I.L. Guthrie, Physical and Mathematical Modelling of Steelmaking Tundish Operations: A Review of the Last Decade (1999–2009), ISIJ International. 50 (2010) 331–348. https://doi.org/10.2355/isijinternational.50.331.

[56] B. Harris, A.S. Normanton, G. Abbel, B. Barber, I. Baillie, R. Koldewijn, A. Chown, S. Riaz, S. Higson, B. Patrick, T. Peeters, A.W.A. Smith, H. Visser, J. Kromhout, 5th European Continuous Casting Conference, Ironmaking & Steelmaking. 33 (2006) 82–91. https://doi.org/10.1179/174328106X101510.

[57] L. Zhang, J. Zhi, F. Mei, L. Zhu, X. Jiang, J. Shen, J. Cui, K. Cai, B.G. Thomas, Basic oxygen furnace based steelmaking processes and cleanliness control at Baosteel, Ironmaking & Steelmaking. 33 (2006) 129–139. https://doi.org/10.1179/174328106X80127.

[58] K. Chattopadhyay, M. Isac, R.I.L. Guthrie, Effect of submergence depth of the ladle shroud on liquid steel quality output from a delta shaped four strand tundish, Ironmaking & Steelmaking. 38 (2011) 398–400. https://doi.org/10.1179/1743281211Y.0000000009.

[59] P. Mutsaarts, Submerged entry nozzle exchange system for tundishes, MILLENNIUM STEEL. (2006) 144–146. http://www.millennium-steel.com/wp-content/uploads/articles/pdf/2006/pp143-146 MS06.pdf (accessed May 31, 2018).

[60] E. Zinngrebe, M. Van Wijngaarden, F. Mensonides, R. Kalter, S.R. Van Der Laan, M. Rijnders, E. Moosavi-Khoonsari, T. Steel Europe, Microstructures of Mould Slag Crawling at the SEN during Thin Slab Casting, in: European Steel Technology and ApplicationDays (ESTAD) 2019, 2019.

[61] A. Kamaraj, R. Saravanakumar, M. Rajaguru, State of the Art Control Measures for Aluminium Fade and SEN Clogging during Steelmaking Operations, IOP Conf Ser Mater Sci Eng. 314 (2018) 012022. https://doi.org/10.1088/1757-899X/314/1/012022.

[62] L. Pilato, Phenolic resins: A century of progress, Phenolic Resins: A Century of Progress. (2010) 503–515. https://doi.org/10.1007/978-3-642-04714-5.

[63] B. Rand, B. McEnaney, Carbon binders from polymeric resins and pitch. I: Pyrolysis behaviour and structure of the carbons, British Ceramic Transactions. 84 (1985) 157–165.

[64] H. Zielke, T. Wetzig, C. Himcinschi, M. Abendroth, M. Kuna, C.G. Aneziris, Influence of carbon content and coking temperature on the biaxial flexural strength of carbon-bonded alumina at elevated temperatures, Carbon N Y. 159 (2020) 324–332. https://doi.org/10.1016/j.carbon.2019.12.042.

[65] P. Gao, R. Hensley, A. Zielke, A road map to the future for the auto industry, McKinsey Quarterly. (2014) 43–53. https://www.mckinsey.com/industries/automotive-and-assembly/our-insights/a-road-map-to-the-future-for-the-auto-industry# (accessed May 4, 2021).

[66] B. McEnaney, B. Rand, CARBON BINDERS FROM POLYMERIC RESINS AND PITCH. PART II - STRUCTURE AND PROPERTIES OF THE CARBONS., British Ceramic Transactions. 84 (1985) 193–198.

[67] B. Rand, A. A. S., R. d V. P. S., THE ROLE OF CARBON IN REFRACTORIES, in: Tehran International Conference on Refractories, 2004.

[68] W.E. Lee, S. Zhang, Direct and indirect slag corrosion of oxide and oxide-c refractories, 7th Int. Conference on Molten Slags Fluxes and Salts. (2004) 309–320. http://www.saimm.co.za/Conferences/MoltenSlags2004/309-Lee.pdf (accessed June 19, 2018).

[69] W.E. LEE, Refractories, in: Comprehensive Composite Materials, Elsevier, 2000: pp. 363–385. https://doi.org/10.1016/B0-08-042993-9/00099-1.

[70] R. Warren, Ceramic-matrix composites, Composites. 18 (1987) 86–87. https://doi.org/10.1016/0010-4361(87)90485-X.

[71] G.Z. Ruan, N. Li, Carbon pickup of interstitial free steel from Al 2 O 3 –C refractories, Ironmaking & Steelmaking. 31 (2004) 342–344. https://doi.org/10.1179/030192304225018091.

[72] J.K.S. Svensson, F. Larsson, A. Memarpour, S. Ekerot, V. Brabie, P.G. Jönsson, Implementation of an YSZ coating material to prevent clogging of the submerged entry nozzle (SEN) during continuous casting of Ce-treated steels, Ironmaking & Steelmaking. 45 (2018) 105–113. https://doi.org/10.1080/03019233.2016.1245916.

[73] J.K.S. Svensson, A. Memarpour, S. Ekerot, V. Brabie, P.G. Jönsson, Studies of new coating materials to prevent clogging of submerged entry nozzle (SEN) during

continuous casting of Al killed low carbon steels, Ironmaking & Steelmaking. 44 (2017) 117–127. https://doi.org/10.1179/1743281215Y.0000000065.

[74] B. Harris, A.S. Normanton, G. Abbel, B. Barber, I. Baillie, R. Koldewijn, A. Chown, S. Riaz, S. Higson, B. Patrick, T. Peeters, A.W.A. Smith, H. Visser, J. Kromhout, 5th European Continuous Casting Conference, Ironmaking & Steelmaking. 33 (2006) 82–91. https://doi.org/10.1179/174328106X101510.

[75] R.C. Garvie, D. Hoggard, G.W. Shaffer, Advanced Ceramics for Refractories, Materials and Processing Report. 4 (1990) 6–7. https://doi.org/10.1080/08871949.1990.11752332.

[76] A.F. Dick, X. Yu, R.J. Pomfret, K.S. Coley, Attack of submerged entry nozzles by mould flux and dissolution of refractory oxides in the flux, ISIJ International. 37 (1997) 102–108. https://doi.org/10.2355/isijinternational.37.102.

[77] E. RYSHKEWITCH, Compression Strength of Porous Sintered Alumina and Zirconia., Journal of the American Ceramic Society. 36 (1953) 65–68. https://doi.org/10.1111/j.1151-2916.1953.tb12837.x.

[78] K. Mukai, J.M. Toguri, N.M. Stubina, J. Yoshitomi, A mechanism for the local corrosion of immersion nozzles., Isij International. 29 (1989) 469–476. https://doi.org/10.2355/ISIJINTERNATIONAL.29.469.

[79] J. Hong, J.-S. Park, S. Kim, A Mechanism of Slagline Wear of Graphite-Bonded Zirconia Submerged Nozzle during Continuous Casting of Steel, in: Proceedings of the 5th International Conference on Molten Slags, Fluxes, and Salts, 1997: pp. 275–280. https://api.semanticscholar.org/CorpusID:203632262 (accessed February 22, 2023).

[80] K. Sugita, Historical Overview of Refractory Technology in the Steel Industry, Nippon Steel Technical Report. 98 (2008) 8–17. http://www.nssmc.com/en/tech/report/nsc/pdf/n9803.pdf (accessed January 5, 2018).

[81] A. Yamaguchi, S. Zhang, J. Yu, Effect of refractory oxides on the oxidation of graphite and amorphous carbon, Journal of the American Ceramic Society. 79 (1996) 2509–2511. https://doi.org/10.1111/j.1151-2916.1996.tb09009.x.

[82] F.J. Long, K.W. Sykes, The effect of specific catalysts on the reactions of the steam-carbon system, Proc R Soc Lond A Math Phys Sci. 215 (1952) 100–110. https://doi.org/10.1098/rspa.1952.0199.

[83] E. Zinngrebe, V. Beurden, V. Der Laan, Investigation into excessive wear of Rotary Ladle Gates at Port Talbot. TATA Internal Report, Reference Source No: 172227, 2017.

[84] J. Ikäheimonen, K. Leiviskä, J. Ruuska, J. Matkala, NOZZLE CLOGGING PREDICTION IN CONTINUOUS CASTING OF STEEL, IFAC Proceedings Volumes. 35 (2002) 143–147. https://doi.org/10.3182/20020721-6-ES-1901.01175.

[85] N.U. Girase, S. Basu, S.K. Choudhary, Development of indices for quantification of nozzle clogging during continuous slab casting, Ironmaking & Steelmaking. 34 (2007) 506–512. https://doi.org/10.1179/174328107X168075.

[86] F. Gyakwaa, M. Aula, T. Alatarvas, T. Vuolio, Q. Shu, M. Huttula, T. Fabritius, Application of Raman Spectroscopy for Characterizing Synthetic Non-Metallic Inclusions Consisting of Calcium Sulphide and Oxides, Applied Sciences. 10 (2020) 2113. https://doi.org/10.3390/app10062113.

[87] M.A. Pimenta, G. Dresselhaus, M.S. Dresselhaus, L.G. Cançado, A. Jorio, R. Saito, Studying disorder in graphite-based systems by Raman spectroscopy, Phys. Chem. Chem. Phys. 9 (2007) 1276–1290. https://doi.org/10.1039/B613962K.

[88] F. Gyakwaa, M. Aula, T. Alatarvas, T. Vuolio, Q. Shu, M. Huttula, T. Fabritius, Application of Raman spectroscopy for characterizing synthetic non-metallic inclusions consisting of calcium sulphide and oxides, Applied Sciences (Switzerland). 10 (2020) 2113. https://doi.org/10.3390/app10062113.

[89] S. Mosca, C. Conti, N. Stone, P. Matousek, Spatially offset Raman spectroscopy, Nature Reviews Methods Primers. 1 (2021) 21. https://doi.org/10.1038/s43586-021-00019-0.

[90] R. Krishna, A.N. Jones, R. Edge, B.J. Marsden, Residual stress measurements in polycrystalline graphite with micro-Raman spectroscopy, Radiation Physics and Chemistry. 111 (2015) 14–23. https://doi.org/10.1016/j.radphyschem.2015.02.007.

[91] B. Estandia, L. Rodriguez, J.A. Alvarez, D. Ferreño, D. Hernández, J. Gonzalez, Raman spectroscopy of flake graphite as a tool to detect stress-strain states in cast iron, 71st World Foundry Congress: Advanced Sustainable Foundry, WFC 2014. (2014).

[92] F. Rosenburg, E. Ionescu, N. Nicoloso, R. Riedel, High-Temperature Raman Spectroscopy of Nano-Crystalline Carbon in Silicon Oxycarbide, Materials 2018, Vol. 11, Page 93. 11 (2018) 93. https://doi.org/10.3390/MA11010093.

[93] P. Mallet-Ladeira, P. Puech, C. Toulouse, M. Cazayous, N. Ratel-Ramond, P. Weisbecker, G.L. Vignoles, M. Monthioux, A Raman study to obtain crystallite size of carbon materials: A better alternative to the Tuinstra-Koenig law, Carbon N Y. 80 (2014) 629–639. https://doi.org/10.1016/j.carbon.2014.09.006.

[94] A. Eckmann, A. Felten, A. Mishchenko, L. Britnell, R. Krupke, K.S. Novoselov, C. Casiraghi, Probing the nature of defects in graphene by Raman spectroscopy, Nano Lett. 12 (2012) 3925–3930. https://doi.org/10.1021/NL300901A/SUPPL_FILE/NL300901A_SI_001.PDF.

[95] F. Wang, Z. Huang, Y. Liu, Y. Li, Novel cardanol-containing boron-modified phenolic resin composites, High Perform Polym. 29 (2017) 279–288. https://doi.org/10.1177/0954008316641196.

[96] A. Khawam, D.R. Flanagan, Role of isoconversional methods in varying activation energies of solid-state kinetics: I. isothermal kinetic studies, Thermochim Acta. 429 (2005) 93–102. https://doi.org/10.1016/j.tca.2004.11.030.

[97] Y. Li, J. Wang, H. Duan, L. Han, Q. Jia, X. Liu, S. Zhang, H. Zhang, Catalytic preparation of carbon nanotube/SiC whisker bonded low carbon MgO–C refractories and their high-temperature mechanical properties, Ceram Int. 48 (2022) 5546–5556. https://doi.org/10.1016/J.CERAMINT.2021.11.099.

[98] J. Wang, X. Deng, H. Zhang, Y. Zhang, H. Duan, L. Lu, J. Song, L. Tian, S. Song, S. Zhang, Synthesis of carbon nanotubes via Fe-catalyzed pyrolysis of phenolic resin, Physica E Low Dimens Syst Nanostruct. 86 (2017) 24–35. https://doi.org/10.1016/J.PHYSE.2016.09.016.

[99] S. Li, J. Liu, J. Wang, L. Han, H. Zhang, S. Zhang, Catalytic preparation of graphitic carbon spheres for Al2O3-SiC-C castables, Ceram Int. 44 (2018) 12940–12947. https://doi.org/10.1016/J.CERAMINT.2018.04.108.

[100] D. Halder, P.R. Midya, S. Das, N.S. Das, I. Roy, K.K. Chattopadhyay, Amorphous carbon nanotubes incorporated MgO-graphite composite with enhanced properties for steel making furnaces, Ceram Int. 42 (2016) 15826–15835. https://doi.org/10.1016/J.CERAMINT.2016.07.051.

[101] H. Zielke, T. Wetzig, C. Himcinschi, M. Abendroth, M. Kuna, C.G. Aneziris, Influence of carbon content and coking temperature on the biaxial flexural strength of carbon-bonded alumina at elevated temperatures, Carbon N Y. 159 (2020) 324–332. https://doi.org/10.1016/j.carbon.2019.12.042.

[102] T.H. Ko, W.S. Kuo, Y.H. Chang, Microstructural changes of phenolic resin during pyrolysis, J Appl Polym Sci. 81 (2001) 1084–1089. https://doi.org/10.1002/app.1530.

[103] A.P. Luz, C.G. Renda, A.A. Lucas, R. Bertholdo, C.G. Aneziris, V.C. Pandolfelli, Graphitization of phenolic resins for carbon-based refractories, Ceram Int. 43 (2017) 8171–8182. https://doi.org/10.1016/j.ceramint.2017.03.143.

[104] D. Tuschel, Stress, Strain, and Raman Spectroscopy, Spectroscopy. 34 (2019) 10–21. https://www.spectroscopyonline.com/view/stress-strain-and-raman-spectroscopy.

[105] M.-A. Faghihi-Sani, A. Yamaguchi, Oxidation kinetics of MgO–C refractory bricks, Ceram Int. 28 (2002) 835–839. https://doi.org/10.1016/S0272-8842(02)00049-4.

[106] Z. Liu, J. Yu, S. Yue, D. Jia, E. Jin, B. Ma, L. Yuan, Effect of carbon content on the oxidation resistance and kinetics of MgO-C refractory with the addition of Al powder, Ceram Int. 46 (2020) 3091–3098. https://doi.org/10.1016/j.ceramint.2019.10.010.

[107] B. Hashemi, Z.A. Nemati, M.A. Faghihi-Sani, Effects of resin and graphite content on density and oxidation behavior of MgO-C refractory bricks, Ceram Int. 32 (2006) 313–319. https://doi.org/10.1016/j.ceramint.2005.03.008.

[108] W. Guo, H. Xiao, E. Yasuda, Y. Cheng, Oxidation kinetics and mechanisms of a 2D-C/C composite, Carbon N Y. 44 (2006) 3269–3276. https://doi.org/10.1016/j.carbon.2006.06.027.

[109] K. Nishikawa, Y. Ueta, D. Hara, S. Yamada, N. Koga, Kinetic characterization of multistep thermal oxidation of carbon/carbon composite in flowing air, J Therm Anal Calorim. 128 (2017) 891–906. https://doi.org/10.1007/s10973-016-5993-6.

[110] C.A.A. Cairo, M. Florian, M.L.A. Graça, J.C. Bressiani, Kinetic study by TGA of the effect of oxidation inhibitors for carbon-carbon composite, Materials Science and Engineering A. 358 (2003) 298–303. https://doi.org/10.1016/S0921-5093(03)00302-2.

[111] L. Chen, B. Wang, D. Yi, H. Liu, Non-isothermal oxidation kinetics of WC–6Co cemented carbides in air, Int J Refract Metals Hard Mater. 40 (2013) 19–23. https://doi.org/10.1016/j.ijrmhm.2013.02.003.

[112] F. Wang, L. Zhao, W. Fang, X. He, F. Liang, H. Chen, H. Chen, X. Du, Preparation of organic/inorganic composite phenolic resin and application in Al2O3-C refractories, Int J Appl Ceram Technol. 13 (2016) 133–139. https://doi.org/10.1111/ijac.12426.

[113] J.M. Pérez, A. Fernández, Thermal stability and pyrolysis kinetics of lignin-phenol-formaldehyde resins, J Appl Polym Sci. 123 (2012) 3036–3045. https://doi.org/10.1002/app.34817.

[114] M. V. Alonso, M. Oliet, J.C. Domínguez, E. Rojo, F. Rodríguez, Thermal degradation of lignin–phenol–formaldehyde and phenol–formaldehyde resol resins, J Therm Anal Calorim. 105 (2011) 349–356. https://doi.org/10.1007/s10973-011-1405-0.

[115] G. Mishra, T. Bhaskar, Non isothermal model free kinetics for pyrolysis of rice straw, Bioresour Technol. 169 (2014) 614–621. https://doi.org/10.1016/j.biortech.2014.07.045.

[116] D. Drozin, S. Sozykin, N. Ivanova, T. Olenchikova, T. Krupnova, N. Krupina, V. Avdin, Kinetic calculation: Software tool for determining the kinetic parameters of the thermal decomposition process using the Vyazovkin Method, SoftwareX. 11 (2020) 100359. https://doi.org/10.1016/j.softx.2019.100359.

[117] N. V. Muravyev, A.N. Pivkina, N. Koga, Critical appraisal of kinetic calculation methods applied to overlapping multistep reactions, Molecules. 24 (2019). https://doi.org/10.3390/molecules24122298.

[118] S. Vyazovkin, A.K. Burnham, L. Favergeon, N. Koga, E. Moukhina, L.A. Pérez-Maqueda, N. Sbirrazzuoli, ICTAC Kinetics Committee recommendations for analysis of multi-step kinetics, Thermochim Acta. 689 (2020) 178597. https://doi.org/10.1016/j.tca.2020.178597.

[119] N. Sbirrazzuoli, L. Vincent, J. Bouillard, L. Elegant, Isothermal and non-isothermal kinetics when mechanistic information available, J Therm Anal Calorim. 56 (1999) 783–792. https://doi.org/10.1023/A:1010110307418.

[120] X. Li, B. Zhu, F. Zhao, In-situ synthesis of SiC and β-Si3Al3O3N5 whiskers in alumina carbon based materials, Materials Science Forum. 745–746 (2013) 663–666. https://doi.org/10.4028/www.scientific.net/MSF.745-746.663.

[121] G.E.A. Swann, S. V. Patwardhan, Application of Fourier Transform Infrared Spectroscopy (FTIR) for assessing biogenic silica sample purity in geochemical analyses and palaeoenvironmental research, Climate of the Past. 7 (2011) 65–74. https://doi.org/10.5194/cp-7-65-2011.

[122] F. Kundie, C. Azhari, Z. Ahmad, Effect of nano- and micro-alumina fillers on some properties of poly(methyl methacrylate) denture base composites, Journal of the Serbian Chemical Society. 83 (2018) 75–91. https://doi.org/10.2298/JSC170118056K.

[123] M. Kolahdoozan, R.J. Kalbasi, Z.S. Shahzeidi, F. Zamani, Knoevenagel Condensation of Aldehydes with Ethyl Cyanoacetate in Water Catalyzed by P4VP/Al 2 O 3 -SiO 2, J Chem. 2013 (2013) 1–8. https://doi.org/10.1155/2013/496837.

[124] A. Boumaza, A. Djelloul, F. Guerrab, Specific signatures of α-alumina powders prepared by calcination of boehmite or gibbsite, Powder Technol. 201 (2010) 177–180. https://doi.org/10.1016/j.powtec.2010.03.036.

[125] A.R. Abhijith, A.K. Srivastava, A. Srivastava, Synthesis and Characterization of Magnesium Doped ZnO Using Chemical Route, J Phys Conf Ser. 1531 (2020). https://doi.org/10.1088/1742-6596/1531/1/012005.

[126] C. Fang, Y. Zhang, Z. Zhang, C. Shan, W. Shen, X. Jia, Preparation of “natural” diamonds by HPHT annealing of synthetic diamonds, CrystEngComm. 20 (2018) 505–511. https://doi.org/10.1039/C7CE02013A.

[127] Z. Yao, S. Yu, W. Su, W. Wu, J. Tang, W. Qi, Kinetic studies on the pyrolysis of plastic waste using a combination of model-fitting and model-free methods, Waste Management and Research. 38 (2020) 77–85. https://doi.org/10.1177/0734242X19897814.

[128] A.O. Balogun, A.A. Adeleke, P.P. Ikubanni, S.O. Adegoke, A.M. Alayat, A.G. McDonald, Kinetics modeling, thermodynamics and thermal performance assessments of pyrolytic decomposition of Moringa oleifera husk and Delonix regia pod, Sci Rep. 11 (2021) 13862. https://doi.org/10.1038/s41598-021-93407-1.

[129] J. Xu, J. Yang, X. Liu, H. Wang, J. Zhang, S. Fu, Preparation and characterization of fast-curing powder epoxy adhesive at middle temperature, R Soc Open Sci. 5 (2018). https://doi.org/10.1098/rsos.180566.

[130] N. Sbirrazzuoli, Model-free isothermal and nonisothermal predictions using advanced isoconversional methods, Thermochim Acta. 697 (2021) 178855. https://doi.org/10.1016/j.tca.2020.178855.

[131] W. Lu, M.Y. Li, X.W. Li, X.X. Wu, L. Bin Sun, Z.C. Li, Experimental study on the oxidation behavior and microstructural evolution of NG-CT-10 and NG-CT-20 nuclear graphite, Nuclear Science and Techniques. 30 (2019). https://doi.org/10.1007/s41365-019-0693-0.

[132] M. Sharma, S. Rani, D.K. Pathak, R. Bhatia, R. Kumar, I. Sameera, Temperature dependent Raman modes of reduced graphene oxide: Effect of anharmonicity, crystallite size and defects, Carbon N Y. 184 (2021) 437–444. https://doi.org/10.1016/J.CARBON.2021.08.014.

[133] K. Alamelu, V. Raja, L. Shiamala, B.M. Jaffar Ali, Biphasic TiO 2 nanoparticles decorated graphene nanosheets for visible light driven photocatalytic degradation of organic dyes, Appl Surf Sci. 430 (2018) 145–154. https://doi.org/10.1016/j.apsusc.2017.05.054.

[134] R. Rahimi, S. Zargari, Z. Sadat Shojaei, Photoelectrochemical Investigation of TiO2-Graphene Nanocomposites, in: Proceedings of The 18th International

Electronic Conference on Synthetic Organic Chemistry, MDPI, Basel, Switzerland, 2014: p. a044. https://doi.org/10.3390/ecsoc-18-a044.

[135] W.W. So, S. Bin Park, K.J. Kim, C.H. Shin, S.J. Moon, The crystalline phase stability of titania particles prepared at room temperature by the sol-gel method, J Mater Sci. 36 (2001) 4299–4305. https://doi.org/10.1023/A:1017955408308.

[136] Y. Xu, S. Sang, Y. Li, B. Ren, L. Zhao, Y. Li, S. Li, Pore structure, permeability, and alkali attack resistance of Al 2O3-C Refractories, Metall Mater Trans A Phys Metall Mater Sci. 45 (2014) 2885–2893. https://doi.org/10.1007/s11661-014-2217-1.

[137] R. Bo, S. Shaobai, L. Yawei, J. Shengli, Correlation of pore structure and alkali vapor attack resistance of bauxite–SiC composite refractories, Ceram Int. 41 (2015) 14674–14683. https://doi.org/10.1016/j.ceramint.2015.07.190.

[138] D. Hu, H. Chen, Z. Yong, M. Chen, X. Zhang, Q. Li, Z. Fan, Z. Feng, Enhanced Thermal Conductivity of Carbon Nanotube Arrays by Carbonizing Impregnated Phenolic Resins, Materials Sciences and Applications. 04 (2013) 453–457. https://doi.org/10.4236/msa.2013.48055.

Appendices

μ -CT of Large pore-network crack

EqDiameter		
Preheat Time	Average >= 100 μm	Max >= 100 μm
0-Hr	139.53492	282.514
3-Hr	138.2726111	357.932
6-Hr	287.9725	433

Image Segmentation of μ-CT pores

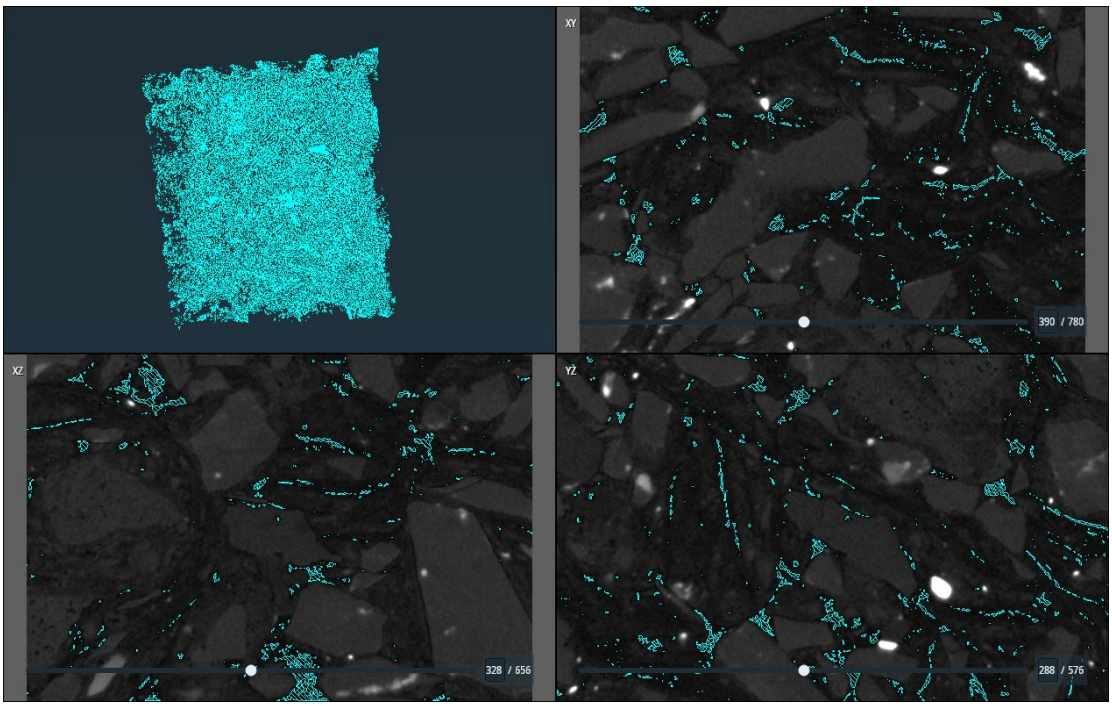

Image Segmentation of µ-CT Carbon Matrix

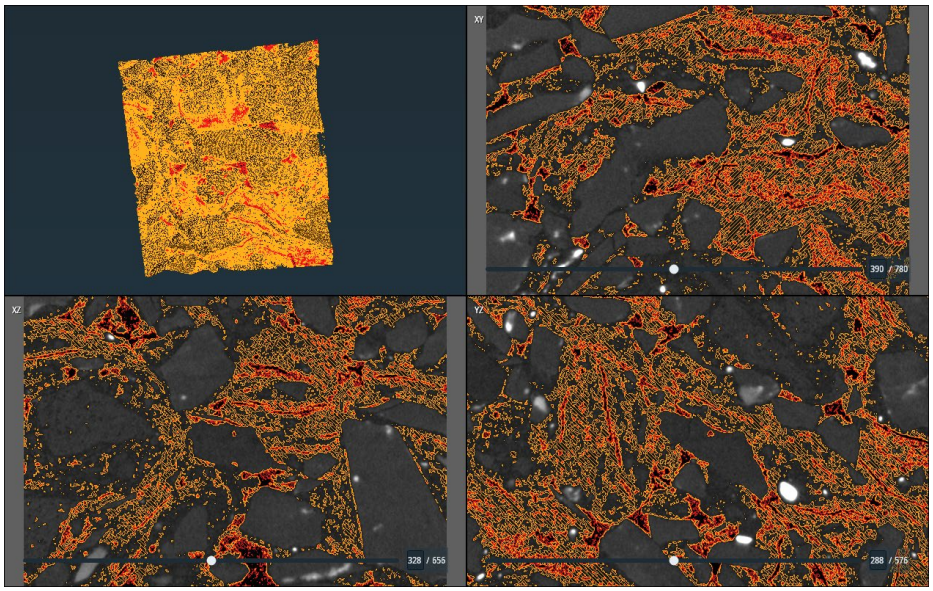

Image Segmentation of µ-CT Carbon Matrix and Aggregate

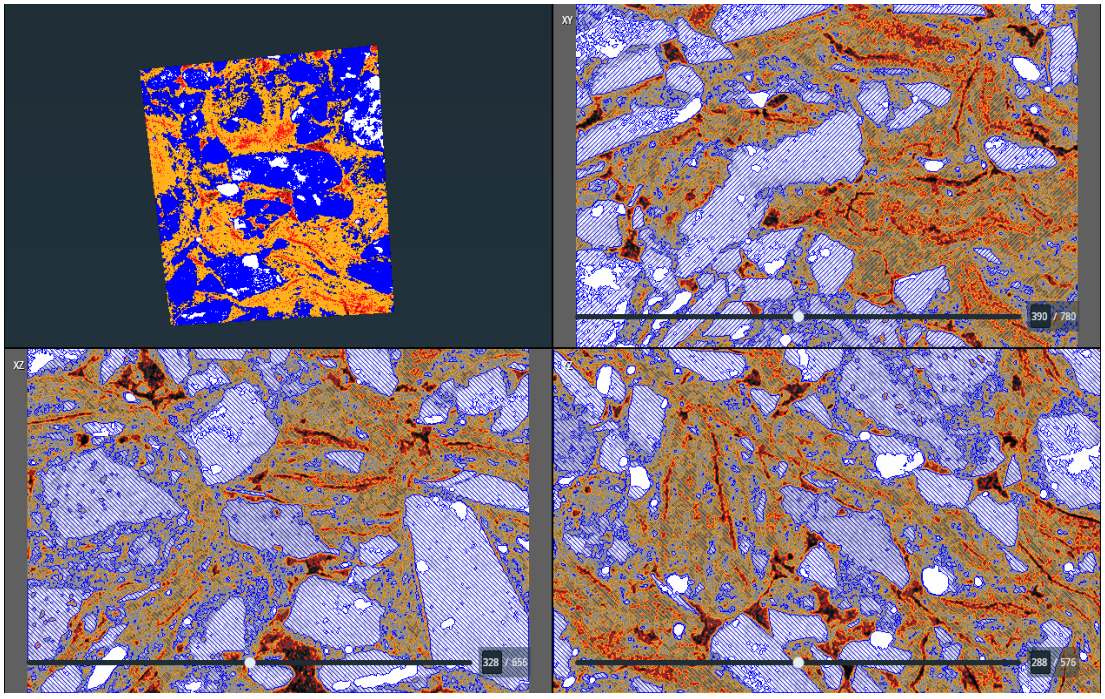

Image Segmentation of μ-CT of All regions

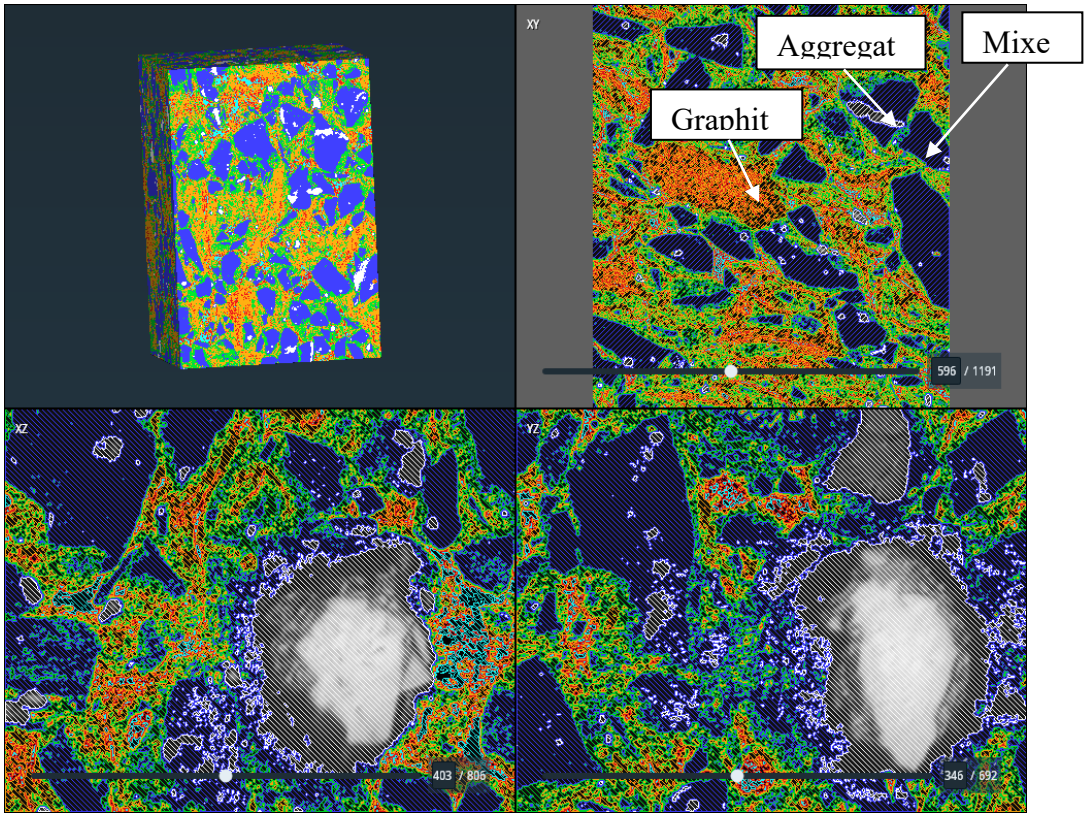

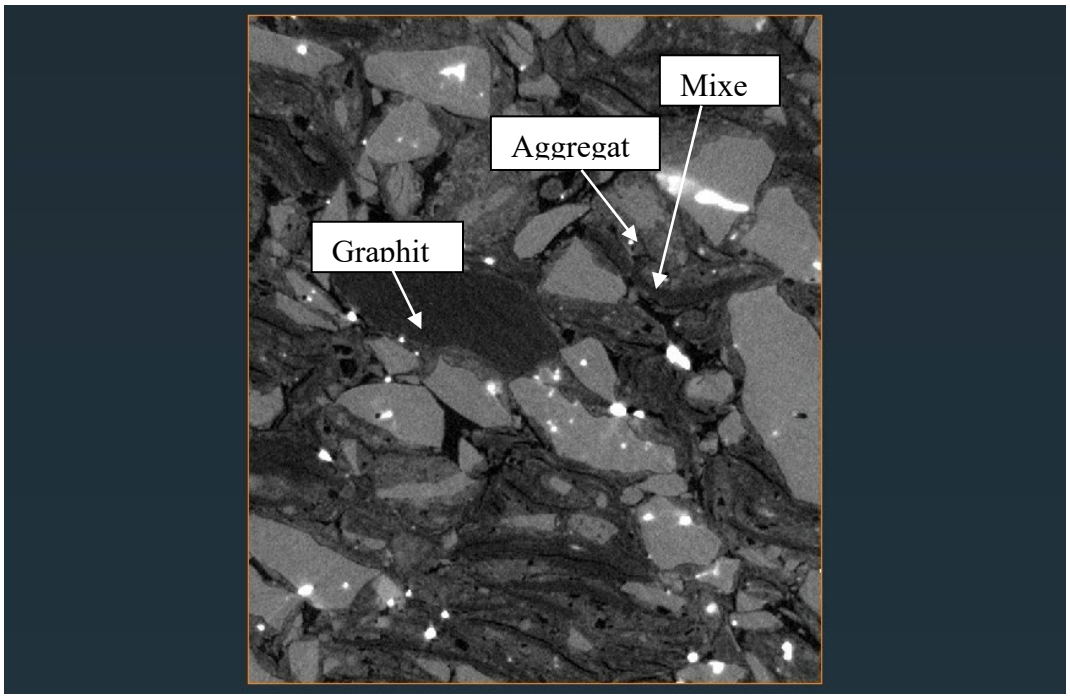

Dampening Wave, and Frequency Velocity fityk fitted peak

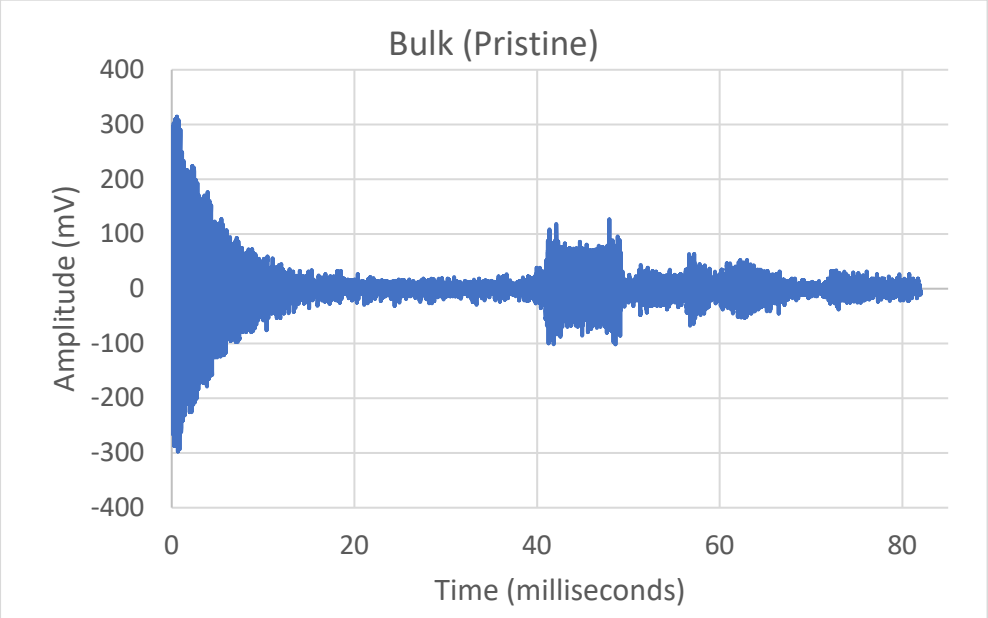

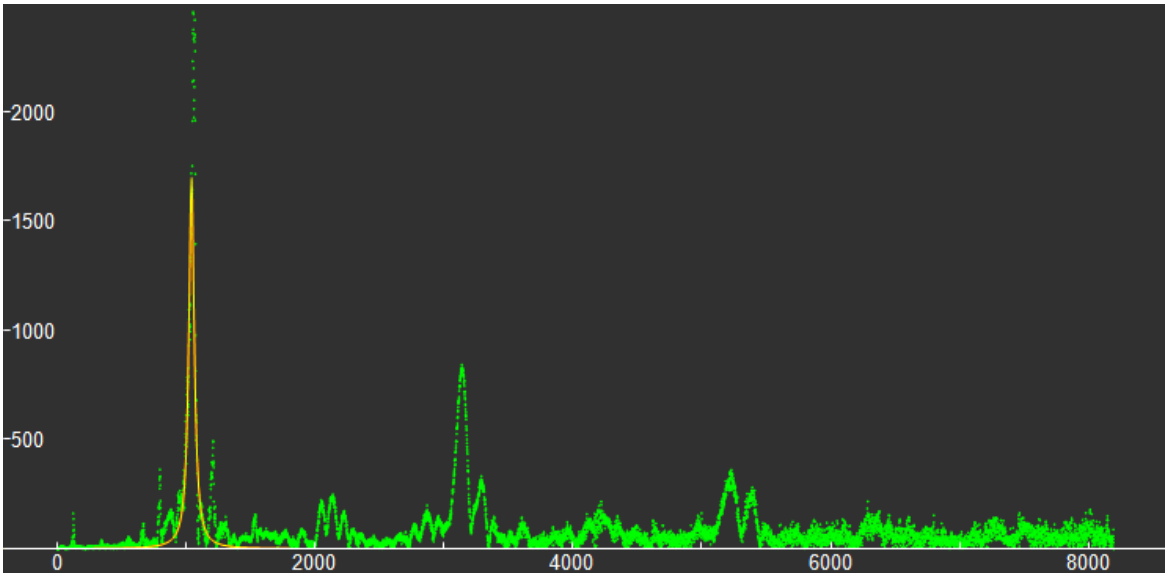

Illustration of Lorentzian peak fitting of G and D peak

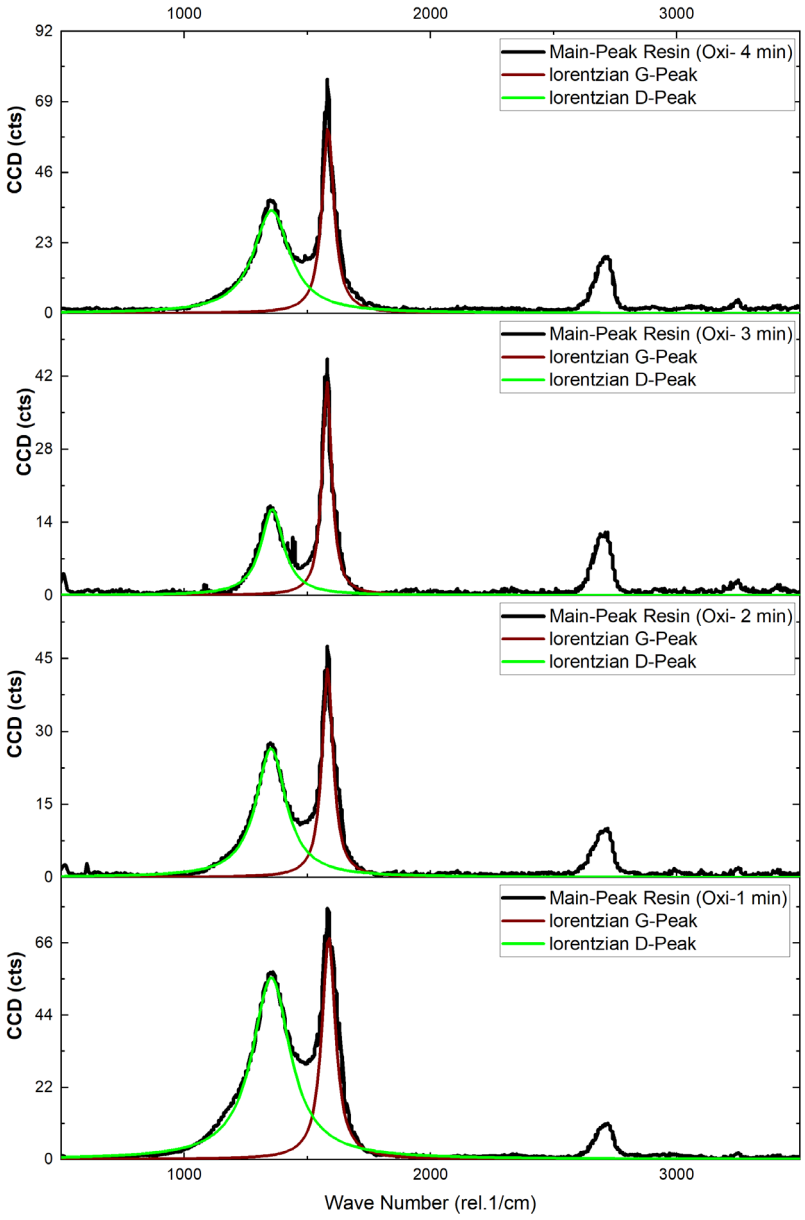

SEM and FTIR Scans for SEN samples

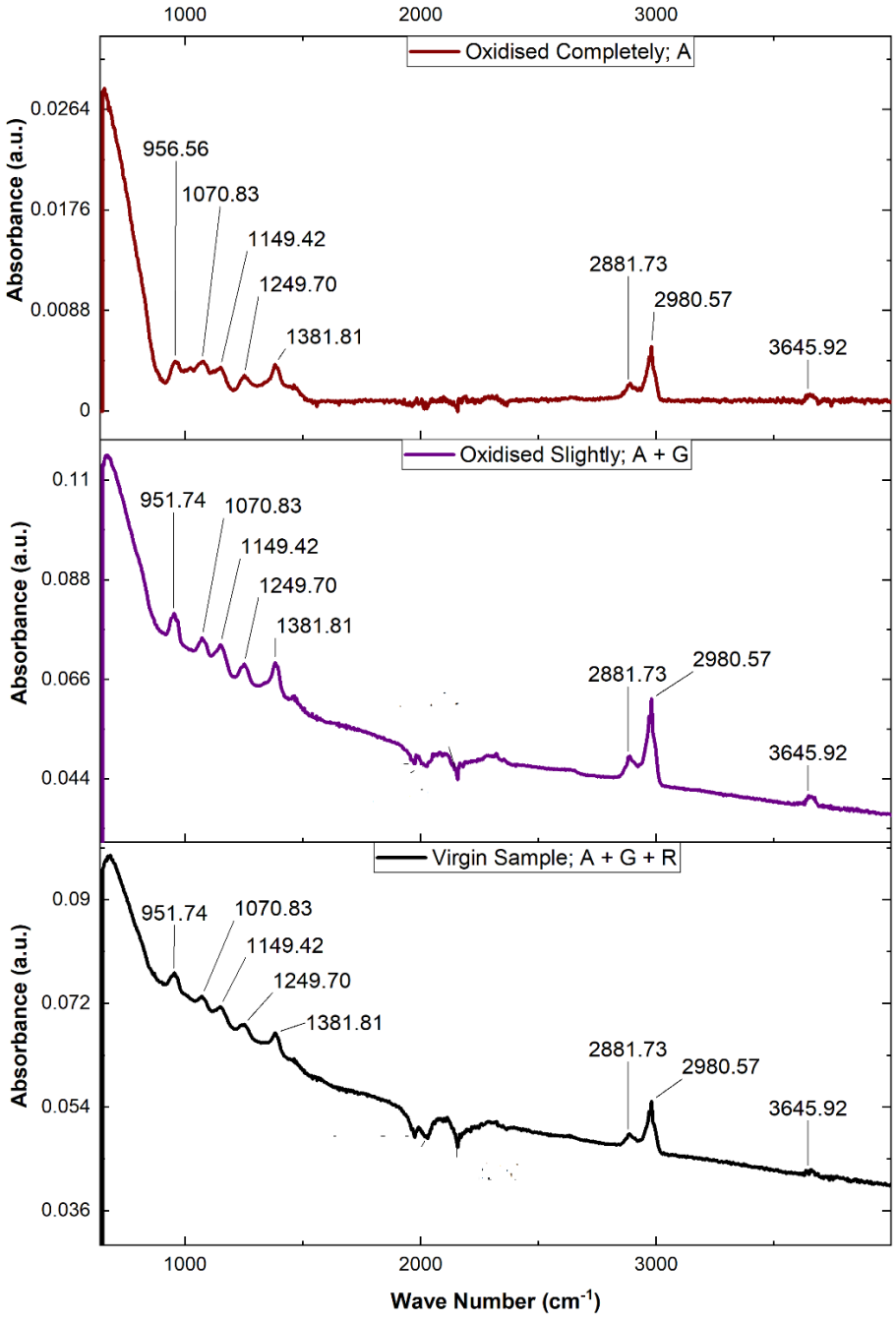

A = Aggregate G=Graphite Resin

Virgin SEN

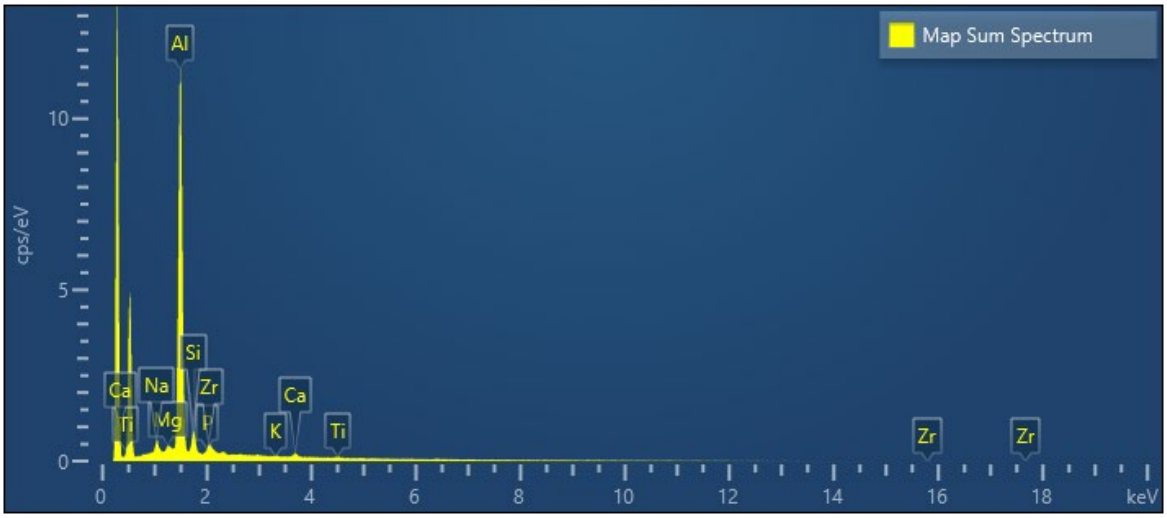

Electron Image 7

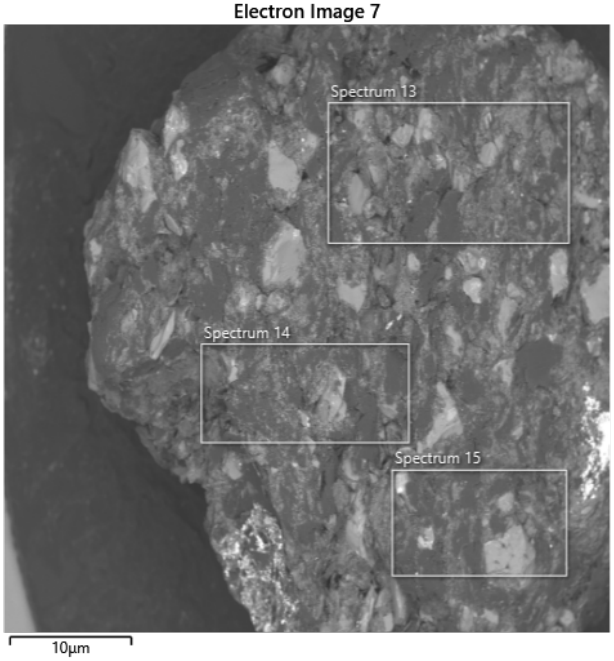

3 hour Preheated SEN

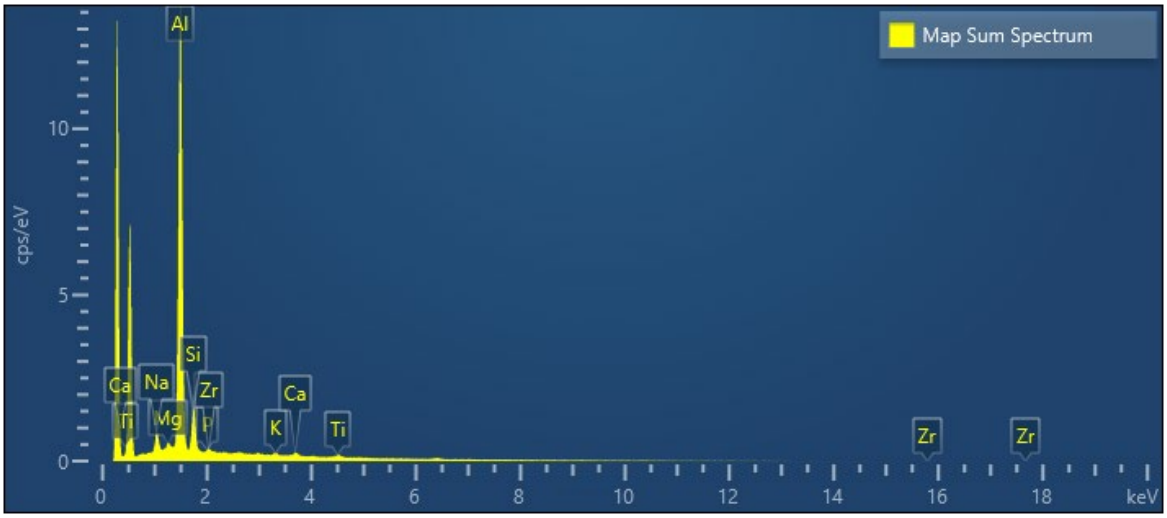

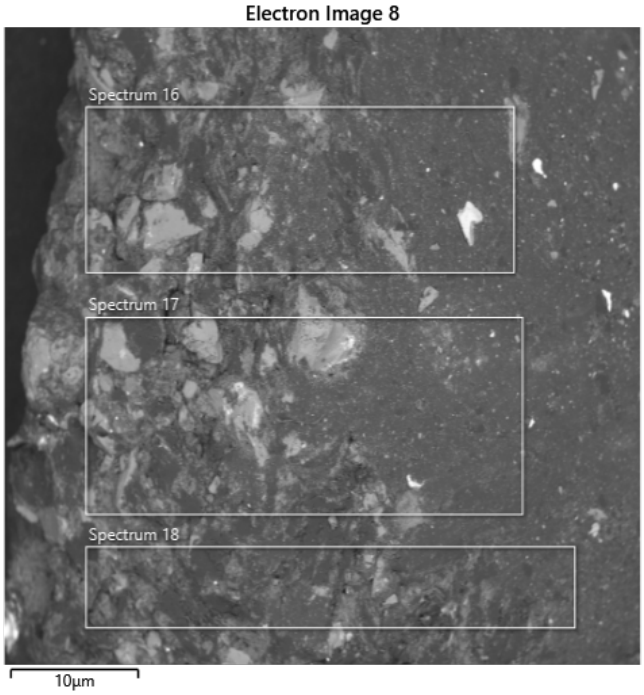

6 hour Preheated SEN